Dissertation

submitted to the

Combined Faculties for the Natural Sciences and for Mathematics
of the Ruperto-Carola University of Heidelberg, Germany

for the degree of

Doctor of Natural Sciences

presented by
Diplom-Physicist

Axel Nimmerjahn

born in
Kulmbach, Germany

Oral Examination: July 4th, 2005

Advances in Two-Photon Fluorescence Microscopy for High-Resolution Anatomical and Functional Imaging of Cell Populations in the Intact Brain

Referees

Prof. Dr. Bert Sakmann
Prof. Dr. Karlheinz Meier

Advances in Two-Photon Fluorescence Microscopy for High-Resolution Anatomical and Functional Imaging of Cell Populations in the Intact Brain

Two-photon microscopy has enabled high-resolution imaging of single cells in the brain of anaesthetized animals. Here we developed two-photon microscopy towards imaging of cell populations in the neocortex of awake behaving rodents. For this purpose, we developed two miniature two-photon microscopes based on fluorescence excitation through a hollow-core photonic crystal fiber and a coherent fiber-bundle, respectively. In addition, we demonstrate their applicability to in vivo imaging. Furthermore, as meaningful biological application critically depends on fluorescence labeling, we developed staining methods for three different cell populations. In particular, we used Sindbis- and Lentiviral gene transfer into neurons for targeted expression of fluorescent indicators. We discovered a method for specific staining of astroglia in vivo, and we employed transgenic fluorescent protein expression to label microglia. Using a standard two-photon microscope, we show that in the adult brain neurons and astroglia show overall stable morphologies. In contrast, microglia displayed continuous structural changes, and responded rapidly to local injury. Furthermore, we uncovered the distinctive calcium dynamics underlying neuronal and astroglial cell signaling in vivo. Taken together, these advances in miniaturization and fluorescence labeling promise to enable optical studies of network activity during behavior.

Fortschritte in der Zwei-Photonen Fluoreszenzmikroskopie zur hochauflösenden anatomischen und funktionellen Untersuchung von Zellpopulationen im intakten Gehirn

Die Zwei-Photonen Mikroskopie hat die hochauflösende Untersuchung einzelner Zellen im Gehirn anästhesierter Tiere ermöglicht. Die vorliegende Arbeit beschreibt die Weiterentwicklung dieser Technik in Richtung Zellpopulationsstudien im Neokortex von freilaufenden Nagetieren. Insbesondere wurden zwei Miniaturmikroskope, basierend auf der Fluoreszenzanregung durch eine photonische Kristallfaser beziehungsweise durch ein kohärentes Faserbündel, entwickelt und deren Einsatzfähigkeit anhand von in vivo Messungen verifiziert. Eine sinnvolle biologische Anwendung dieser Mikroskope setzt jedoch geeignete Fluoreszenzfärbemethoden voraus. Daher wurden zudem Methoden zur Färbung dreier Zellpopulationen entwickelt. Insbesondere wurden Sindbis- und Lentiviren zum Transfer und der gerichteten Expression genetisch kodierter Fluoreszenzindikatoren in Neuronen eingesetzt. Weiterhin wurde eine Methode zur spezifischen Färbung von Astroglia entdeckt und die transgene Expression von fluoreszierenden Proteinen zur Mikrogliazellfärbung eingesetzt. Mit einem Standard-Zwei-Photonen Mikroskop konnte gezeigt werden, daß sich Neurone und Astroglia im adulten Gehirn morphologisch kaum verändern, während Mikrogliazellen ihre Gestalt dynamisch variieren und schnell auf lokale Hirnverletzungen reagieren. Zudem konnte die spezifische Kalziumdynamik von Neuronen und Astroglia im intakten Gehirn visualisiert werden. Diese Fortschritte im Bereich Miniaturisierung und Fluoreszenzfärbung lassen die optische Messung von verhaltensabhängiger Netzwerkaktivität möglich erscheinen.

Contents

1 Motivation **3**

2 Introduction **5**

2.1 The Brain . . . 5

2.1.1 Anatomy . . . 5

2.1.2 Functional Organization . . . 9

2.1.3 The Rodent Brain as a Model System . . . 13

2.2 In Vivo Two-Photon Fluorescence Microscopy . . . 14

2.2.1 Instrumentation . . . 15

2.2.2 Fluorescence Excitation . . . 17

2.2.3 Fluorescence Detection . . . 18

2.2.4 Spatial Resolution . . . 20

2.2.5 Temporal Resolution . . . 21

2.2.6 Depth Penetration . . . 21

2.2.7 Further Considerations . . . 23

2.3 In Vivo Fluorescence Labeling . . . 24

2.3.1 Fluorescent Markers . . . 25

2.3.2 Loading Techniques . . . 28

2.4 Miniaturization of Two-Photon Fluorescence Microscopy . . . 31

3 Results **33**

3.1 Advancements in Microscope Miniaturization . . . 33

3.1.1 Single Fiber Based Two-Photon Microscope . . . 33

3.1.2 Coherent Fiber Bundle Based Two-Photon Microscope . . . 40

3.2 In Vivo Imaging Using Fiber-Based Two-Photon Microscopes . . . 45

3.3 Fluorescence Labeling of Neocortical Cell Populations In Vivo . . . 46

3.3.1 Neurons . . . 47

3.3.2 Astrocytes . . . 51

3.3.3 Microglia . . . 58

3.4 Dynamic Processes in Neocortical Cell Populations In Vivo . . . 58

3.4.1 Neurons . . . 58

3.4.1.1 Structural Dynamics . . . 58

3.4.1.2 Calcium Dynamics with Genetically Encoded Calcium Indicators . . . 61
3.4.2 Astrocytes . . . 63
3.4.2.1 Distribution and Structural Dynamics . . . 63
3.4.2.2 In Vivo Calcium Dynamics . . . 64
3.4.3 Microglia . . . 67
3.4.3.1 Structural Dynamics in the Healthy Brain . . . 68
3.4.3.2 Response to Local Injury . . . 73

4 Discussion **77**
4.1 Advancements in Microscope Miniaturization . . . 77
4.1.1 Single Fiber Based Two-Photon Microscope . . . 77
4.1.2 Coherent Fiber Bundle Based Two-Photon Microscope . . . 78
4.2 Fluorescence Labeling and Imaging of Neocortical Cell Populations In Vivo 79
4.2.1 Neurons . . . 79
4.2.2 Astrocytes . . . 81
4.2.3 Microglia . . . 83

5 Summary & Publications **85**

6 Future Perspectives **89**

7 Materials & Methods **93**
7.1 Fiber-Based Two-Photon Microscopes . . . 93
7.1.1 Single Fiber Based Two-Photon Microscope . . . 93
7.1.2 Coherent Fiber Bundle Two-Photon Microscope . . . 96
7.2 In Vivo Fluorescence Labeling and Two-Photon Imaging . . . 97
7.2.1 Neurons . . . 97
7.2.2 Astrocytes . . . 101
7.2.3 Microglia . . . 103

References **106**

Acknowledgements **123**

A Supplementary Movies **127**
A.1 Neurons . . . 127
A.2 Astrocytes . . . 128
A.3 Microglia . . . 128

B Acronyms **133**

Chapter 1

Motivation

One of the central questions in brain research is how information is encoded, processed, and stored in the intact brain on a cellular level. For example, how is incoming information from sensory cells at the periphery filtered and represented in the brain? How are memories formed or retrieved, and how are actions initiated? How is brain homeostasis controlled and how do the various brain elements communicate or cooperate with each other?

During the last years, it has become obvious that the interactions between cortical elements are much more complex than previously thought. For example, neurons are regarded as *the* elements responsible for information processing in the brain, while glial cells (mainly astrocytes, oligodendroctes and microglial cells) have been assumed to simply give structural and nutritional support to neurons. A role for glia in information processing has been neglected for a long time, most probably because glial cells lack the ability to generate action potentials and thus cannot communicate via propagating electrical activity as neurons do. However, recent studies have shown that astrocyes, for example, can sense and respond to neuronal activity. Incoming signals in astrocytes are communicated to neighboring astrocytes (and other cell types, like neurons and microglia) or over long distances. These and other findings have raised fundamental questions about the role as well as the interaction of various cellular networks in brain function, and in particular in information processing. What kind of information is processed by which network and what are the dynamic properties of those networks? How do the different networks communicate and how is their interaction altered during disease?

Researchers have tried to address these questions using various model systems and technical approaches. To date, our current understanding of how the brain functions on a cellular level primarily stems from studies on various tissue slice preparations and cell cultures. However, the variety of in vitro preparations employed (i.e. in an artificial environment outside the living organism) and tissue alterations induced by the dissection procedures contribute to a heterogeneity of observations. Modern imaging techniques now permit live imaging in the intact brain. This allows direct re-examination of basic issues and unprecedented understanding of elementary cellular principles governing brain function. In particular, two-photon fluorescence microscopy (2PM) has become an indispensable tool for high-resolution imaging in living animals. As a fluorescence microscopy technique,

however, it requires the development of appropriate fluorescence staining techniques that report specific aspects of cell or network dynamics in the intact brain. In vivo labeling of cortical networks with functional indicators, such as calcium indicators is particularly desirable, as it would enable to record cell signalling from many network components at the same time. Furthermore, approaches to miniaturize 2PM eventually may result in portable devices permitting imaging of cortical circuit dynamics during behavior. Thus, a clever symbiosis of technical advancements and novel labeling techniques promises to help resolve fundamental principles of cortical information processing.

Here, we aimed to advance 2PM from imaging of individually labeled structures in anaesthetized animals towards high-resolution functional imaging of cell populations in freely moving rodents. For this purpose, we aimed to advance both microscope miniaturization and in vivo fluorescence labeling techniques. In particular, we focused on anatomical and functional labeling and imaging of neuronal and glial cell populations.

Chapter 2

Introduction

As the aim of the thesis was to advance two-photon microscope miniaturization, and in parallel to develop, evaluate and apply novel in vivo fluorescence labeling techniques, this chapter is divided into four introductory sections which are designed to provide the physical and biological fundamentals required to comprehend the results and rationale presented in chapter 3. Section 2.1 introduces the reader to the basic anatomy and functional layout of the brain region investigated, as well as the rodent brain as a model system. Section 2.2 gives an overview of basic principles underlying 2PM, followed by a brief review on state of the art fluorescence labeling techniques used in biomedical research to visualize biological structure and function in vivo (see section 2.3). Finally, section 2.4 delineates the basic concept behind miniaturization of two-photon microscopy.

2.1 The Brain

2.1.1 Anatomy

The Brain (*Encephalon*). Commonly divided into three broader regions: (*a*) The hindbrain (*rhombencephalon*), including the medulla oblongata, pons and cerebellum, (*b*) the midbrain (*mesencephalon*), and (*c*) the forebrain (*prosencephalon*), including the diencephalon and the cerebral hemispheres. Within the forebrain, the cerebral hemispheres comprise three deep-lying structures (the basal ganglia, the hippocampus and the amygdaloid nuclei) and an outer layer, the cerebral cortex.

The Cerebral Cortex. The largest part of the cerebral cortex (subdivided into archicortex, paleocortex, and neocortex) is occupied by neocortex, which also represents the phylogenetically most recent cortex. The neocortex typically is 1 - 4 mm in thickness (depending on species) and organized into cell layers. The number of layers and their thickness vary throughout the cortex. The most typical form of the neocortex contains six layers, numbered from the outer surface of the cortex to the underlying white matter. In addition to the layered organization, neocortex is subdivided into cortical areas. These areas are distinguished by their histological and neurochemical characteristics,

their connections (afferent/efferent fiber systems) and their functional properties (see below). Each area consists of vertical columns that traverse the layers and comprise an interconnected set of neurons. Columns are typically a fraction of a millimeter in diameter [37].

Cellular Elements of the Cerebral Cortex - Neurons. Each neocortical layer is defined primarily by the presence or absence of neuronal cell bodies. Neurons have four distinctive compartments, referred to as dendrites, soma (i.e. the cell body), axons, and terminals. Although each neuron conforms to this basic plan, several types of neurons have been distinguished (Fig. 2.1). The two major groups of cortical neurons are spiny neurons and aspiny neurons [37]. Spiny neurons are subdivided into spiny stellate cells and pyramidal cells.

Pyramidal cells represent the major population (∼70 - 85%) of all cortical neurons and they are found in layers II - VI. Pyramidal cells are long-axon cells and typically have three main distinguishing characteristics [38]:

(i) The shape of the cell soma is pyramidal or ovoid. From the upper pole arises a prominent apical dendrite directed radially towards the pia mater, giving off a number of oblique branches. From the base of the cell soma a system of large basal dendrites emerges, that is directed laterally or downward. In general, the apical dendrite reaches layer I, where it forms a tuft of branches.

(ii) From the base of the cell or the origin of a basal dendrite comes the axon that is directed downwards and leaves the cortex to terminate in other cortical or subcortical regions. The axon during its descending course through the cortex, gives off several minor and major collaterals that give rise to terminal axonal arborizations which constitute one of the main components of the intracortical circuitry. These terminal axonal arborizations are distributed locally, vertically or horizontally.

(iii) All dendritic surfaces are covered by short bulbous protrusion, called spines. An exception are the proximal segments arising directly from the cell soma which are generally spine-free.

Although morphologically very similar, pyramidal cells are heterogeneous with regard to soma size and shape, dendritic branching, spine density, pattern of axonal collaterals and projections site. With few clear exceptions (i.e. some spiny stellate cells), pyramidal cells are the only so called projection neurons of the cerebral cortex.

The remaining 15 - 30% of all cortical neurons are short-axon cells, also called interneurons. Interneurons vary greatly in their somatic, dendritic and axonal morphologies, and they are morphologically heterogenous even within each subgroup [123]. Aspiny cells (with smooth or sparsely spiny dendrites) constitute the majority of interneurons. They are found in all layers, while spiny stellate cells are confined to the middle layers of the cortex (especially layer IV).

For human temporal cortex, the total number of neurons per mm^3 in layer I - VI is 8,300, 45,600, 36,000, 46,200, 23,100 and 16,800, respectively. However, large variations

Figure 2.1: Drawing showing the main types of cortical neurons (and their axons, right) [22]. Their location with respect to layers is indicated on the left.

can be found in the numerical density of neurons between different brain regions and species [37].

Neurons (of the same or different type) in the brain are connected with each other at specific junctions, called synapses. Two types of synapses have been distinguished: chemical and electrical synapses. In the adult brain, neurons mainly form chemical synapses with other neurons, and intercellular communication is mediated by presynaptic neurotransmitter release, followed by transmitter diffusion through the synaptic cleft, and subsequent binding to postsynaptic receptors. Chemical synapses, again, are commonly subdivided into two morphological categories, asymmetrical and symmetrical synapses. Asymmetric synapses are characterized by a prominent so called postsynaptic density (PSD), while symmetric synapses show only a very thin PSD [37]. In contrast, direct intercellular communication is provided by gap-junctions, also known as electrical synapses. Gap junctions are channel-forming structures in contacting plasma membranes that allow direct metabolic and electrical communication between cells through passive diffusion of molecules [176].

Cellular Elements of the Cerebral Cortex - Glial Cells. Although the majority of the cortical volume (80 - 85%) is occupied by neuronal cell bodies and (extrinsic/intrinsic) nerve fibers [207], the neocortex contains a variety of additional elements essential to brain function, such as blood vessels and glial cells (Fig. 2.2 and 2.3). In fact, 90% of all cells in the human brain are glial cells (mainly astrocytes, oligodendrocytes, and microglia; astrocytes : oligodendrocytes : microglia $\simeq 10 : 5 : 1$) [207]. In contrast to neurons, glial cells show no distinct layered distribution. Microglia density, for example, does not change significantly across layers and typically is 4,200 - 6,600 cells/mm^3. In contrast, the density of astrocytes and oligodendrocytes varies considerably with distance from the cortical surface. In particular, oligodendrocytes are found at a typical density of $\sim$10,000 cells/mm^3 in layer 1, increasing by a factor of 4 - 5 towards deeper layers, while cortical astrocytes are found at a density of 12,000 - 32,000 cells/mm^3 in layer 1 (yet densities up to 65,000 cells/mm^3 have been reported [207]), decreasing by a factor of 2 towards layer VI [207].

Throughout the brain, astrocytes show great morphological diversity, apparently adapting their shape and size to the architecture of the surrounding tissue. Astrocytes are subdivided into three types (radial cells, fibrous astrocytes, and protoplasmic astrocytes), from which protoplasmic astrocytes are primarily found in the cortex. Protoplasmic astrocytes are bushy cells with numerous short, but highly ramified processes of variable calibre [100]. Protoplasmic astrocytes, in addition, often form end feet like structures on cortical blood vessels. In contrast, oligodendrocytes (OLGs) are highly polymorph. Nevertheless, they have been grouped into four subtypes of which type I OLGs prevail in the cortex. Type I OLGs are organized around blood vessels, neurons, and fiber tracts forming one-to-many myelin sheaths, that surround specific subpopulations of axons [207]. Thus, in gray matter, the density of oligodendrocytes correlates with that of myelinated axons. Finally, resident microglial cells are highly branched cells, with fine processes and small somata frequently found in the vicinity of blood vessels [100].

Glial cells are territorially organized with each glial cell covering an area of around

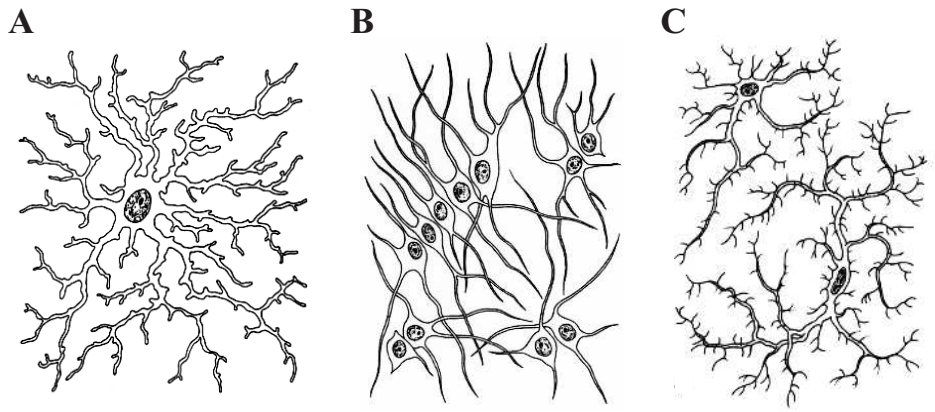

Figure 2.2: Drawing showing different glial cell types in the neocortex. (**A**) Astrocyte (**B**) Oligodendrocytes (**C**) Microglia (adapted from [62]).

30 - 60 μm diameter. Microglial cells, for example, occupy distinct territories such that cytoplasmic processes of neighboring cells do not make contact with each other. Microglial cells, in addition, do not seem to establish durable contacts with any other cell. In contrast, astrocytes show interdigitation of territories. They are heavily interconnected through intercellular gap-junctions, forming extensive multicellular networks. The territories of oligodendroglia deeply overlap. Oligodendrocytes form heterologous gap junctions with neighbouring astrocytes [129]. An intercellular coupling of oligodendrocytes, however, is still controversial [100]. Some recent reports, in addition, provide evidence for weak electrical coupling between neurons and glial cells [176].

2.1.2 Functional Organization

The Brain. Responsible for a variety of basic and higher-level bodily functions. While many of our life-sustaining functions, for example, are mediated by regions of the diencephalon and the brain stem (which comprises the medulla oblongata, pons, midbrain and parts of the hypothalamus), the cerebral cortex is responsible for planning and execution of actions in everyday life, as well as long-term memory [95].

The Cerebral Cortex. Divided into four lobes (frontal, parietal, temporal and occipital lobe), named after the overlying cranial bones. Each lobe has many distinct functional domains. The temporal lobe, for example, has distinct regions that carry out auditory or visual functions. The frontal lobe is largely concerned with the control of movement, and the parietal lobe processes somatic sensation.

Regions dedicated to a particular function include several specialized areas that, again, have different roles in processing information. These areas are known as primary, secondary, or tertiary areas, depending on their proximity to the peripheral pathways. The primary sensory areas of cortex, for example, are the initial site of cortical processing of

Figure 2.3: Schematic of the neuropil, i.e. the space between cell bodies (reconstructed from electron microscope serial sections) [186]. It contains a dense meshwork of processes, such as dendrites of pyramidal cells (green), glial processes (yellow), and axons (red and grey) emanating from the various cellular elements.

sensory information. They convey incoming information from receptor cells at the periphery to an adjacent, higher-order area, which refines the information. Each higher-order area, in turn, sends it output to one or another of three major multimodal association areas. These cortical association areas receive their specific input from cortical areas, i.e. they are not directly involved with processing sensory or motor information. Rather they are involved in integrating and interpreting information from two or more sensory modalities. In contrast, the primary motor cortex is the final site in the cortex for processing motor commands. Higher-order motor areas compute programs of movement that are conveyed to the primary motor cortex for implementation [95].

Each cortical area consists of functional units (also called columns), and information is processed across layers in an interconnected set of neurons. In particular, cortical neurons are thought to be organized into multiple, small repeating microcircuits based around pyramidal cells and their input-output connections. However, given the great diversity of anatomical, molecular and physiological types of neurons, and the intricate connectivity, it is evident that a unique, discrete microcircuit cannot exist. It is possible, however, to draw up a common basic microcircuit, with respect to the density and types of neurons per column [37].

The cortex receives inputs from the thalamus, other cortical regions on both sides of the brain, and from a variety of other sources. Different inputs to the cortex appear to be processed in different ways. The output of cortex is directed to several brain regions, including other regions of the cortex on both sides of the brain, the basal ganglia, the thalamus, the pontine nuclei, as well as the spinal cord. Outputs of the cortex arise from different areas as well as different populations of cells.

Cellular Elements of the Cerebral Cortex - Neurons. Neurons are the elements that mediate electrical activity in the brain. Generally, neurons receive signals from other neurons via their (chemical) synapses on dendrites. Incoming information is integrated near the soma and outgoing signals are conveyed via the axon to synapses at target cells of the same or different type. Although each neuron conforms to this basic principle, each type differs considerably. Differences concern the number and distribution of their dendritic trees and axon branches, the location of synaptic inputs on the cell, their location in the neocortical layers, the types of target cells to which they project, and their biochemical composition (e.g. transmitter type, enzymes, pumps, and receptors). It seems that pyramidal cells, for example, located in different layers and/or areas participate in different synaptic circuits. Different populations of pyramidal cells receive different synaptic input, and pyramidal cells occupying different layers project to different sites. In particular, the projection site of pyramidal neurons is considered the most important feature for distinguishing these morphologically rather stereotyped cells.

Pyramidal cells are excitatory cells, that use glutamate as their primary transmitter. The dendritic shafts and spines of pyramidal cells are thought to be the only postsynaptic sites for axon terminals of the major cortical afferent systems to form asymmetrical synapses [38]. In contrast, interneurons have more than one type of postsynaptic element among their synaptic targets, including dendritic shafts, spines, somata and axon initial segments. The degree of preference for these postsynaptic elements vary markedly be-

tween different types of interneurons. Interneurons are mostly inhibitory cells that use γ-aminobutyric acid (GABA) as their primary transmitter [36]. An important example of an excitatory interneuron is the spiny stellate cell, that uses glutamate as its transmitter.

While the main sources of symmetrical synapses are the inhibitory interneurons, asymmetrical excitatory synapses are formed by the corticocortical and thalamocortical axons and the local axon collaterals of pyramidal cells and spiny stellate cells. The percentage of symmetrical and asymmetrical synapses in the cortex varies between 10 - 20% and 80 - 90% respectively. A characteristic feature of the synaptic relationships among cortical neurons is that a given nonpyramidal neuron or pyramidal cell forms relatively few synapses with other neurons. The same holds true for the extrinsic cortical afferent fibers. Ten to twenty synapses with the same postsynaptic cell is considered a high number of synapses. Since a cortical neuron may receive synapses on the order of several thousands (5,000 - 60,000 synapses per neuron), this implies that the synaptic connections of individual cortical neurons are highly divergent [38].

Changes in the strength of chemical synapses between neurons, as well as in the 'wiring diagram' itself are thought to underly learning-induced changes in the cortex [28]. In contrast, gap junction channels are thought to contribute to synchronizing large neuronal ensembles (including oscillatory activity) at different frequency bands, and to be involved in epileptogenesis [176]. Finally, the diversity of neurons (especially that of interneurons) might be crucial for providing sufficient sensitivity and dynamic range to match stimulus complexity and to maintain the delicate balance between excitation and inhibition required for normal brain function [123].

Cellular Elements of the Cerebral Cortex - Glial Cells. While neurons are important elements in information processing, glial cells are commonly described as cells providing structural and nutritional support to neurons. In recent years, however, it has become obvious that glia are involved in much more the brain does [158]. In particular, recent findings suggest glia involvement in information processing [18]. More importantly, glia play pivotal roles in various disease states.

Microglial cells, for example, are immuno-competent cells in the brain and their functional role is best defined as the first responsive elements during pathologic events. Little is known, however, about their role in the normal brain. The morphology and branching patterns of microglial cells show heterogeneity between different brain regions, indicating that the shape of microglial cells adapts well to the architecture of the brain region they populate. Biochemical interactions exist both between glial cells of the same and different type, and with neurons. Intricate bi-directional signalling becomes especially apparent during immune defense against brain pathology, which requires a concerted and graded response of various cortical and extra-cortical elements.

Oligodendrocytes (OLGs) are defined as the cells that make and maintain myelin in the brain. Myelination of axons, as particularly prominent in the white matter, ensures rapid signal conduction over long distances. The vast majority of oligodendroglial cells form one-to-many myelin sheaths, which surround specific subpopulations of axons [207].

The role of astrocytes is less well defined. For example, astrocytes are thought to provide guiding structures during development and represent important elements for

controlling the composition of the extracellular space mediating signals between the brain endothelium and the neuronal membrane. Through their gap-junctional coupling they constitute a three-dimensional net whose mesh size is adapted to the various functions subserved by neurons of different regions and their companion glial cells [100]. Astrocytes, in addition, are critically involved in a variety of brain diseases, such as Alexander disease and glioma formation.

2.1.3 The Rodent Brain as a Model System

Medical research aims at understanding biological functions of the human organism and the factors that influence its normal operation. Such insights provide the basis for comprehension of pathologic alterations and the development of new strategies to maintain (e.g. through vaccines), restore (e.g. through drugs), or even improve human's health. New technological or pharmaceutical developments (e.g. of new diagnostic tools), however, require understanding of basic phenomena at the molecular, single cell, network, and higher order level. Yet many of the basic mechanisms underlying bodily functions have remained elusive. It is not known, for example, how sensory or motor information is handled by the different cellular networks in certain areas of our brain or how these networks communicate following brain injury in order to confine tissue damage.

For ethical reasons those and other basic questions must not be addressed in humans. Therefore, one requires an appropriate model system. Such a system needs to be highly reproducible, easy to handle and to manipulate. Importantly, results obtained in the model should be portable to the real system. In this respect, rodents (in particular mice and rats) present a valuable model system since they share many basic biological functions (e.g. learning and memory or immune response). In addition, their gene sequence (encoding the functional proteins) shows remarkable similarities with humans. Both the mouse and human genomes, for example, contain about 3 billion base pairs and their gene sequence shares more than 85% identity [15]. Thus, rodent systems provide a valuable model to study, for example, brain function in health and disease (e.g. epilepsy, Alzheimers disease or stroke).

Nevertheless, the brain of humans shows some notable anatomical as well as functional differences as compared to rodents. While the thickness of the cortex, for example, does not vary substantially in different species (always $\sim$1 - 4 mm), the human cortex shows a dramatic increase in surface area by means of a highly convoluted shape. In addition, while laminar specific similarities of cortical columns are conserved between species [37] the total number of cortical columns is massively increased in humans, presumably providing greater computational power [95]. Therefore, results obtained in the model system eventually have to carefully be reviewed (and verified) in the real system.

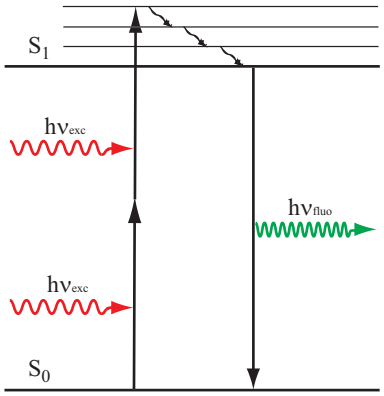

Figure 2.4: Schematic of two-photon excitation. A fluorophore in the ground state S_0 is excited (here to a vibrational level above the first excited state S_1) by simultaneous absorption of two low energy photons. It relaxes down the vibrational ladder to S_1 and usually returns to a vibrational level above S_0 via emission of one high energy photon ($h\nu_{\text{fluo}} \leq 2h\nu_{\text{exc}}$).

2.2 In Vivo Two-Photon Fluorescence Microscopy

Since its inception more than a decade ago [42], two-photon fluorescence microscopy has been widely used in the field of biology and medicine. It has been applied, for example, to study tissues as diverse as brain, skin, lymph nodes and tumors (for reviews see [217] [78] [154]). The theoretical basis of two-photon excitation had been established already in 1931 by Maria Göppert-Mayer [66]. However, the experimental observation [94] of this physical effect had to wait for the invention of the laser as it requires high light intensities. The value of two-photon excitation for microscopy was recognized not until 1990 [42].

2PM is based on quasi-simultaneous absorption of two photons promoting an electronic transition that would otherwise require a single photon of approximately twice the energy (see Fig. 2.4). The probability for such an event is extremely low at ambient intensities [43] and occurs at appreciable rates only at very high intensities (in general $> 10^{17} W/m^2$). Usually, such intensities can only be achieved in the focus of a high numerical aperture (NA) lens using a mode-locked laser-source with sub-picosecond pulse duration. Two-photon absorption is confined to the focal volume which provides inherent optical sectioning without the use of a spatial filter. Unlike confocal microscopes (based on one-photon excitation) this allows the detection of scattered fluorescence photons. Both the detection of scattered fluorescence and the reduced scattering cross-section (increased scattering length) for low energy photons (usually in the infrared) contribute to the capability of the two-photon microscope to provide high resolution images from deep (i.e. several hundred micrometers) within living tissue [43] [217]. In addition, confining excitation to the high-intensity region at the focus not only allows for a significant increase in detection efficiency, but also reduces photobleaching and damage in the out-of-focus volume.

This section aims to introduce the physical principles governing two-photon fluorescence excitation and how these principles expand into the actual instrumentation

of a two-photon microscope. Furthermore, we will discuss some applications as well as limitations to the use of 2PM in biological and medical research. Much of the content of this section has been elaborated in the course of preparing a manuscript entitled 'Two-Photon Laser Scanning Microscopy' (co-authored by Patrick Theer and Fritjof Helmchen) invited for publication in an edited multiauthor book on 'Ultrashort Laser Pulses in Biology and Medicine' (Springer publishing house, Heidelberg).

2.2.1 Instrumentation

General Setup. Two-photon microscopes are laser-scanning microscopes and their architecture is essentially identical to that found in confocal microscopes. In fact, commercial confocal laser-scanning instruments can easily be converted for two-photon operation, generally requiring only the replacement of optics in the excitation path to adapt to the different excitation wavelengths [42]. Furthermore, since in most situations out-of-focus fluorescence is negligible in two-photon microscopy, a confocal pinhole is rarely desirable. This offers the opportunity to employ whole-field detection: all fluorescence photons that enter the objective and are passed by the detection filter, are collected. This not only increases detection efficiency but also allows simplification of the optical design.

A schematic of a generic two-photon microscopy set-up is shown in Fig. 2.5. The main components are an infrared ultra-short pulses emitting laser as excitation light source, scan-mirrors and optics, and a fluorescence detector. Images are obtained by raster scanning the focused laser beam across a specimen. Fluorescence usually is collected by the same objective used for focusing of the excitation light, then separated by a dichroic mirror from the excitation light and focused onto a detector. The detector signal is used to build up the image sequentially in a raster pattern.

Light Source. Excitation light sources that have been used in two-photon microscopy include solid-state lasers such as Cr:LiSAF, Nd:YLF, Nd:glass, and Cr:fosterite, as well as dye- and fiber-based lasers (for a review see [177]). The most widely used excitation light source is, however, the Ti:sapphire laser. Due to its high average power capability ($\sim$1 W), broad tuning range (700 - 1100 nm), short pulse duration ($\sim$100 fs), as well as reliable and robust operation, it has become the light source of choice. Typical Ti:sapphire laser repetition rates f_{rep} are on the order of 100 MHz, well matching the nanosecond fluorescence lifetime of many fluorophores.

Scan Mirrors and Optics. Optics in the excitation path must, of course, be selected for high throughput in the infrared. For the scan mirrors, protected silver coatings should be employed as they offer excellent reflectivity in this wavelength range. Dielectric coatings can provide even better performance but are hardly available for scan mirrors.

Filter. Excitation and emission wavelengths are typically well separated by several 100 nm. Color glass barrier filters (e.g. Schott BG39) can be used to reject infrared stray light. Generally, they have broad transmission windows in the visible wavelength region

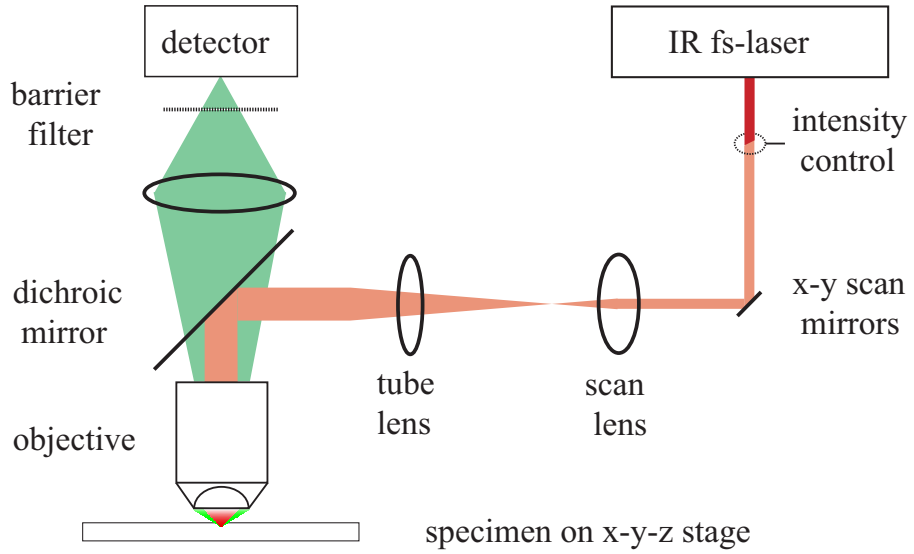

Figure 2.5: Schematic of a generic two-photon fluorescence microscope. The focused laser beam is raster-scanned across a specimen. Fluorescent light emitted by the sample is collected through the objective, filtered and subsequently detected.

but reject infrared light very efficiently.

Fluorescence Light Detectors. With whole-field detection as the preferred fluorescence detection modality in two-photon microscopy, the detection system should ensure collection of most of the fluorescence photons emerging from the specimen. To achieve this, low magnification, high-NA objectives and high-transmission collection optics should be used. In addition, the detection system must be carefully designed to match the objective's effective angular acceptance which generally requires a dichroic mirror and collecting lens with large clear apertures to be placed as close as possible to the objective [142]. Rejection of residual excitation light can be achieved by inserting a barrier filter. The large separation of excitation and emission wavelengths allows for the use of colored glass filters which often provide a better performance than the dielectric filters that are generally required for single-photon fluorescence microscopy. Furthermore, large-area detectors (with several ten mm^2 active area) should be employed for efficient detection, since at large imaging depths most of the collected fluorescence photons will have been scattered before entering the objective. Hence, the light cone emerging from the objective's back aperture will be somewhat diffuse and the minimal spot-size to which this light can be focused is therefore no longer diffraction limited. The circle of least confusion can be quite large, i.e. several mm in radius. In addition, detectors should offer high quantum efficiency at the emission wavelength, and internal gain to avoid excess noise introduced by external amplification. Detectors most suitable for two-photon microscopy are photomultiplier tubes (PMT) and avalanche photo diodes (APD). Although APDs are comparatively superior in terms of

quantum efficiency (∼80%), their small sensitive area, low internal gain (∼ 10^2), and excess noise, limits their range of use. In contrast, PMTs are available with large sensitive areas, quantum efficiencies up to 30%, and high internal gain (> 10^6) with no need for further amplification (for a review on detector designs see [10]).

Simultaneous detection of multiple structures labeled with different fluorophores can be easily achieved in two-photon microscopes. The reason being that two-photon absorption spectra of most fluorophores are relatively broad allowing a wide range of fluorescent dyes to be excited simultaneously, while emitted fluorescence light can effectively be separated into several spectral windows by use of appropriate dichroic beamsplitters.

2.2.2 Fluorescence Excitation

Two-photon excitation requires absorption of two photons within a very narrow temporal window, typically less than 10^{-15} s. The absorption cross section σ describing this process depends linearly on the excitation intensity, i.e. $\sigma = \delta I$ where δ denotes the two-photon absorption cross-section measured in units of Göppert-Mayer (1 GM = 10^{-58} m^4 s/photon). The two-photon absorption rate thus scales with the square of the excitation intensity

$$R_{abs} = \frac{\sigma I}{hc\lambda} = \frac{\delta I^2}{hc\lambda} \tag{2.1}$$

where h, c, and λ are the Planck constant, speed of light in vacuum, and the wavelength respectively.

Owing to the square dependence on light intensity, significant two-photon absorption rates require high photon flux densities in the range of GW/cm^2. Such high photon flux densities can be achieved by temporal and spatial concentration of laser light. Although some two-photon excitation has been demonstrated using spatial confinement alone (by employing high numerical aperture lenses) [74], acceptable average power levels and time-efficient imaging generally requires additional temporal concentration through use of pulsed radiation. Under typical experimental conditions, i.e. fluorescence excitation using a focused pulsed laser beam, the average number of photon pairs absorbed per fluorophore and per unit time is given by [42]

$$n_a = \frac{\delta}{\tau f^2}\left(\frac{\pi(\mathrm{NA})^2}{hc\lambda}\right)^2 \langle P\rangle^2 \tag{2.2}$$

where ⟨P⟩ is the average power, NA is the numerical aperture, f the pulse repetition rate and τ the pulse duration. Note, that Eqn. 2.2 holds true for the paraxial approximation.

According to Eqn. 2.2, the two-photon fluorescence yield can be increased by decreasing the repetition frequency or the pulse duration (assuming constant average power).

This is, however, not generally true for several reasons. First, pulses propagating through coatings and optical glass (e.g. the objective lens or optical fibers) are spread in time due to group velocity dispersion: Light of ultra-short laser pulses consists of a relatively wide range of optical frequencies. Due to the wavelength dependence of the refractive index in optical materials, the various frequency components travel at different speeds (group velocities). This leads to 'chirped' (or frequency swept) pulses which are longer than their originals. Note, that the difference in speed increases with spectral width of the pulse, tantamount to decreases in pulse duration.

Although, in principle, group velocity dispersion induced pulse spreading can be compensated by pre-chirping (e.g. using prism or grating arrangements), compensation becomes instrumentally elaborate when pulse widths much smaller than 100 fs in the focus of high NA objectives are required [126] [41]. In addition, even if pulse spreading could be fully compensated, decreasing pulse duration below the point where its spectral width exceeds the excitation spectral width of the employed fluorophore would decrease excitation efficiency [41]. This sets a lower bound to the minimal desirable pulse duration, which for typical fluorophores (showing two-photon excitation spectral widths between 50 and 150 nm [210] [6]) is between 25 and 5 fs, respectively.

Second, increasing two-photon fluorescence yield by decreasing the repetition rate is limited because Eqn. 2.2 holds true only as long as the excitation probability of a fluorophore per pulse is much smaller than unity. This is due to the fact that the excited-state life-time of most fluorophores (a few nanoseconds) is much longer than the pulse duration ($\sim$100 fs) and thus insufficient to relax to the ground state (a prerequisite for the absorption of another pair of photons). Hence, if the excitation probability approaches unity, saturation effects begin to occur. Even if saturation posed no problem, the excitation pulse repetition rate clearly can not be lower than the rate of image acquisition (typically 50 kHz - 2 MHz), since at least one pulse has to be delivered per pixel.

2.2.3 Fluorescence Detection

Two-photon excitation generally is confined to the focal region and out-of-focus fluorescence is negligible. Hence all fluorescence light emerging from the sample contributes useful signal and as much as possible should be detected. However, for choosing the optimal detection design, the fluorescence-light distribution at the sample surface needs to be known. In general, one can distinguish two border cases. First, imaging in transparent media or scattering samples at depths much smaller than their scattering mean-free-path length l_s and second, imaging at depths z_0 beyond l_s. In the first case, the so called ballistic case, most fluorescence photons emerge unscattered and the collection efficiency ϵ_b (isotropic emission assumed) scales with the solid angle of the objective lens

$$\epsilon_b = \frac{1}{2}\Big(1 - \cos(\theta_{\mathrm{NA}})\Big) \tag{2.3}$$

where θ_{NA} is the half-angle of the objective's angular aperture. A useful approximation of Eqn. 2.3 for low to moderate NA's is given by

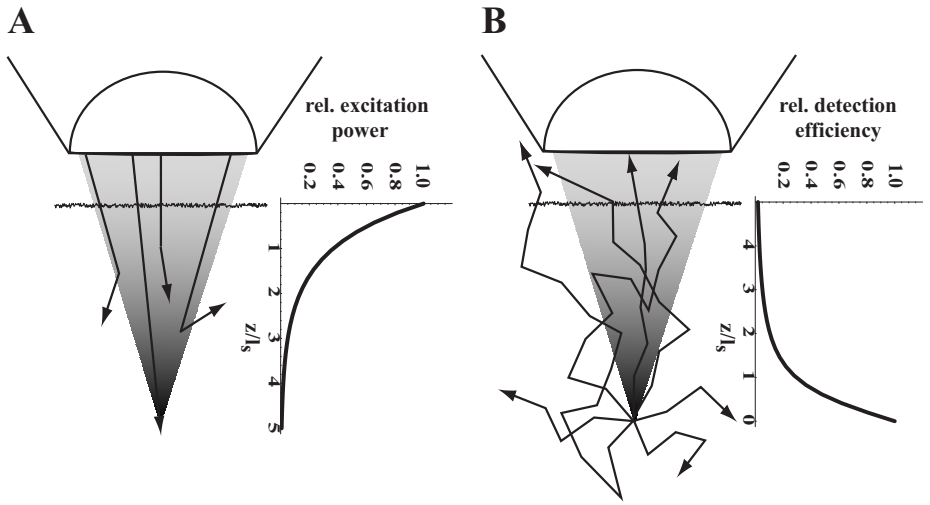

Figure 2.6: Two-photon imaging in scattering media. (**A**) Excitation power decreases exponentially with imaging depth. (**B**) Detection efficiency decreases for large imaging depths $\sim 1/z^2$.

$$\epsilon_b \approx \frac{1}{\pi}\Big(\frac{\mathrm{NA}}{n}\Big)^2 \tag{2.4}$$

The factor 1/2 in Eqn. 2.3 is due to the fact that in the standard collection scheme (epifluorescence-collection), light of only one hemisphere is collected. In certain situations (imaging of thin samples), light emerging from the far side of the sample can also be collected by using the condenser path. In particular, when purely used for detection (i.e. no refractive index match required), high NA oil condensers may be employed, providing up to more than twofold increase in total collected signal [106].

In the second case, i.e. imaging at depths z_0 beyond l_s, most of the fluorescence light reaching the objective entrance aperture will have been scattered resulting in a spread of its spatial and angular distribution. In other words, fluorescence light seems to originate from an extended source in the focal plane (Fig. 2.6). Whether light is collected or not depends no longer solely on its direction but also on its position at the time it leaves the sample.

For intermediate imaging depths where photons experience only a few scattering events (semi-ballistic case), calculations of fluorescence-light distributions are difficult and rely mainly on numerical simulations (Monte Carlo studies). At the limit of large imaging depths ($z_0 \gg l_s$), photons generated at the focus experience a large number of scattering events and emerge with a roughly isotropic angular distribution (diffuse case). In this case, photons may be viewed as performing a random walk (isotropic scattering) starting from a point source deep within a semi-infinite medium until they reach the surface, escape and do not return. For this geometry, the photon density G_F within the medium can be calculated using the method of images [89], i.e. superposing a virtual point sink outside the medium symmetrically to the surface boundary, and is given by

$$G_F(z,r) = \frac{Q}{4\pi D}\left(\frac{1}{\sqrt{r^2+(z_0-z)^2}} - \frac{1}{\sqrt{r^2+(z_0-z)^2}}\right) \tag{2.5}$$

where Q is the fluorescence emission rate, $D = cl_s/3$ the effective photon diffusion coefficient, and r and z the distances from the optical axes and surface, respectively. The fluorescence light intensity at the surface corresponds to the photon flux F_F through the surface and is given by the spatial gradient of the photon density:

$$F_F(z,r) = D\frac{\partial}{\partial z}G_F\Big|_{z=0} = \frac{Q}{2\pi}\frac{z_0}{(r^2+z_0^2)^{3/2}} \tag{2.6}$$

Only light that escapes within a maximum radius $r_{\max}$ and half-angle $\theta_{\max}$, given by the effective field-of-view radius and angular acceptance of the detection system respectively, can be collected. Note, that $r_{\max}$ and $\theta_{\max}$ are not independent parameters and change with imaging depth.

The collection efficiency in the diffuse case ϵ_d is given by the fraction of photons that emerge within an effective field-of-view radius given by the integral of Eqn. 2.6 multiplied by the fraction permitted by the effective angular acceptance of the detection system [12]

$$\epsilon_d = \Big(1-\cos(\theta_{\max})\Big)\left(1-\frac{z_0}{\sqrt{r_{\max}^2+z_0^2}}\right) \tag{2.7}$$

For depths much larger than the field of view ($z_0 \gg r_{\max}$) the detection efficiency scales as $1/z_0^2$. In evaluating Eqn. 2.7 it becomes clear that in order to maximize the collection efficiency of focal fluorescence for deep imaging, a large field-of-view is just as important as a high angular acceptance. The use of low magnification, high NA objectives is therefore of paramount importance in two-photon microscopy. In fact, it has been shown, that using a special low magnification, high NA objective (Olympus XLUMPlanFl 20×/0.95W), the detection efficiency can be increased by a factor of 10 compared to a standard 60×/0.9 NA objective [142]. However, in order to maximize the benefit, the entire detection path has to be adapted accordingly. This usually requires large clear-aperture optics and large-field detectors with an appropriate acceptance angle.

2.2.4 Spatial Resolution

Two-photon microscopes are diffraction-limited in resolution to ∼0.3 μm laterally, and ∼0.8 μm in axial direction. Theoretically, spatial resolution of a two-photon microscope is somewhat reduced, as compared to an ideal confocal microscope (using the same fluorophore). This is because the excitation wavelength in two-photon microscopes is roughly twice the wavelength used in confocal microscopes [170] [70]. In practice, however, the difference is much less, because the finite pinhole size (which is needed for efficient detection

in confocal microscopes [71]), chromatic aberration, and imperfect alignment of laser focus and detector pinhole all degrade resolution in the confocal microscope.

The resolution of a two-photon microscope can be improved by using confocal detection [178]. However, this comes at the cost of reduced collection efficiency (particularly for scattering samples) and with more severe chromatic aberration. Without confocal detection and using two-photon excitation, chromatic aberration in the objective is only a minor concern. For highly chromatic systems (e.g. acousto-optical modulators), however, even the small spread of excitation wavelength that results from the shortness of the laser pulses (needed to achieve efficient two-photon excitation) cannot be ignored [40].

The resolution of two-photon images can be further improved by deconvolution methods [2] [88] (which might be particularly useful when looking at tiny structures, such as dendritic spines that are only a few micrometers in length). Various algorithms have been developed for efficient implementation of this computationally intensive procedure. Through their use, resolution in raw images can be improved by a factor of two or more [169]. Image deconvolution in two-photon microscopy, however, requires knowledge of the imaging system's point spread function (PSF; the image of a point is the PSF, and thus the image of a complex structure represents the convolution of the points in that structure with the PSF). Although the PSF can be empirically determined (e.g. by imaging subresolution particles) and succesfully applied for refinement of raw images taken from thin specimens, its aberration in vivo forms a major obstacle to in vivo image enhancement.

2.2.5 Temporal Resolution

The temporal resolution of a two-photon microscope depends on the scan mirrors employed. High-speed video rate 2PM has been demonstrated using resonant galvanometer mirrors, or by illuminating many spots simultaneously using microlens arrays. So far, full-frame scan rates up to 225 Hz (video rate is 25 - 30 Hz) have been demonstrated [17]. However, since dynamic changes are often confined to small sub-regions within a frame scanning of only a few lines often proves sufficient. In this way, acquisition rates of up to 1 kHz can be achieved.

The mass of the galvanometer mirrors, however, makes it difficult to achieve scan rates beyond the 1 kHz range (which would allow to observe, for example, phenomena such as ion redistribution during neuronal action potentials). Higher scan rates can be obtained with acousto-optic modulators (AOMs) [61], though at the cost of spatial resolution (see above) and available average power. AOMs use sound to induce refraction waves that behave like a diffraction grating, i.e. the degree of refraction is wavelength dependent.

2.2.6 Depth Penetration

One of the main advantages of two-photon microscopy is its increased depth penetration as compared to one-photon imaging techniques when used in highly scattering tissue,

such as brain tissue. This advantage is due to two unique properties of two-photon microscopy: First, highly localized fluorescence excitation, allowing efficient fluorescence collection (see above). Second, reduced excitation light scattering through use of longer wavelength light (typically, near-infrared excitation light is used in two-photon microscopy). Both these properties contribute to the ability of two-photon microscopy to provide high resolution images from deep within living tissue (as demonstrated in this thesis).

However, given the wide range of optical tissue properties (which depend, for example, on cellular content, vascularisation, etc.) it is difficult to provide definite numbers for maximum imaging depths attainable in a given tissue. It is clear, though, that imaging beyond the point at which the focal fluorescence signal drops below the photon shot-noise level is not feasible. While the point at which this occurs depends on imaging parameters such as laser power, staining strength, detection efficiency, pixel dwell time, etc. it may be defined by postulating a certain signal-to-noise (S/N) ratio. One way of doing this is to stipulate a minimum average focal excitation power $\langle P_{\min}\rangle = \langle P\rangle \exp(-z_{\max}/l_s)$, corresponding to a minimum number of photon pairs $n_{\min}$ absorbed per fluorophore and unit time. Using Eqn. 2.2, the maximum imaging depth is thus given by

$$z_{\max} = l_s \ln\left(\sqrt{\frac{\delta}{n_{\min}\tau f}}\frac{\pi(\mathrm{NA})^2}{hc\lambda}\langle P\rangle\right) \tag{2.8}$$

which depends linearly on the scattering mean-free-path length l_s and logarithmically on the excitation power P and duty cycle τf. Therefore, a significant increase in maximum imaging depth could be achieved by a significant decrease in duty cycle or increase in excitation power.

The average excitation output power of light sources commonly used in two-photon microscopy (mainly mode-locked Ti:Al_2O_3 lasers providing 100 fs pulses at ∼100 MHz repetition rate), however, is limited to ∼1 W. This allows maximum imaging depths of about 2 - 3 scattering-mean-free-path lengths. The actual value of l_s depends on the type of tissue. Hence, the actual imaging depth can be quite different for varying specimens. In the cornea of the eye, for example, an autofluorescence image can be obtained from depths beyond a millimetre, whereas inside highly scattering specimens such as human skin, the contrast of autofluorescence is significantly degraded at 200 - 300 μm distance from the surface. [104] [185]. As a result, efforts to increase imaging depth have mainly concentrated on improving fluorescence excitation and collection efficiency. In particular, investigations on the role of the detection optics' angular and area acceptance have revealed the importance of using high numerical aperture and field-of-view lenses [142] [12]. Using a 20×/0.95 NA objective (Olympus) instead of a 'standard' 60× lens, for example, has been predicted to increase imaging depth by about 100 μm in brain tissue [142].

The excitation efficiency (and thus imaging depth), in addition, can be increased by decreasing the laser duty cycle τf, lowering either the pulse repetition rate or pulse duration (within the limits discussed above). Pulse widths as short as 15 fs have been demonstrated in the focus of a high numerical aperture objective [126], corresponding to a 7-fold increase in excitation efficiency as compared to the 'standard' 100 fs laser pulses.

Much larger increases in excitation efficiency, however, can be expected from lowering the laser repetition rate [13], which can be achieved either by increasing the cavity length of the oscillator [29] or cavity dumping [156]. Both methods, however, result in a significant decrease in available average power. This can be avoided by use of a regenerative amplifier, for which repetition rates of up to 400 kHz have been demonstrated [141]. Considering a typical pixel-rate between 50 kHz and several MHz as lower bound for the pulse repetition frequency (since at least one laser pulse has to be delivered per image pixel) an up to 2000-fold increase in excitation efficiency can be achieved as compared to a standard 100 MHz oscillator (assuming that the same average power is provided by the oscillator and amplifier). Using Eqn. 2.8, this translates in an increase in penetration depth by up to 3.8 scattering mean-free-path lengths.

Yet, regardless of any improvements in excitation power or efficiency imaging depth cannot be increased ad infinitum. Rather, imaging depth is fundamentally limited by the onset of substantial out-of-focus fluorescence generated near the sample surface [213] [187]. This can be understood as follows: In order to maintain constant signal strength (from deep-lying fluorophores) the incident laser power has to be increased exponentially with depth. For large imaging depths, however, this exponential increase in power starts to dominate the decrease of excitation efficiency caused by the increase in beam cross section (scaling quadratically with depth). Eventually, this leads to generation of two-photon excited fluorescence near the sample surface comparable to or exceeding that produced in the focal volume. Hence, in this case, the assumption of two-photon fluorescence excitation being confined to the focal region holds no longer true.

2.2.7 Further Considerations

The viability of the biological specimen is of paramount importance for any living-tissue imaging technique. Thus, in addition to the physical constraints discussed above, optimization of two-photon excitation efficiency is also limited by the degree of photodamage the specimen can tolerate. In particular, two-photon absorption has been associated with different mechanisms of light-induced damage, such as thermal and photooxidative damage [106] [87] [107]. As a rule of thumb, excitation intensity should be set to a level just enough to generate sufficient fluorescence. However, if peak-intensity related problems persist, increasing the pulse duration or the focal volume (e.g. by underfilling the objective's back-aperture) might improve the situation yet reduce S/N ratio.

Note, that excitation efficiency greatly depends on the fluorophore's absorption cross-section δ. The higher the dye's quantum efficiency, the less the excitation power required for imaging and the deeper one can peer into tissue. In addition, optimizing the fluorophores' two-photon absorption properties helps to improve specimen viability. Recently, fluorophores with large two-photon-absorption cross sections ($\delta > 1{,}000$ GM, i.e. one to two orders of magnitude larger than that of commonly used fluorescent probes; see table table 2.1) have been synthesized [5] [113], yet their in vivo applicability is currently rather limited [125].

Although most fluorophores can be excited at twice the wavelength of their one-

photon absorption maximum, two-photon excitation spectra are often significantly different from their one-photon counterparts [210]. This is due to the different parity selection rules that apply to one and two-photon transitions. For symmetric molecules, for example, quantum parity reverses between one-photon and two-photon excitation processes. Thus, molecular states that are accessible with one-photon excitation may not be accessible in the two-photon case and vice versa. In particular, in a number of fluorophores the two-photon excitation spectrum shows a significant blue shift (i.e. a shift towards higher energy transitions) as compared to their one-photon counterpart [6], while at the same time no red shift has been reported so far. A possible explanation might be that fluorescence emission will only occur for transitions from one-photon allowed excited states, i.e. although lower excited states might be accessible via two-photon absorption those will not be fluorescent. This notion is supported by the fact that fluorescence emission spectra under one- and two-photon excitation are usually identical [210]. Hence, the same excited state is occupied before the system relaxes to its ground state. In this case, fluorescence quantum efficiency for one and two-photon excitation can expected to be equal. The transition from the two-photon excited state to the fluorescent one photon excited state most likely is achieved through vibrational coupling [6]. Therefore, since calculation of two-photon cross sections and quantitative predictions on the basis of known one-photon cross sections are difficult, choosing the optimum wavelength for two-photon excitation heavily relies on specific measurements of two-photon absorption spectra.

2.3 In Vivo Fluorescence Labeling

2PM as a fluorescence imaging technique heavily relies on appropriate fluorescent staining methods to visualize biological structure and function. Fluorescent staining can be intrinsic to the object under investigation - autofluorescence of pyridine nucleotides (NADH and NADPH), for example, has been used to probe the metabolic state of cells [96] and to monitor redox states in cornea and skin [175]. Most intrinsic fluorophores, however, offer very low two-photon cross-sections (see table 2.1) limiting the range of applications. Thus, in most cases fluorophores have to be introduced from the outside using appropriate staining techniques.

Generally, staining techniques comprise two essential components, the fluorescent marker(s) and the loading technique(s), which introduces the marker to the object under investigation. Ideally, staining techniques should be

1. easy and safe to perform. This is of particular concern, for example, when using viral infection as labeling technique (see below).

2. highly specific, for example, concerning the cell type to be labeled or brain region to be affected.

3. highly efficient. Fluorophores, for example, should offer large two-photon cross-sections, broad absorption, and narrow emission spectra.

4. stable for a period considerably longer than the average lifetime of the process under investigation.

5. minimally invasive, thus avoiding alterations of the object under investigation or its environment (in some cases, however, one might want to achieve the exact opposite, for example, when interested in cellular mechanisms of repair).

6. capable to report biological function, for example, through dependence of fluorescence intensity on ion concentration or membrane voltage.

In practice, none of the currently available staining techniques fulfills all these requirements. As a result, staining techniques generally have to be combined in order to address a specific question.

2.3.1 Fluorescent Markers

Fluorescent markers typically are organic molecules that emit fluorescence light upon excitation with photons of appropriate wavelength. They can be subdivided into anatomical and functional markers, although the transition between those categories is fairly smooth. While anatomical markers serve to visualize cell morphology, subcellular localization or transport processes, functional markers are employed to report cell signaling (such as action potential firing or ion level changes) through changes in fluorescence intensity. Indicator molecules can be entirely synthetic, entirely genetically encoded macromolecules, or hybrid combinations, each approach having its specific strengths and weaknesses [196]. In particular, indicator molecules are designed to maximize sensitivity and specificity for improved specimen viability and more targeted applications, respectively.

Genetically Encoded Indicators. One of the probably most prominent indicator molecules is the green fluorescent protein (GFP) [195], that has been isolated from the jellyfish Aequorea victoria in the 1960s [171] and allows genetic encoding of strong visible fluorescence in host cells (see subsections 3.3.1 and 3.3.3 for applications). Meanwhile, numerous spectral variants of GFP have been presented [168] [25] providing improved absorption cross-section, quantum yield, and other favorable features such as improved folding behavior, temperature and pH sensitivity. Fluorescent proteins (FPs) have successfully been employed in various biological systems, particularly in mice and zebrafish. They can serve, for example, as gene expression markers or, if tagged to a protein of interest, as reporter of protein localization. Furthermore, mutagenesis and engineering of FPs into chimeric proteins has yielded genetically-encoded indicators capable to sense cellular activity through changes in intracellular calcium [68] [130] [128] (see also subsection 3.4.1.2).

Synthetic Indicators. Synthetic fluorophores are available in a variety of different colors and have been employed for various purposes. Tail vein injection of fluorescein

isothiocyanate-labeled dextran, for example, has enabled measurements of cortical blood flow [104], while quantum dots (i.e. fluorescent semiconductor nanocrystals), for example, have been used to study intracellular processes such as the diffusion of individual glycine receptors in neurons, or to identify lymph nodes in live animals [125]. Synthetic dyes, in addition, have been applied to label cell populations [163] (see also subsection 3.3.2), senile plaques [30] and various other tissue components.

Of particular importance to biological research are functional synthetic indicators, the most prominent being ion indicators. Ion indicators for calcium, magnesium, sodium, heavy metals, pH and other ions exist. Calcium indicators, for example, allow (indirect) measurement of cellular activity. They bind to intracellular signaling molecules [196] [216], and with different affinity. Ca^{2+} indicators have been extensively used to study single-cell and population activity, both in tissue slice preparations and in living animals [82] [185] [181] [108] (see also subsection 3.4.2.2). Note, however, that calcium indicator based imaging of cellular populations in vivo [181] [138] was not available at the start of this thesis.

A direct monitoring of membrane voltage has been achieved with voltage sensitive dyes (VSDs), that have been employed, for example, to record population-activity of neuronal circuits in the invertebrate Aplysia [58]. VSDs, however, are difficult to handle as signals generally are small and photodamage can be large.

Some commonly used indicator molecules together with their major two-photon excitation associated properties are shown in table 2.1.

Fluorophore	**2P Exc. Wavelength** *[nm]*	**Max. Emission Wavelength** *[nm]*	**2P Abs. Cross Section** *[GM]*	**Example Applications**
Extrinsic				
Cascade Blue	750	423	∼1	
Alexa 488		519		
Lucifer Yellow	860	533	∼1	Labeling of
Rhodamine B	840	600	∼200	single cells
Texas Red	780	615		
Alexa 594		617		
Fura-2 Calcium	700	362	12	Functional labeling of
Indo-1 Calcium	700	405	1.5	single cells and
Calcium Green	725 - 780	531		cellular networks
Fluorescein	∼780	520	∼40	Staining of
Quantum Dots	design specific	design specific	2,000 - 47,000	blood plasma
Intrinsic				
GFP	800 - 850	516	∼6	Labeling of
EGFP	900 - 950	516	∼113	cell populations,
YFP	970	524	∼50	subcellular compartments,
RFP	990	583	∼100	etc.
NADH	∼700	465	∼0.02	Probing of
FMN	∼700	513	∼0.8	metabolic processes

Table 2.1: Some common extrinsic and intrinsic indicator molecules (taken from [76] [110] [175] [212] [210] [211] [147]).

2.3.2 Loading Techniques

In the following, we will briefly review loading techniques currently available for staining of cortical structures in vivo. Note, however, that major techniques for in vivo staining of cellular populations first evolved during the thesis and that the development of such techniques was one of its major aims.

Physical Methods. Provide a way to introduce indicator molecules into single cells and small populations of cells as well as other cortical elements (e.g. the cortical microvasulature) [104]. Physical methods for cell labeling include intracellular dye loading via sharp microelectrodes or patch pipettes [82] (commonly used to stain single cells), single-cell electroporation (SCE) [72] [159], and biolistics [101]. In particular, SCE employs electrical pulses to briefly disrupt the cell membrane allowing charged indicator molecules to enter via electrophoresis, while in biolistics a 'gene gun' is used to shoot dye- (or DNA)-coated gold or tungsten particles into tissue resulting in dye dilution and diffusion (or protein expression) from the particles trapped inside cells.

The major disadvantage of all these techniques is, that typically only one or a few cells are labeled. Furthermore, labeling is often uncontrolled, i.e. the selection of cells is more or less random. However, a recent approach now allows to specifically target identified cells in the intact brain [122].

Chemical Methods. Allow in vivo labeling of small cellular populations. For example, multi-cell bolus loading (MCBL) of the acetoxy-methyl(AM)-ester forms of calcium indicator dyes recently has enabled functional staining of hundreds of cells in the intact brain [181]. In particular, this approach (that has also been employed in this thesis; see subsection 3.4.2.2) is based on neutralizing the charged side groups of fluorescent indicators with AM-esters, making them membrane-permeable. Once inside the cell, the uncharged ester groups are cleaved by non-specific esterases, restoring the fluorescent indicator molecules. Furthermore, local uptake of the dextran-conjugated form of ion indicators was used for retrograde labeling of small cellular networks as well as anterograde labeling of projection pathways [108] [14].

The main drawbacks associated with chemical methods are, however, their temperature-dependence [14] and low specificity (MCBL, for example, labels both neurons and glia).

Viral Infection. Method for inducing gene expression in a defined subpopulation of cells in vivo [53], thus allowing targeted and specific labeling of small cellular populations (see subsection 3.3.1). Typically, a solution of replication-incompetent viral particles is injected directly into the tissue. Depending on the specificity of the virus, a specific subpopulation of cells gets infected in the immediate vicinity of the injection site. Expression of the transgene, e.g. GFP, is controlled by the promoter. Various viral expression systems have been developed, which differ with regard to cloning capacity, expression level, labeling onset (also called 'lag phase'), cell specificity, and cytotoxicity (see table 2.2).

Viral infection offers unparalleled transfection efficiencies. In addition, virus-mediated labeling

	Cloning capacity *[kb]*	**Lag phase** *[d]*	**Neuron specificity**	**Biosafety level**
Sindbis/Semliki Forest Virus	6.5	1 - 2	++	2
Adeno-Associated Virus	4.9	13 - 15	+/++	1
Lentivirus	9.0	7 - 14	+/++	1
Measles Virus	4.8	2 - 3	+	2

Table 2.2: Comparison of commonly used viral expression systems for gene transfer in vivo [53]. The specificity of expression depends on the internal promoter.

provides high S/N ratio (in contrast to MCBL; see above), allowing to resolve even fine cellular structures such as dendritic spines and axons [116] [102] [48]. Functional labeling, however, is complicated by the lack of appropriate genetically encoded indicators (see also subsection 3.4.1.2).

Genetics. Allows cell-type specific labeling of large cellular populations. FP expression in a subset of cells is achieved through genetic manipulation at the pre-embryonic stage. Specificity is achieved by use of cell-type specific promoters. In this manner, many transgenic mouse lines have been produced, in which GFP or its spectral variants are expressed in different cell types, such as neurons, astrocytes and microglia [73] [57] [139] [93] [219]. Transgenic mice, expressing GFP in astrocytes or microglia have also been used in this study (see subsections 3.3.2 and 3.3.3).

However, even the most specific genetic designs affect entire cell populations in multiple brain regions. Thus, current transgenic technologies do not allow targeting of small neuronal networks, complicating the study of subcellular compartments. In addition, only few mouse lines exist, that express functional indicators [75].

For a summary of important features of the above-mentioned loading techniques see table 2.3.

	Genetics	**Viral Infection**	**Chemical Methods**		**Physical Methods**		
			Bolus Loading	*Lipofection*	*Electroporation*	*Biolistics*	*Patch-Clamp*
Specificity	Depending on promoter	Depending on promoter	Unspecific	Variable	Specific *(under visual guidance)*	Unspecific	Specific *(under visual guidance)*
Labeling Onset	Genetically encoded	Depending on viral system	Rapid (< 1 hour)	Hours	Rapid (< 1 hour)	Hours	Rapid (< 1 hour)
Labeling Extent	Large population of cells	Small population of cells	Large population of cells	Small population of cells	Single cells to small populations	Large population of cells	Single cells
Labeling Stability	Stable	Depending on viral system	Hours	Hours	Hours	Hours	Hours
Functional Labeling	Not yet mature	Not yet mature	Possible	Possible	Possible	Possible	Possible
Multicolor Labeling	Possible	Possible	No	No	Possible	Possible	Possible *(not common)*
Toxicity	Minimal	Depending on viral system	Minimal	Variable	Minimal *(when optimized)*	Minimal *(when optimized)*	Minimal
Example Application	Cellular development	Molecular pathways	Network activity	Small network activity	Small network activity	Network activity	Single cell activity

Table 2.3: In vivo staining techniques.

2.4 Miniaturization of Two-Photon Fluorescence Microscopy

Owing to its exceptional depth penetration and intrinsic optical sectioning properties, 2PM has become the principal technique for high-resolution imaging in the intact brain. Imaging experiments in the majority of cases are performed under anesthesia. This not only guarantees a state free of pain for the animal, but also eliminates a major source of motion artifacts. Anesthesia, however, alters cortical dynamics and, in turn, single-cell activity, which depends on synaptic background activity, inhibition, and modulatory pathways [161] [112]. One approach to overcome this limitation is imaging in awake, head-restrained animals, that have been trained to keep still while an experiment is conducted. However, this approach inevitably suffers from a rather limited behavioral repertoire. Thus, for studies aiming to investigate, for example, the cellular computations underlying cortical decision making a method for high-resolution fluorescence imaging in the brain of awake, behaving animals would be of great benefit.

Recently, two-photon microscopy has been extended from anesthetized, head-stabilized to freely moving animals through the technical implementation and application of a miniaturized head-mounted microscope [79]: Pulsed near-infrared laser light was conducted through to a single-mode optical fiber to a miniature head-mounted microscope. Fiber delivery of excitation light allowed to decouple bulky optical components (laser, telescopes, etc.) from parts indispensable for image generation and acquisition at the animal's head. Latter components, in addition, were miniaturized to yield an imaging device that could be carried around by the animal.

However, two-photon imaging was handicapped in several respects. First, propagation of ultrashort light pulses (∼100 femtoseconds initial width) through a single-mode optical fiber resulted in severe pulse broadening (up to 1 picosecond at the maximum average output power of ∼180 mW). This temporal broadening, which significantly impaired efficient two-photon fluorescence excitation and thus imaging depth, was mainly due to two physical phenomena, namely group-velocity dispersion (GVD) and self-phase modulation (SPM). Briefly, GVD is based on the wavelength dependence of the refractive index and causes long-wavelength ('red') parts of the pulse spectrum to travel faster in the fused silica material of the fiber than those from the short-wavelength ('blue') parts [3]. As a result, pulses acquire a positive linear frequency modulation (also called 'chirp'). As a linear effect, GVD can be easily compensated for by special arrangements of prisms [63] [135] or diffraction gratings [191]. In contrast, SPM is a nonlinear effect that changes the wavelength spectrum [3]. SPM is based on the intensity dependence of the refractive index, which becomes effective above a certain peak pulse intensity. Hence, different parts of the pulse become affected differentially. SPM is exacerbated in single-mode optical fibers (due to the spatial confinement of pulse energy) and is difficult (if not impossible) to compensate for by pre-chirping (i.e. dispersion compensation prior to light coupling into the fiber). Yet, pre-chirping constituted the most effective way to achieve (partial) dispersion compensation in the fiber microscope and a compact design of the headpiece at the same time (for more details see [135]).

Second, two-photon imaging using the miniature microscope was hampered by lack of efficient fluorescence labeling techniques. Cells had to be labeled individually via micropipettes. Due to the limited control over the location of cell labeling and the limited lateral mobility of the head-mounted fiber microscope, individual stained cells were difficult to find. In addition,

inefficient fluorescence excitation (due to fiber dispersion-induced pulse broadening) hampered two-photon imaging under unfavorable conditions (e.g. a weak fluorescent stain or overlying blood vessels). Furthermore, labeled cells often were found damaged in consequence of micropipette retraction after filling.

Helmchen et al. concluded, that several technological developments or refinements would be necessary to improve fiber microscope performance, and to yield a practical tool for imaging of cellular activity in behaving animals:

1. Efficient labeling techniques: Staining methods that provide rapid, specific and reliable labeling of cell populations, would greatly simplify the application of the fiber microscope as they permit selection of stained cells at a location suitable for imaging. In addition, such methods (be it on their own or in combination with other methods) need to provide functional imaging capabilities (i.e. a visualization of the activity patterns of the stained cells).

2. Improved fluorescence excitation: As the two-photon absorption rate depends quadratically on average (fiber) output power and inversely on pulse length (see Eqn. 2.1), this means that adoption of more sophisticated pulse compression schemes with increased light transmission properties and/or use of special fibers with reduced fiber dispersion would significantly improve imaging depth. Improved fluorescence excitation, in addition, would reduce the probability of causing photodamage to the tissue.

3. Improved positioning: A microscope design that in addition to remote focusing permits remote positioning of the field of view (FOV) would alleviate the difficulty of finding specific dye-filled cells and allow selection of places suitable for imaging. Furthermore, a remote fine-positioning ability would permit easy readjustment of the FOV following lasting lateral image shifts due to animal movement.

4. Advanced fluorescence detection: Fluorescence collection through a large-core (multimode) fiber with subsequent fluorescence detection by a fixed PMT (instead of using a head-mounted one) would reduce fiber microscope weight. In addition, this scheme would abolish restrictions on detector type, size, and weight and enable simultaneous imaging in multiple wavelength channels.

5. Miscellaneous: Advanced microscope miniaturization might involve the development of a custom-made light-weight objective lens with improved fluorescence collection and transmission properties.

This was the starting point of this thesis, and one of its major goals was to overcome the remaining technological hurdles described above. Solutions to all of the above-mentioned issues are presented in the following chapter. In addition, we present an ultra-small and lightweight variant of a fiber microscope, as well as a variety of applications to the in the course of this thesis newly developed labeling techniques.

Chapter 3

Results

The main objective of this thesis was to advance two-photon microscope miniaturization towards high-resolution imaging of cellular network activity in behaving animals. As two-photon microscopy heavily relies on appropriate fluorescence labeling techniques to visualize biological (structure and) function, we therefore put considerable effort in concomitant development and evaluation of appropriate fluorescence labeling techniques.

The following sections present the advances we made in both areas (i.e. in microscope miniaturization and fluorescence labeling). Our results on fiber-based two-photon microscope miniaturization are presented in section 3.1 and published in [136] [65] [64]. Section 3.2 demonstrates the applicability of our miniature two-photon fiber microscopes to fluorescence imaging in vivo through combination with fluorescence labeling techniques (which are described in section 3.3). Section 3.3 presents and evaluates novel staining techniques for imaging of cell populations in vivo, while section 3.4 presents applications to the newly developed labeling techniques in the intact cortex (published in [137] [138] [48] [102]). Both evaluation and application of fluorescence staining techniques was performed on a standard two-photon microscope setup.

3.1 Advancements in Microscope Miniaturization

In subsection 3.1.1, we present a new version of a miniaturized two-photon microscope based on fluorescence excitation through a single optical fiber, that is improved in several respects: (a) Efficiency of two-photon excitation, (b) adjustability of the FOV, (c) multiple-wavelength channel detection capability, and (d) weight. Application of the improved miniature microscope to in vivo imaging of cellular networks is demonstrated in section 3.2. Furthermore, we present the design of an ultra-small and light variant of a miniature two-photon microscope based on a flexible coherent fiber bundle and a gradient-index lens objective in subsection 3.1.2. In vivo application of the fiber-bundle microscope is described in section 3.2.

3.1.1 Single Fiber Based Two-Photon Microscope

The experimental setup of the improved miniature microscope based on fluorescence excitation through a hollow-core photonic crystal fiber (PCF) is shown in Fig. 3.1A. Femtosecond laser pulses

were generated by a Ti:sapphire laser system (Coherent; 76 MHz repetition rate, ∼100 fs initial pulse length). Laser excitation light was coupled into a ∼1.5 m long hollow-core PCF (HC-800-01; BlazePhotonics) with an $f = 18.4$ mm aspheric lens (Geltech) and conducted to the miniature head-mounted microscope (Fig. 3.1B). Lissajous image scans in the head-mounted microscope were achieved using a custom-made resonant fiber scanner [79]. Excitation light was deflected by a tiltable silver coated mirror (Linos; 6 mm diameter), collimated with an $f = 15.4$ mm aspheric lens (AR Coating: 600 - 1050 nm; ThorLabs) and focused through a miniature water-immersion objective (M. Throl Opt. Systems; 0.9 NA; 1.1 g; 1.0 mm working distance in water; transmittance: 87% between 500 - 650 nm, and 85% between 800 - 1100 nm). Fluorescent light was collected through the objective, separated from the excitation light by a 570 nm dichroic mirror (CALFLEX X; Linos) and coupled into a ∼1.5 m long supplementary large-core optical plastic fiber (M02-534, Edmund Industrie Optik GmbH; 980 μm inner diameter; 0.19 dB/m max. attenuation) with an $f = 4.5$ mm aspheric lens (AR Coating: 350 - 600 nm; ThorLabs). Fluorescence light was detected distal to the head-mounted microsope using a pair of stationary photomultiplier tubes (R6357, Hamamatsu) (see subsection 7.1.1 for more details). As compared to the original design, the enhanced miniature microscope is considerably reduced in both size ($5.5 \times 3.0 \times 1.8$ cm^3 now; $7.5 \times 3.0 \times 2.0$ cm^3 then) and weight (11 g now; 25 g then).

In the following, we will describe the major technological improvements in this new design of a miniature fiber-microscope. A detailed description of its operation mode is given in subsection 7.1.1.

Distortion-Free Delivery of High-Energy Femtosecond Pulses Through a Hollow-Core Photonic Crystal Fiber. First, we evaluated pulse propagation of laser excitation light in a hollow-core PCF for the purpose of efficient two-photon excitation at the fiber output. Hollow-core PCFs are radically different from conventional step-index fibers in that they guide light in an air core by so-called Bragg photonic bandgap guidance [34] (instead of total internal reflection), thereby minimizing dispersion and nonlinear effects. The hollow-core PCF used in our study had a 9 μm air core surrounded by a 40 μm diameter microstructured cladding (Fig. 3.2A) and a transmission window (loss <240 dB/km) in the 800 - 850 nm range. Hollow-core fiber dispersion is dominated by waveguide dispersion, which changes from normal to anomalous dispersion in the transmission window. For the fiber investigated here, the zero-dispersion wavelength is near 810 nm.

The pulsed laser beam was launched into the fiber with an $f = 18.4$ mm aspheric lens (Geltech) with no prechirp applied. A diffusion-type GaAsP photodiode (Hamamatsu) was used as a nonlinear detector for interferometric measurement of two-photon-induced photocurrent [157]. With a fresh cleave 50% and more of the input intensity could be readily transmitted through the hollow-core fiber. Near- and far-field images of the output beam were acquired with a video camera (Fig. 3.2). The near-field intensity distribution displayed a hexagonal shape because of the core geometry. The intensity was mostly confined to the central air core, with the outer wings of the profile extending slightly into the inner rings of the photonic crystal. Both near- and far-field distributions showed nearly Gaussian cross-sectional profiles, indicating that with proper fiber coupling light propagated primarily in a fundamental mode with a full width at half-maximum of ∼6 μm (Figs. 3.2C and 3.2E). Higher-order modes could, however, be observed when fiber coupling was misaligned. As shown for a similar fiber, such higher modes experience strong attenuation, and coupling between the low-loss mode and higher modes is weak [23]. Although the fiber thus is not intrinsically single

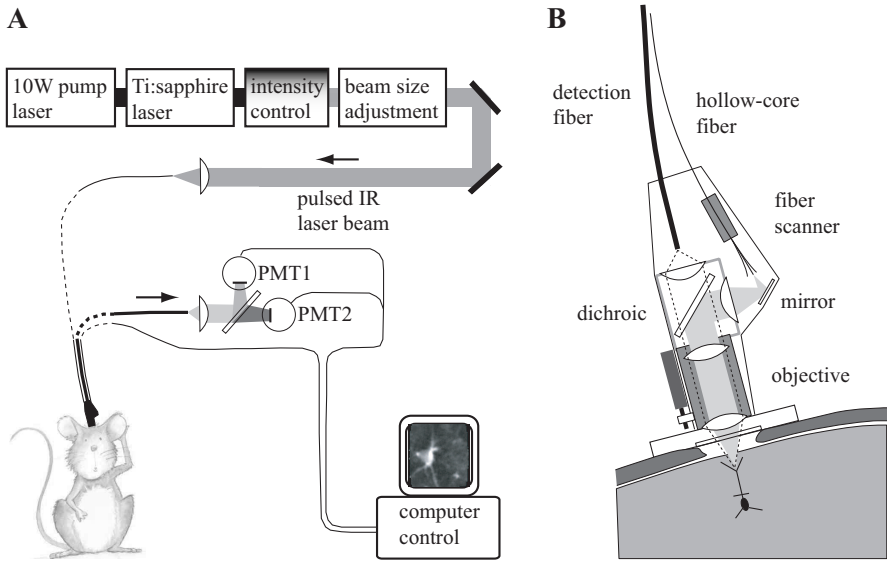

Figure 3.1: Improved miniature two-photon fiber microscope setup. (**A**) Infrared femtosecond laser pulses were coupled into a 1.5 m long hollow-core PCF and conducted to a head-mounted microscope. Fluorescent light was collected through the objective and a supplementary large-core OPF. Two-channel fluorescence detection was implemented at the remote end of the large-core OPF using two PMTs. (**B**) In the microscope headpiece, light emerging from the hollow-core PCF tip was collimated and focused trough a water-immersion objective, which can be remotely positioned with the help of a small DC motor. Resonant vibrations of the fiber tip were used for scanning (see subsection 7.1.1).

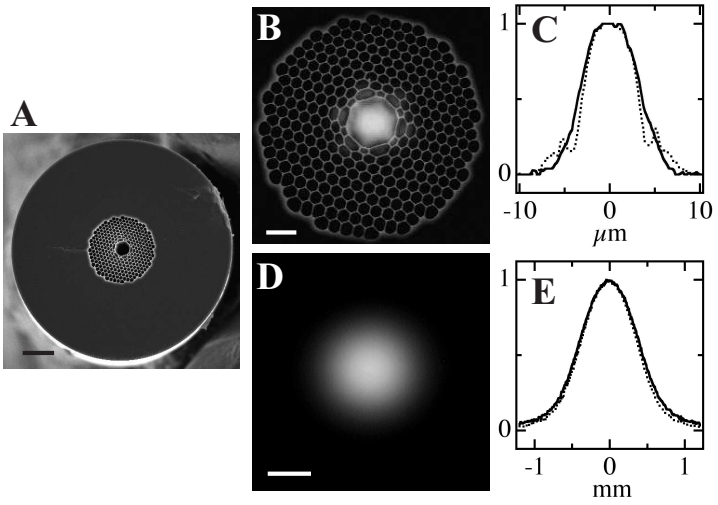

Figure 3.2: (**A**) Scanning electron micrograph of the hollow-core PCF. Scale bar, 20 μm. (**B**) Near-field intensity distribution at the fiber output overlaid on the scanning electron microscope image. Scale bar, 5 μm. (**C**) Intensity profiles of the near-field distribution along two orthogonal directions. (**D**) Far-field beam profile at 5.9 mm distance from the fiber end. Scale bar, 0.5 mm. (**E**) Far-field intensity profiles along two orthogonal directions.

mode, quasi-fundamental mode propagation can be ensured by optimizing fiber coupling and by using sufficiently long fiber pieces.

We measured the autocorrelation and the spectrum of the output pulses for different center wavelengths at low (2 mW) and relatively high (250 mW) average output power, respectively (Fig. 3.3). The relative broadening of both the temporal and the spectral width compared with the input pulses was analyzed over the 790 - 850 nm wavelength range. While the spectral width was preserved at all wavelengths, the pulse broadening factor showed a clear minimum at a wavelength of approximately 812 nm. Importantly, this wavelength dependence was independent of the average transmitted power, demonstrating that broadening is caused by fiber dispersion and that nonlinear effects appeared to be absent even at 250 mW output power. Near the zero-dispersion wavelength autocorrelation traces were almost identical to those of the input pulse. Well below and above the zero-dispersion wavelength the output pulses were significantly broadened, with the autocorrelation traces indicating a linear chirp (Fig. 3.3A).

We further characterized pulse propagation by measuring the pulse duration and the spectrum as a function of average output power at the optimal wavelength of 812 nm (Fig. 3.4). Both the interferometric autocorrelation and the spectrum at the fiber output showed only minor changes compared with the input pulse, even at high average output power of 350 mW, which corresponds to pulse energies of $\sim$4.6 nJ. The spectral width remained unchanged over the entire intensity range, and temporal broadening was negligible, reaching values no higher than 15% at 350 mW. Minor side wings in the interferometric autocorrelation trace may indicate a small nonlinear frequency chirp.

In conclusion, the hollow-core PCF described here permits fiber delivery of high-energy femtosecond pulses with unprecedented quality. Pulse propagation was nearly distortion free close to the zero-dispersion wavelength. Because pulses are guided almost exclusively in air, nonlinear effects were minimal with essentially intensity-independent propagation over the entire range investigated.

Dual-Wavelength Channel Detection. Using the hollow-core PCF for excitation light delivery to the microscope headpiece, we next evaluated the use of a large-core optical plastic fiber (OPF) for fluorescence collection and flexible fluorescent light conduction towards a stationary PMT setup (for details on detector setup see subsection 7.1.1). Originally, an individual PMT directly at the animal's head was used for 'whole-area' fluorescence detection [41]. As a result, limitations on detector type, size, weight and number had to be accepted. Employing a large-core fiber for fluorescence collection effectively alleviates these restrictions. At the same time, efficient fluorescence collection can be achieved.

Dual-color focal check beads (15 μm diameter; 'green' inside, 'red' outside; Molecular Probes) served as a test sample to evaluate dual-wavelength channel imaging capabilities through the OPF. Fig. 3.6 shows example images taken at high spatial resolution. In addition, dual-color fluorescence images were obtained in a series of in vivo experiments. In particular, dual-color fluorescence images of astroglial and neuronal networks were recorded in layer 2 of the intact rat neocortex (see Fig. 3.12). The large-core fiber detection scheme thus enables efficient and concurrent imaging of differentially labeled tissue elements in vivo.

Remote Positioning of the Field of View. Furthermore, we evaluated the use of

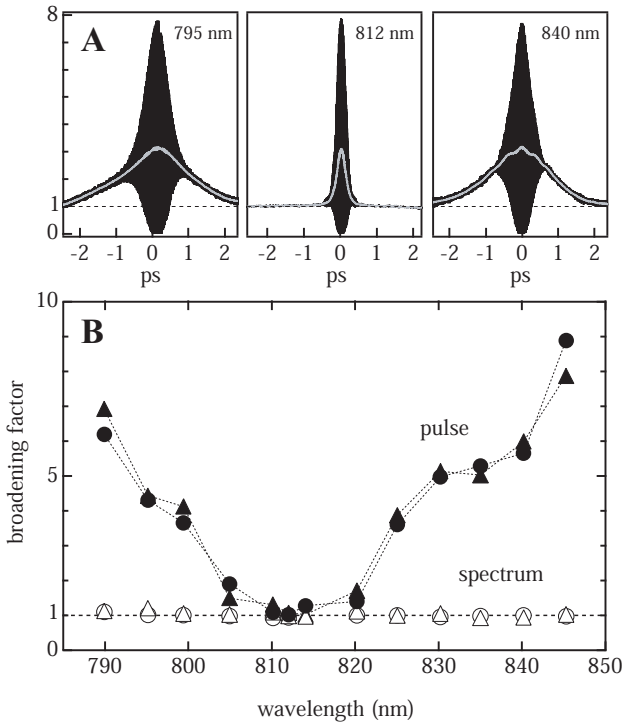

Figure 3.3: Pulse propagation through the hollow-core fiber. (**A**) Autocorrelation measurements of output pulses at three different wavelengths (250 mW average output power). The interferometric autocorrelations are shown by the black traces, and the intensity autocorrelations are shown by the light curves. (**B**) Relative broadening of pulse width (filled shapes) and spectral width (open shapes) compared with the corresponding input pulse (170 - 290 fs). The dashed line indicates 100%. The widths are plotted for average output powers of 2 mW (circles) and 250 mW (triangles). No prechirp was used.

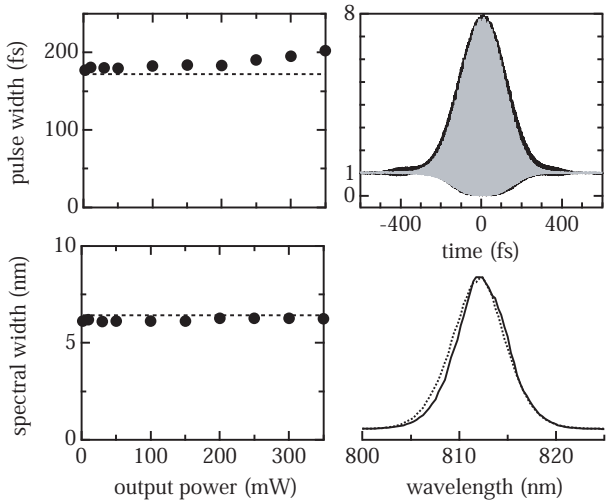

Figure 3.4: Distortion-free high-energy pulse transmission through the hollow-core fiber. Left, pulse width (top) and spectrum width (bottom) at an 812 nm center wavelength as a function of transmitted average power. The dashed lines indicate the width of the input pulse. Right, interferometric autocorrelation (top; black curve) and spectrum (bottom) for 350 mW output power. Traces are compared with the 170 fs input pulse (gray autocorrelation at the top and dashed spectrum at the bottom). No prechirp was used.

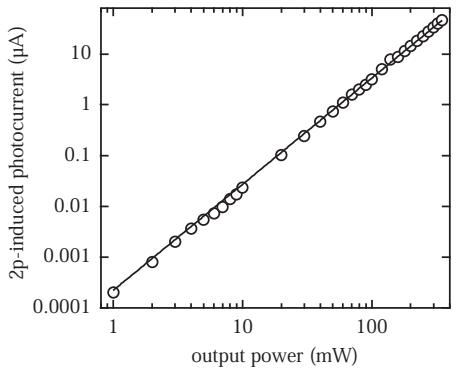

Figure 3.5: Efficient two-photon excitation through the hollow-core fiber. The two-photon-induced photocurrent in a GaAsP photodiode is plotted as a function of average output power. A quadratic relationship (fit exponent 2.09) was found over the entire range up to 350 mW. Measurements were well below photodiode saturation (400 mA).

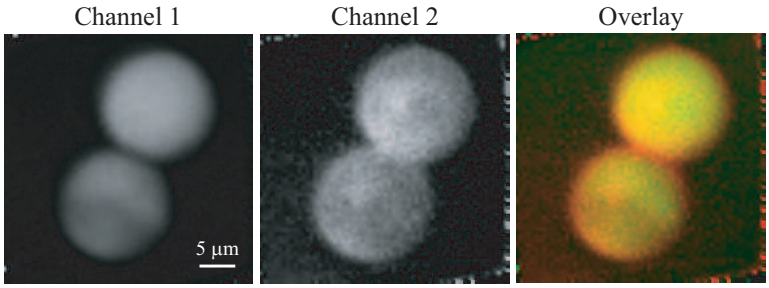

Figure 3.6: Dual-wavelength channel imaging of 15 μm focal check beads with the single-fiber based miniature microscope. Left and center, fluorescence images recorded in the 'green' and 'red' channel, respectively. Right, overlay of the green and red wavelength channel.

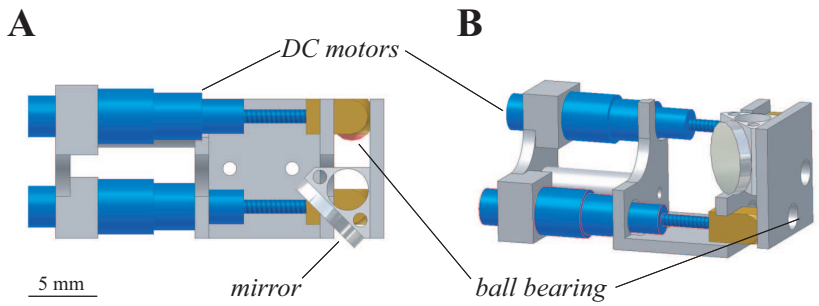

Figure 3.7: Schematic of the motor-driven mirror-mounted tilting stage (in the miniature headpiece, the fiber scanner is located in the cut-out of the motor anchorage and held by a different fitting; the fiber tip is aligned parallel to the motor axis). (**A**) Top view of the motorized mirror holder. (**B**) Side view.

a motor-driven mirror-mounted tilting stage within the head-mounted microscope for remote positioning of the FOV. During and following behaving animal movements, shifts in the relative position of the brain with respect to the skull can occur, which entail FOV shifts of typically a few tens of micrometers [79]. To enable compensation of such displacements, we designed a motorized mirror holder, which allows remote adjustment of the excitation beam angle with respect to the objective axis. The mirror holder consisted of a small wedge to which the mirror was mounted. The wedge, in turn, was attached to a tilting stage. Tilting was achieved using a pair of small DC motors (3 mm 'smoovy' gearmotor; gear ratio 1:125; RMB Miniature Bearings). Each motor had a threaded rod attached to its motor axle, which connected to a shuttle nut rigidly attached to the tilting stage. The motorized mirror holder formed a ∼45 degree angle with both the plane perpendicular to the fiber axis and the axis of the collimating lens (Fig. 3.7).

By imaging a monolayer of 1 μm fluorescent beads, we tested whether the motor-driven tilting stage provides efficient remote positioning of the FOV. Image shifts on the order of several tens of micrometers could readily be achieved in both x and y direction (Fig. 3.8A). At the mirror deflections used in our experiments, no concomitant image shift in z direction was observed. Effective FOV changes were also obtained in vivo (Fig. 3.8B). However, due to the reductionist

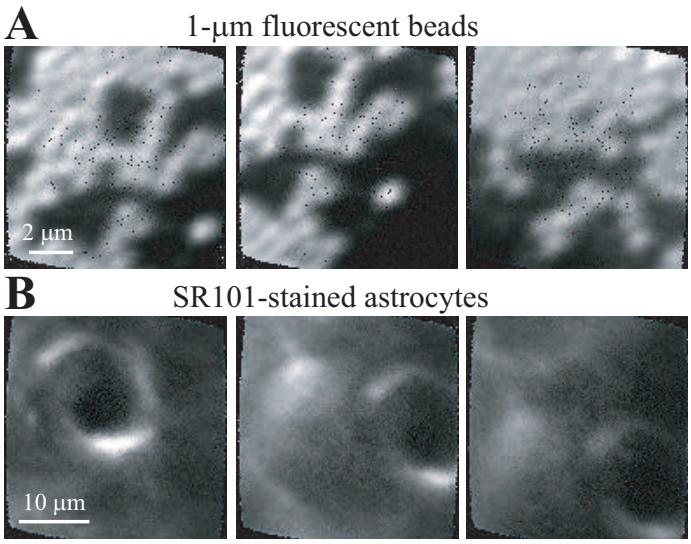

Figure 3.8: Remote positioning of the field of view. (**A**) Example images showing a monolayer of 1 μm fluorescent beads. Individual images were obtained at different mirror deflections. (**B**) Sulforhodamine 101-stained astrocytes in the intact rat neocortex. FOV changes were obtained by mirror tilting.

optical layout of the head-mounted microscope mirror deflections led to lateral shifts of the collimated beam across the objective's back aperture. As a results, beam clipping occurred at large deflection angles. Nevertheless, the motorized mirror holder is suited for remote positioning of the FOV, covering the range of image shifts being expected to (occasionally) occur in freely moving animals.

3.1.2 Coherent Fiber Bundle Based Two-Photon Microscope

As we have just seen in the previous subsection, one approach to microscope miniaturization has been the use of a single single-mode optical fiber for excitation light delivery combined with a fiber-tip scanning mechanism [79] [77]. The placement of the scanning mechanism at the fiber end, however, limits further miniaturization and makes these designs potentially sensitive to rapid accelerations. Alternatively, rigid two-photon endoscopic probes have been built with stacks of cylindrical gradient-index (GRIN) rod lenses [92] [117] [91]. These are well suited for microendoscopy but are limited in their flexibility. A possible way to overcome these limitations is the use of optical image guides that consist of several thousand cores, permitting the coherent transmission of images with preserved spatial relationships. A major advantage of such fiber bundles is that the scanning mechanism can be placed at the fiber entrance. Several confocal fiber-bundle microscopes have been presented [162] [105] [50]; however, they are limited in fluorescence detection and depth penetration. In contrast, two-photon excitation through a coherent optical image guide might allow flexible, ultrasmall microscope probes capable of deep imaging in biological tissue.

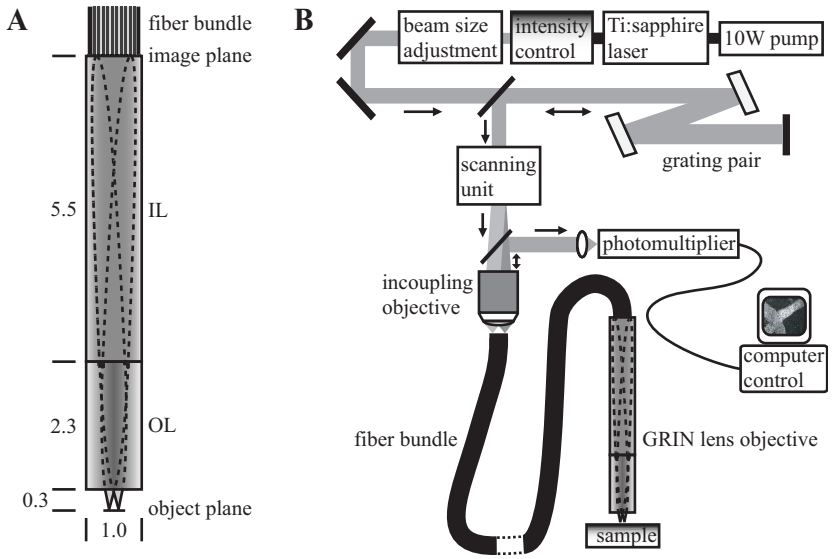

Figure 3.9: (**A**) GRIN lens objective connected to the fiber-bundle end face. Scale is in millimeters. The divergent beams emerging from the fiber cores are collimated by the imaging GRIN lens (IL) and refocused by the objective GRIN lens (OL). The optical path is exemplified for two different cores. (**B**) Scheme of the optical setup. Femtosecond laser pulses double pass a pair of diffraction gratings before they are coupled into the 1.4 m long fiber bundle through a standard two-photon laser-scanning microscope. Fluorescent light is detected through the fiber bundle and the incoupling objective by a photomultiplier tube.

As a first step towards this goal, we characterized a miniaturized two-photon microscope that consists of a fused coherent fiber bundle and an objective lens system based on a pair of GRIN lenses. A 140 cm long fused coherent fiber bundle composed of 30,000 individual cores and with a specified minimum bending radius of 4 cm was used (Sumitomo Electric Industries, IGN-08/30). The individual fiber cores had a diameter of 2.4 μm and a NA of 0.35. The distance between two neighboring cores is 4 μm. The image area (i.e. the area containing the fiber cores) had a diameter of 0.8 mm. The total outer diameter of the bundle, including a jacket for mechanical protection, was 0.95 mm. The end face of the bundle was connected to a GRIN lens objective composed of two 1 mm diameter GRIN lenses (GRINTECH), glued to each other with UV curing adhesive (Fig. 3.9A). The imaging lens, which collimates the light emerging from the single cores, had a pitch of 0.25 and a NA of 0.2. The objective lens, which refocuses the light, had a pitch of 0.20 and a NA of 0.5. Taken together, this GRIN lens pair transfers images with a 2.5 demagnification from the fiber end face to the object plane at a working distance of 300 μm. The fiber bundle was fixed under the incoupling objective of a standard two-photon microscope with a custom holder. The experimental setup is shown in Figure 3.9B.

Since the individual cores of the fiber bundle consisted of solid glass, pulse broadening due to dispersion and nonlinearities had to be corrected [79]. To precompensate the positive group-velocity dispersion that occurs in the fiber-bundle cores, laser pulses were negatively prechirped by double passing a pair of diffraction gratings in a Littrow configuration (400 grooves/mm, 9.7

blaze angle; Richardson Grating Laboratory). This approach restored the pulse width at low (<5 mW) average output powers. However, autocorrelation and spectrum measurements revealed severe nonlinear pulse broadening at higher pulse energies that was comparable with standard step-index single-mode fibers [81]. Even with dispersion compensation, two-photon excitation thus remained suboptimal at the laser intensities typically used.

Following passage through the grating pair, the laser beam was coupled to a custom laser-scanning microscope and focused through a 10× 0.25 air objective (Zeiss Achrostigmat) on the fiber-bundle entrance face. Raster scanning resulted in sequential coupling of the laser beam into individual fiber cores. The efficiency of coupling was typically ∼50%. Fluorescent light was detected through the GRIN lens objective and the fiber bundle. A beam splitter separated the infrared excitation light from the fluorescent light, which was detected by a photomultiplier tube (R6357, Hamamatsu).

To characterize the basic features of this two-photon fiber-bundle microscope we imaged fluorescent beads of different sizes (6, 3, and 1 μm diameter; Polysciences). The average output power used in these measurements was approximately 30 mW. The images of the beads appeared pixelated, revealing the hexagonal arrangement (honeycomb pattern) of the fiber cores (Fig. 3.10). A smoothed visualization of the beads was achieved by blurring the images with a Gaussian filter (pixel radius equal to the core spacing; ImageJ software). An alternative method for depixelation is to apply a bandpass-rejection filter in the Fourier domain [44]. Figure 3.10 shows line profiles through the bead images before and after blurring. The FWHM of the profiles of the smoothed images was 6.09 μm for the 6 μm beads and 3.04 μm for the 3 μm beads. Imaging of 1 μm beads resulted in a single bright core, demonstrating that the resolution of the fiber-bundle microscope is fundamentally limited by the core spacing rather than by the resolution limit of the GRIN objective. According to the sampling theorem, the highest spatial frequencies that can be resolved are given by $1/(2d)$, where d is the core spacing. Given a core spacing of 1.6 μm (physical distance between neighboring cores divided by 2.5 demagnification), the lateral resolution of the current version of the fiber-bundle microscope is 3.2 μm.

The axial resolution of the fiber-bundle microscope was measured by imaging 1 μm beads at different focal planes. The FWHM of a Gaussian fit of the integrated gray-value intensity profile as a function of z position was 20 μm. This value deviates from a theoretical value of approximately 10 μm, calculated from the NA of the objective lens. This mismatch is probably caused by aberrations of the GRIN lens system [117] [105]. We next tested the possibility of imaging extended objects with the fiber-bundle microscope. Pollen grains, a widely used fluorescent test sample, were imaged through the fiber bundle, and images were compared with images obtained with a standard two-photon microscope (Fig. 3.11). Different types of pollen grain could be easily identified. Although the fine structure of the pollen grains could not be resolved in as much detail as with a standard two-photon microscope (Fig. 3.11A), Gaussian-blurred fiber-bundle microscope images provided a low-resolution visualization of the structure of the pollen grains (Fig. 3.11C).

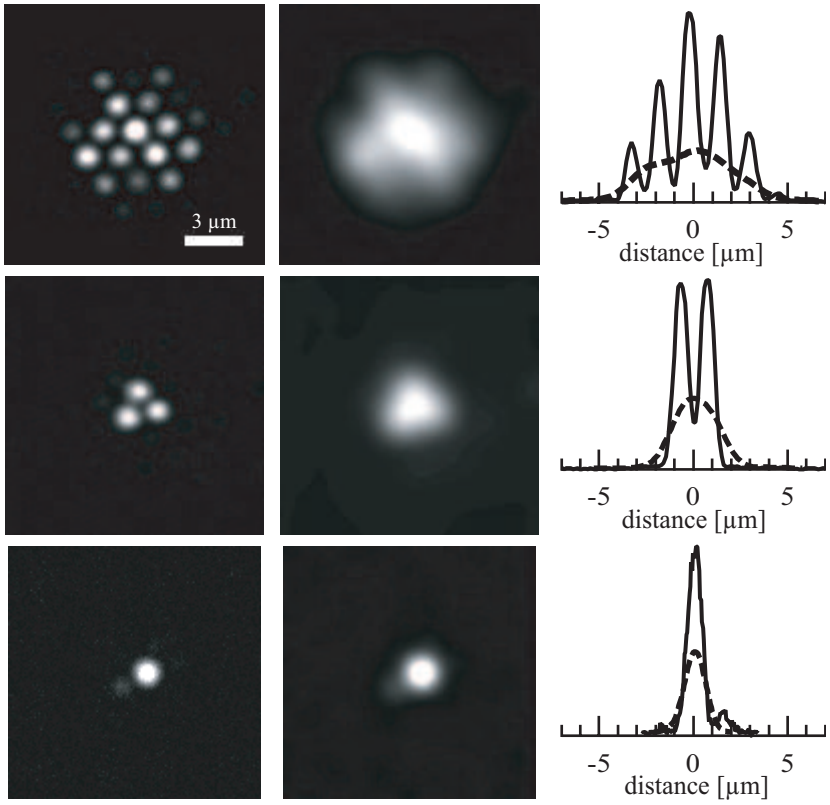

Figure 3.10: Fiber-bundle microscope images of single fluorescent beads of various sizes (top row, 6 μm diameter; middle row, 3 μm diameter; bottom row, 1 μm diameter). Left column shows raw images, in which individual fiber-bundle cores are clearly visible. Images in the middle column were blurred with a Gaussian filter. Right column shows intensity line profiles of the raw (solid traces) and the smoothed (dashed traces) images.

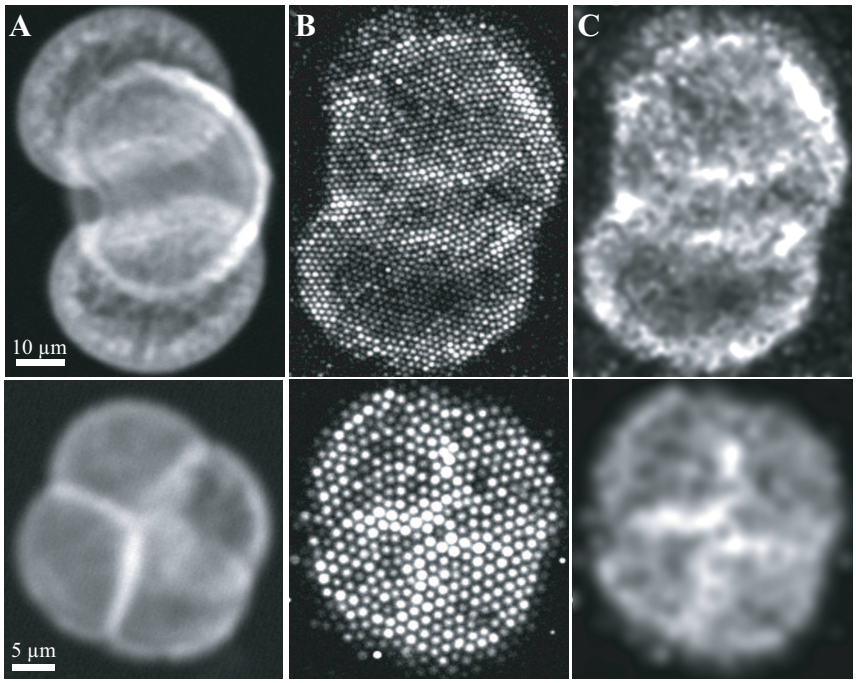

Figure 3.11: Examples of two-photon fiber-bundle microscope images of two types of pollen grain. (**A**) Images taken with a standard two-photon microscope. (**B**) Raw images of the same types of pollen grain taken with a fiber-bundle microscope (averages of 10). (**C**) Smoothed visualization of the images after application of a Gaussian blur filter.

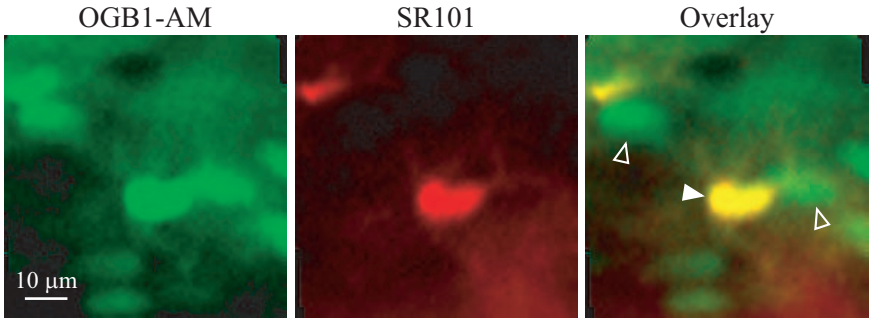

Figure 3.12: Fiber-microscope images of cellular networks in vivo. Left, OGB-1 AM labeled layer 2 cells in intact rat neocortex. Center, astrocytes counterstained using sulforhodamine 101. Right, overlay of the two fluorescence channels permitting separation of the astroglial (yellow) and neuronal (green) network. Open and closed arrowheads indicate neurons and astrocytes, respectively.

3.2 In Vivo Imaging Using Fiber-Based Two-Photon Microscopes

The development of miniaturized two-photon microscopes, as a first step, aims at obtaining high-resolution images from deep within living tissue. We therefore tested whether our two fiber-based approaches can be used for in vivo imaging in the intact brain of head-restrained anaesthetized animals.

Improved Single Fiber Based Two-Photon Microscope. We labeled astroglial and neuronal networks in vivo using multicell bolus-loading [181] with Oregon Green 488 BAPTA-1 acetoxymethyl (AM) ester (OGB-1 AM) and surface application of sulforhodamine 101 [138], respectively. High-resolution images of both astroglial and neuronal networks could be achieved down to layer 2 of the intact rat neocortex (Fig. 3.12).

Fiber-Bundle Based Two-Photon Microscope. Tail-vein injection of dextran-conjugated Fluorescein or Rhodamine (5% weight per volume in normal rat Ringer solution) was used to fluorescently label the blood plasma of anesthetized rats, and to test the use of the fiber-bundle microscope for in vivo imaging. Stained blood vessels were imaged through a 3 mm $\times$ 3 mm craniotomy above the somatosensory area of the neocortex by lowering the GRIN lens objective down to the exposed brain surface. Individual medium- and small-caliber vessels could be resolved near the brain surface (Fig. 3.13).

This demonstrates, that our miniature two-photon microscopes in combination with fluorescent staining techniques are capable of obtaining high-resolution images in vivo up to cortical layer 2.

Meaningful application to biological questions, however, requires appropriate fluorescence staining techniques that visualize biological structure and function. Such techniques

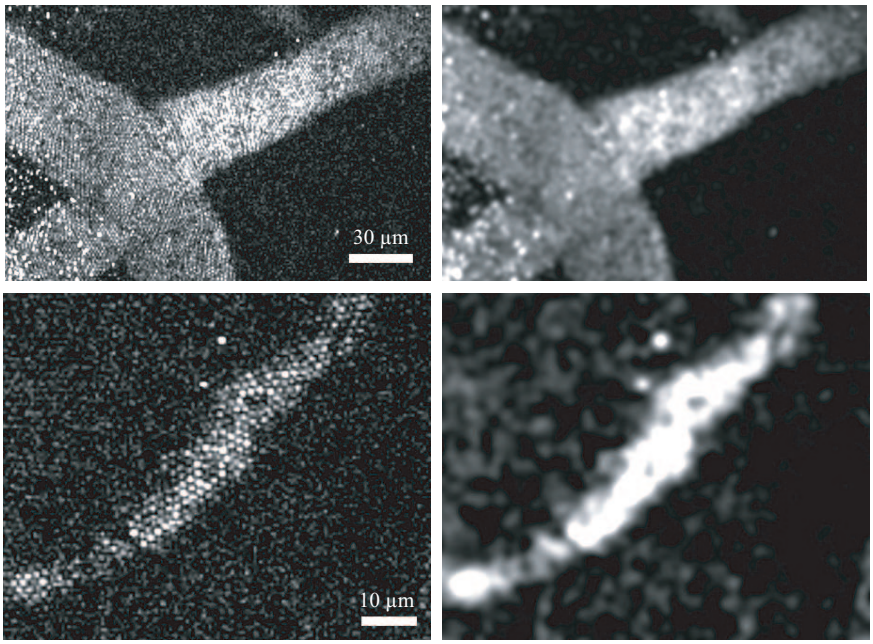

Figure 3.13: Fiber-bundle microscope images of Fluorescein-labeled brain microvasculature in intact neocortex of a living, anesthetized rat. Raw images (left) and smoothed images (right) are shown. The junction of two large blood vessels is visible in the upper row (average of 20). A small-caliber blood vessel is shown in the lower row (average of 10).

had been lacking at the start of this thesis. Thus, in parallel to microscope miniaturization we developed novel fluorescence staining techniques capable to report structure and/or function of specific cell populations in vivo. Note, that a combination of two of these novel labeling techniques has been employed to obtain the images presented in Fig. 3.12.

3.3 Fluorescence Labeling of Neocortical Cell Populations In Vivo

Every fluorescence labeling technique comprises two essential components, the delivery method and the fluorescent indicator itself. Some general requirements concerning fluorescent tissue labeling have been discussed in section 2.3. Here, we were interested in staining techniques for cell-type specific labeling of cellular populations in vivo. We present labeling techniques for three of the four major cellular components in the brain. In particular, subsection 3.3.1 describes two virus-based systems for fluorescent indicator expression in defined neuronal subpopulations (several dozens to hundreds of pyramidal cells). Subsection 3.3.2 presents a method for rapid and specific staining of neocortical astrocytes through simple fluorescent indicator uptake, while subsection 3.3.3 describes a transgenic approach for specific staining of resident microglial cells in vivo. Applications to these staining techniques are presented in section 3.4. Note, that both the evaluation

and application of novel staining techniques presented in the following sections was performed using a conventional 2PM.

3.3.1 Neurons

We have developed a technique for targeted expression of anatomical and functional indicators in a defined subset of neurons in the intact cortex. Labeling is based on stereotactic delivery of engineered Sindbis- or Lentiviral particles for rapid short- and stable long-term expression of fluorescent indicators, respectively. We applied this technique to study the structural plasticity of neurons on the synaptic level (see subsection 3.4.1.1), and to evaluate the use of genetically encoded calcium indicators (GECIs) for imaging of neuronal activity in vivo (see subsection 3.4.1.2).

Short-Term Expression of Fluorescent Proteins. For short-term expression of fluorescent proteins in cortical neurons, we used a viral vector, SINrep(nsP2S^{726}), with attenuated cytotoxicity. For details of virus production, a careful investigation of specificity and virus-associated cytotoxicity see [102].

To demonstrate the use of the SINrep(nsP2S^{726})/EGFP vector for in vivo imaging, we stereotaxically injected viral particles to the layer 2/3 somatosensory cortex of 3-week-old rats. As shown in Fig. 3.14A, after a 24 - 36 h expression period this procedure resulted in bright and temporally stable labeling of a small population of cortical pyramidal cells. The high level of EGFP expression was especially useful for high-resolution time-lapse imaging of dendritic spines. No signs of photobleaching were observed even after 1 h of continuous image acquisition (Fig. 3.14B and C; subsection 7.2.1). Thus, the modified Sindbis virus expression system is well suited for studies in which rapid heterologous protein expression is of advantage, for example, for in vivo imaging of fine dendritic spine morphology.

Furthermore, we have constructed a SINrep(nsP2S^{726})-based vector containing two subgenomic promoters, SINrep(nsP2S^{726})2SP (a similar construct was previously described for SINrep5 vector [144]). This vector can be used to express independently EGFP (to outline dendritic morphology) and a second protein (such as a neuronal protein or its dominant negative form). This approach was employed to probe the potential role of a specific molecular mechanism in dendritic structural plasticity (see subsection 3.4.1.1).

Long-Term Expression of Fluorescent Proteins. Due to the delayed cytotoxic effects on infected cells, the modified Sindbis virus system is not eligible for long-term investigations (several days to weeks). In contrast, Lentiviral vectors permit stable protein expression in cortical cells without compromising cell viability or function (for details on virus production and in vitro assessment see [48]). The rate of protein expression in Lentivirus infected cells, however, is considerably lower and therefore the lag phase somewhat longer compared to Sindbis virus infected cells.

We tested whether EGFP expression from two Lentivirus vectors, FCK(1.3)GW- and FSy(1.1)GW, employing a mouse α-CaMKII (size: 1.3 kb) and a rat Synapsin I promoter (size: 1.1 kb), respectively, is sufficient for in vivo two-photon imaging at the resolution of

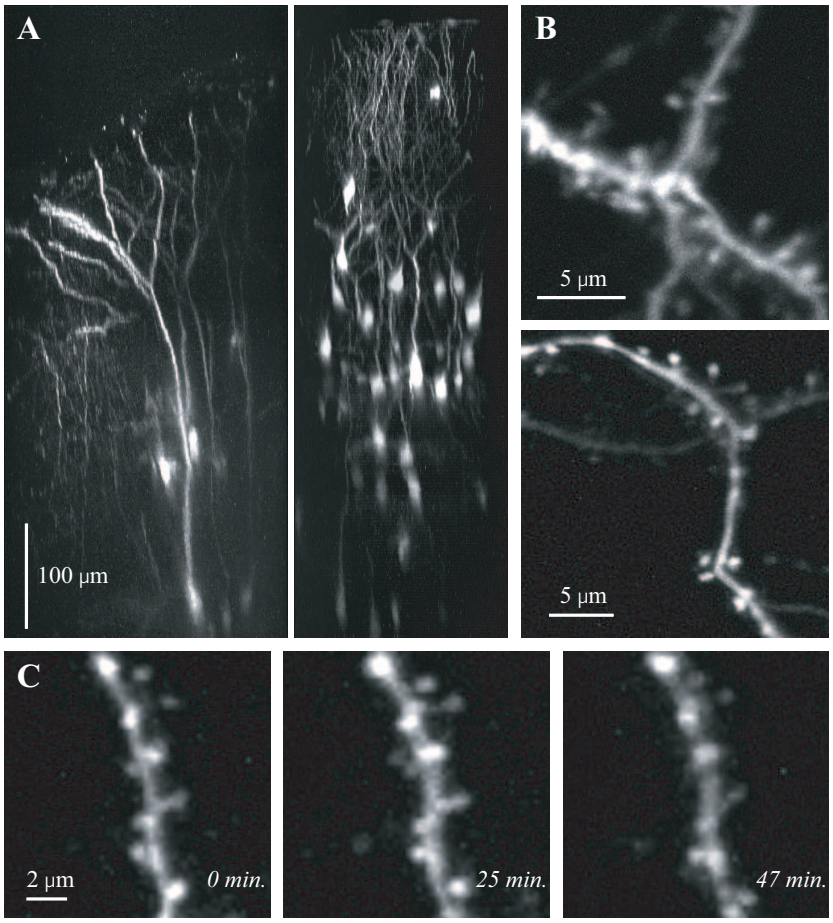

Figure 3.14: In vivo 2-photon imaging of Sindbis virus infected EGFP-expressing cortical neurons after 1 day expression. (**A**) Two example overview maximum-intensity side-projections of infected areas showing EGFP-expression primarily in layer 2/3 principal neurons. (**B**) Examples of high magnification images of spiny dendritic branches. (**C**) Example of a time-lapse recording of dendritic spines over a period of 47 min. Images are projections of stacks of 20 images (z-step, 1 μm). Stacks were acquired at 45 s interval.

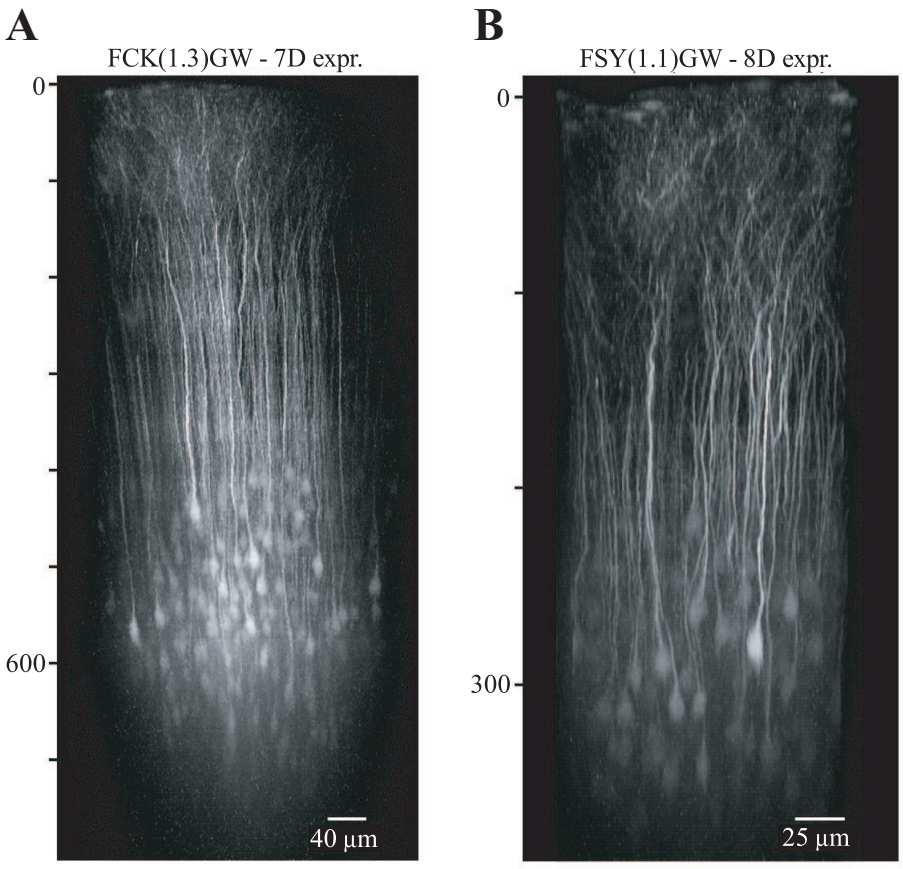

Figure 3.15: In vivo expression pattern of cortical layer 2/3 Lentivirus-infected neurons. Each image is a maximum-intensity side projection from an overview stack of fluorescence images recorded by using in vivo two-photon microscopy. Note the different depth scaling (indicated on the left of each image) and the different scale bars. (**A**) FCK(1.3)GW-infected neurons in a P28 rat after 7 days of expression. (**B**) FSy(1.1)GW-infected neurons in a P48 mouse after 8 days of expression.

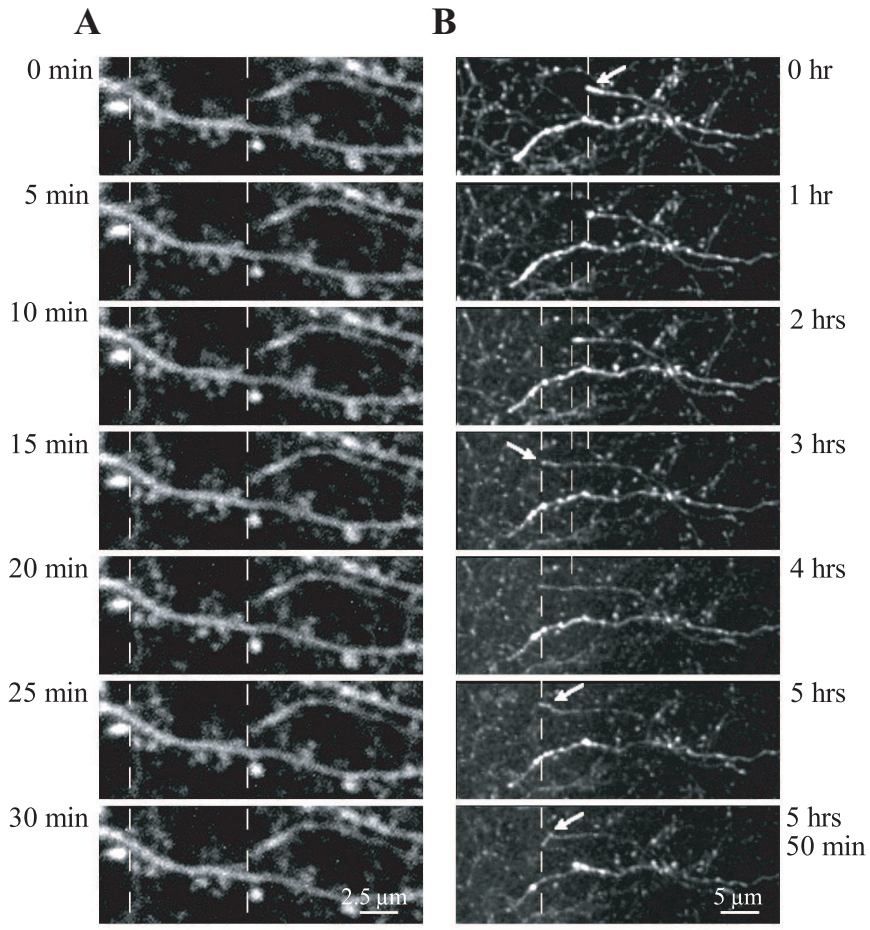

Figure 3.16: Two-photon time-lapse imaging of dendritic spines and axonal projections in the mouse cortex. Acquisition times are indicated on the sides of each image. Each image is a maximum-intensity projection of image stacks (z step, 1 μm) collected in cortical layer 1 in vivo (Lentivirus-infected neurons were located in layer 2/3). Dashed vertical lines serve as a guide for comparison of structures over time. (**A**) Imaging of dendritic spines caused no photobleaching after 30 min at a 1 min sampling interval, with $\Delta F(t = 30 \text{ min}) \simeq 0.97 \cdot \Delta F(t = 0 \text{ min})$. (**B**) Imaging of axons in a layer 1 region adjacent to the injection site for >5 h at a 5 min sampling interval, with $\Delta F(t = 5 \text{ h}) \simeq 0.66 \cdot \Delta F(t = 0 \text{ h})$. Some axonal projection endings, an example indicated by an arrow, showed directed outgrowth for several micrometers on a time scale of several hours in young animals (P15 - P17 mice). Note the different scale bars in A and B.

dendritic spines and axonal branches. After 7 days of expression, both FCK(1.3)GW- and FSy(1.1)GW-infected pyramidal neurons could be imaged routinely down to a depth of 500 μm below the pial surface and down to 800 μm under favorable conditions (e.g., removed dura, and lack of large blood vessels in the field of view) (Fig. 3.15 and Suppl. Movie SN1). High-resolution time-lapse imaging of dendritic spines in cortical layer 1 of P31 - P48 mice, after 7 - 8 days of EGFP expression, showed negligible amounts of photobleaching (Fig. 3.16A, and Suppl. Movie SN2; $\sim$97.5% of fluorescence intensity remained after 30 min imaging at a 1 min sampling interval). Similarly, EGFP-labeled axons in layer 1 region adjacent to the injection site could be imaged for extended time, >1 h when sampled at 45 s intervals, or up to 6 h at 5 min intervals (Fig. 3.16B, and Suppl. Movie SN3; $\sim$66% of fluorescence intensity remained after 5 h of imaging of stable structures at a 5 min sampling interval, in P15 - P17 mice after 5 - 6 days of expression; note the clear outgrowth of an axonal fiber ending in the time-lapse movie). Infected cells remained morphologically intact across the observation period (up to six weeks after infection; a more detailed examination of intrinsic biophysical properties of infected neurons following long-term expression is given in [48]). The Lentivirus expression system is thus well suited for stable long-term expression of FPs in small neuronal networks in the intact neocortex. Both pre- and postsynaptic elements (axons and dendrites, respectively) could be imaged in vivo and over time periods relevant to the study of synaptic plasticity (i.e. minutes to hours, and days to weeks).

In addition, the self-inactivating lentiviral vector was adapted for siRNA-based gene silencing (RNA interference is a method for gene silencing through expression of double-stranded siRNAs [54]). Several studies have reported successful gene silencing with similar retroviral vectors in neurons [208] [86] [199] [160]. Our experiments show (see Dittgen et al. [48] for more details), that siRNA driven from the U6 promoter in lentiviral vectors can cause a significant knockdown of gene expression in neurons, and, in combination with expression of EGFP, can be used to study gene functions in single neurons in vivo by two-photon imaging or two-photon targeted patching (TPTP).

3.3.2 Astrocytes

Furthermore, we discovered a new and robust method for fluorescently labeling astroglia in vivo by briefly exposing the neocortical surface to the red fluorescent dye sulforhodamine 101 (SR101). We provide several lines of evidence that SR101 is specifically taken up by protoplasmic astrocytes. Using in vivo two-photon microscopy, we visualized the distribution of astrocytes in the neocortex down to a depth of 700 μm. In addition, by combining SR101 labeling with bulk calcium indicator loading, we were able to simultaneously measure calcium dynamics in both astroglial and neuronal networks (see subsection 3.4.2.2).

Brief exposure of the neocortex of anesthetized rats and mice to the red fluorescent dye SR101 resulted in rapid staining of a subpopulation of neocortical cells (Fig. 3.17). Using in vivo two-photon microscopy, SR101-labeled cells were imaged down to 700 μm below

	Overlap, %	Non-Overlap, %	Total cells
S-100β	95.1 ± 1.1	3.4 ± 1.1	520 ($n = 4$ animals)
Anti-CNPase	2.6	97.4 ± 2.6	565 ($n = 4$ animals)
Anti-NeuN	0	100	554 ($n = 3$ animals)

Table 3.1: Quantitative comparison between the Texas Red-hydrazide (SR101-fixable analog) and the counter-immunostains in vitro (mean ± SEM)

the pial surface, revealing a relatively homogenous, non-layered distribution (Fig. 3.17B and Suppl. Movie SA1). Only a fraction of cells took up SR101, as indicated by the many unstained cell bodies found particularly in layer 2 and deeper (Fig. 3.17A). All SR101-labeled cells had similar morphological features with multiple processes originating from the cell body, often forming end feet-like structures attached to (unstained) blood vessels. Thus, their morphology closely resembled that of protoplasmic astrocytes as described for neocortex [153].

We typically obtained bright SR101 labeling using micromolar concentrations and extracellular application for several minutes. However, concentrations as low as 250 nM, and dye exposure times as short as a few seconds, were sufficient. SR101 labeling was stable for several hours, with only a slow decay in fluorescence intensity. Over this time course a more granular staining pattern developed, indicating sequestration of SR101 into intracellular organelles. To measure the time course of SR101 uptake, we applied SR101 intracortically through brief (3 s) pressure ejection from a micropipette (borosilicate glass, 2.0 mm outer diameter; 4 - 7 MΩ tip resistance). Close to the pipette tip, several cells were gradually stained within a few minutes and reached stable fluorescence levels after about 10 min (Fig. 3.17C). Notably, 60 min after local application, labeled cells showing comparable levels of fluorescence could be found in the entire cranial window (1 - 2 mm in diameter). This suggests that the spread of dye is supported by gap-junctional connections between SR101-labeled cells. Indeed, local application of the gap-junction blocker carbenoxolone (CBX, 100 μM; Sigma-Aldrich) markedly suppressed labeling of topically applied SR101 near the application pipette in a concentration-dependent manner (Fig. 3.18). Furthermore, CBX applied topically, as part of the objective immersion medium, delayed the spread of locally applied SR101 (data not shown).

The specificity of SR101-labeling for astrocytes was verified using immunohistochemistry. Because SR101 tends to leak out of cells in fixed tissue [52], we used the paraformaldehyde-fixable analog Texas Red-hydrazide, which resulted in a staining pattern similar to that from SR101. After in vivo staining with Texas Red-hydrazide, vibratome sections of labeled tissue were counter-immunostained for the calcium-binding protein S-100β, a specific marker of astrocytes [124]. Nearly all SR101-analog stained cells were found to be S-100β positive (Fig. 3.19A; Table 3.1; 95.1 ± 1.1%; $n = 520$ total cells, 4 animals; 0.4% of S-100β-positive cells presumably were SR101 negative).

By counter-immunostaining for the enzyme CNPase, which is specifically expressed in oligodendrocytes in the CNS, we also tested whether oligodendrocytes might take up SR101 (Fig. 3.19B). Nearly all CNPase-positive cells were SR101 negative, with only very few exceptions (15 of 565 total cells, in 4 animals, showed some overlap). Finally, counter-

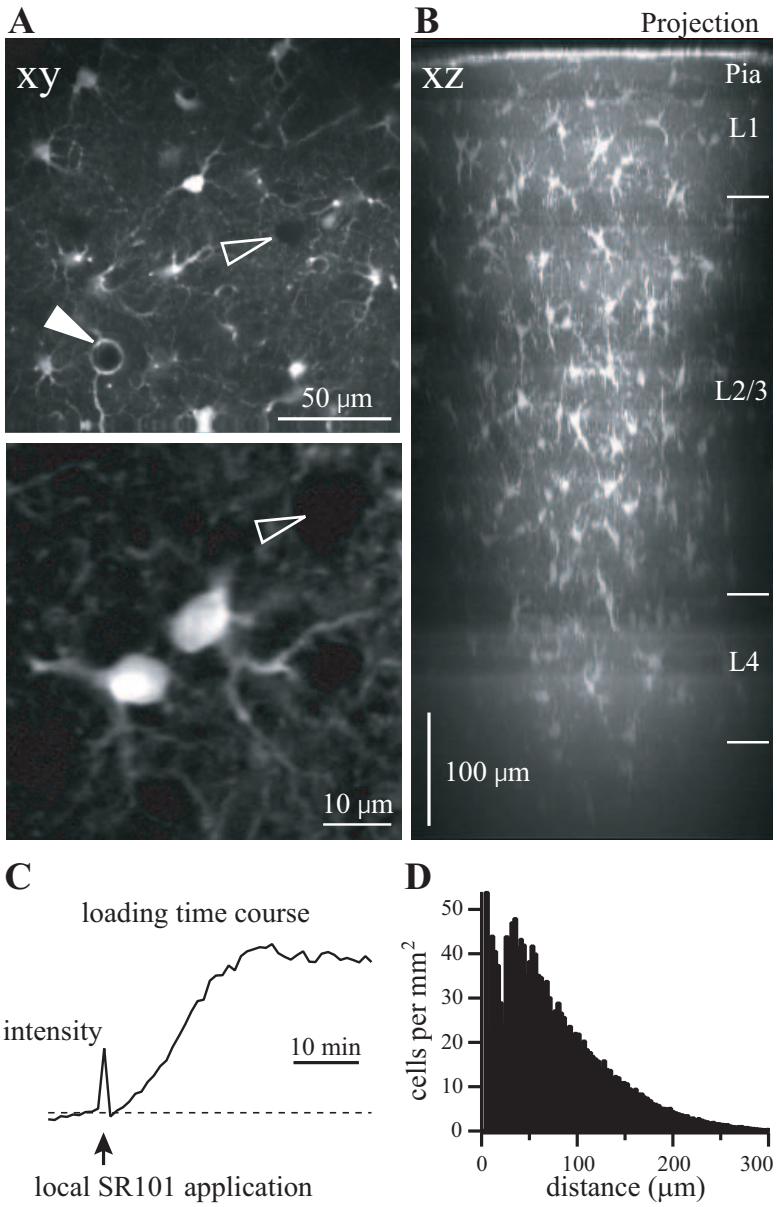

Figure 3.17: In vivo staining pattern of neocortical cells after application of SR101. (**A**) Two-photon fluorescence images (individual focal planes). Top, overview recorded about 200 μm below the pial surface, showing that a subpopulation of cells had taken up the dye. Blood vessels (solid arrowhead) and unstained cell bodies (open arrowhead) appeared as dark gaps. Bottom, high-magnification image of a labeled cell pair. (**B**) Overview side projection of an SR101-stained area in mouse neocortex 30 min after dye application. The image is a maximum-intensity side-projection from a stack of fluorescence images. (**C**) Time course of dye loading after brief intracortical dye ejection (3 s pressure pulse, 0.7 bar; 250 nM SR101 in extracellular saline). Fluorescence intensity was averaged for three cells that appeared next to the application pipette. (**D**) Radial density distribution of astrocytes in the intact mouse brain. Note sharp peak at a mean cell-to-cell distance of 15 μm, which corresponds to frequently observed pairs of astrocytes in very close proximity.

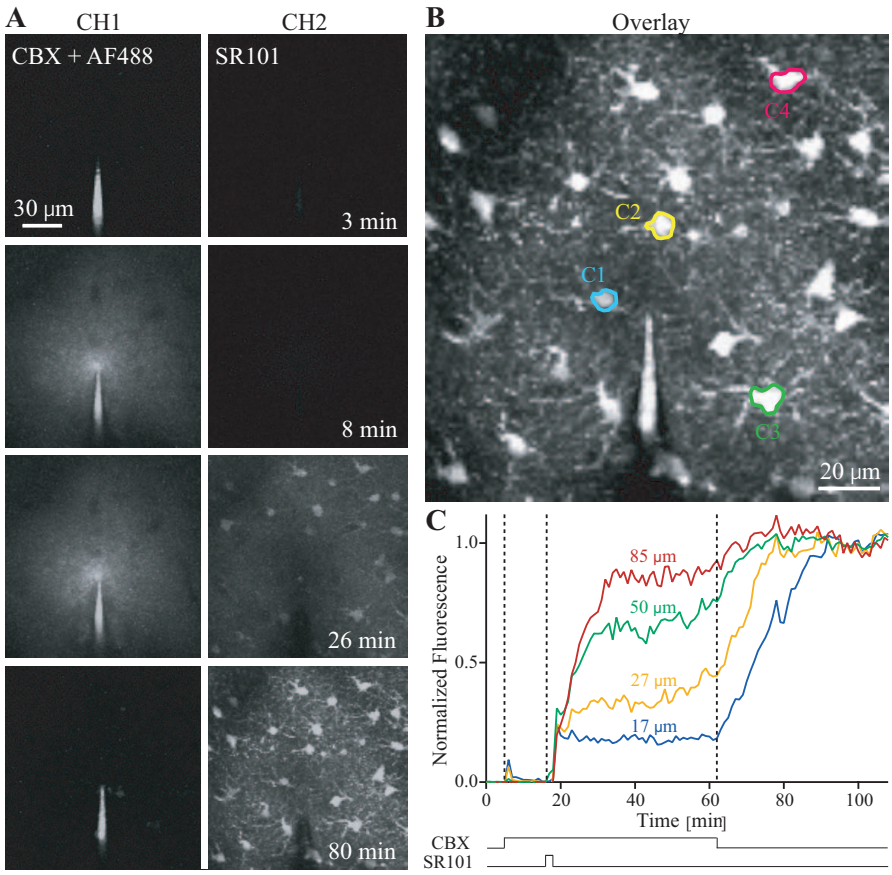

Figure 3.18: Gap junctions permit rapid spread of SR101. The gap-junction blocker carbenoxolone (CBX; 100 μM) was applied through a micropipette 85 μm below the pial surface. The pipette solution also contained the green fluorescent dye Alexa Fluor 488 (AF488; 100 μM) as a means to visualize the pipette shank and CBX ejection. During CBX application, SR101 was briefly applied to the cortical surface, which was then rinsed twice. At 45 min after SR101 application, CBX pressure ejection was ceased. (**A**) Sample images from the dual-channel in vivo time-lapse recording (taken at 60 s intervals). Images in left and right columns show the CBX-containing micropipette detected in the green channel (CH1) and the fluorescence detected in the red channel (CH2), respectively. Acquisition times are indicated for each row. Each image is a maximum-intensity projection of a 132 $\times$ 132 $\times$ 48 μm^3 fluorescence image stack (3 μm axial spacing). (**B**) Overlay of red and green fluorescence channel images indicating the micropipette tip position in two dimensions relative to surrounding cells. (**C**) Time course of fluorescence intensities in the regions of interest indicated in B. Intensities were normalized to their final values. Numbers above the curves indicate the radial distances of each cell from the micropipette tip in three dimensions. Periods of local CBX and topical SR101 application are indicated in lower traces.

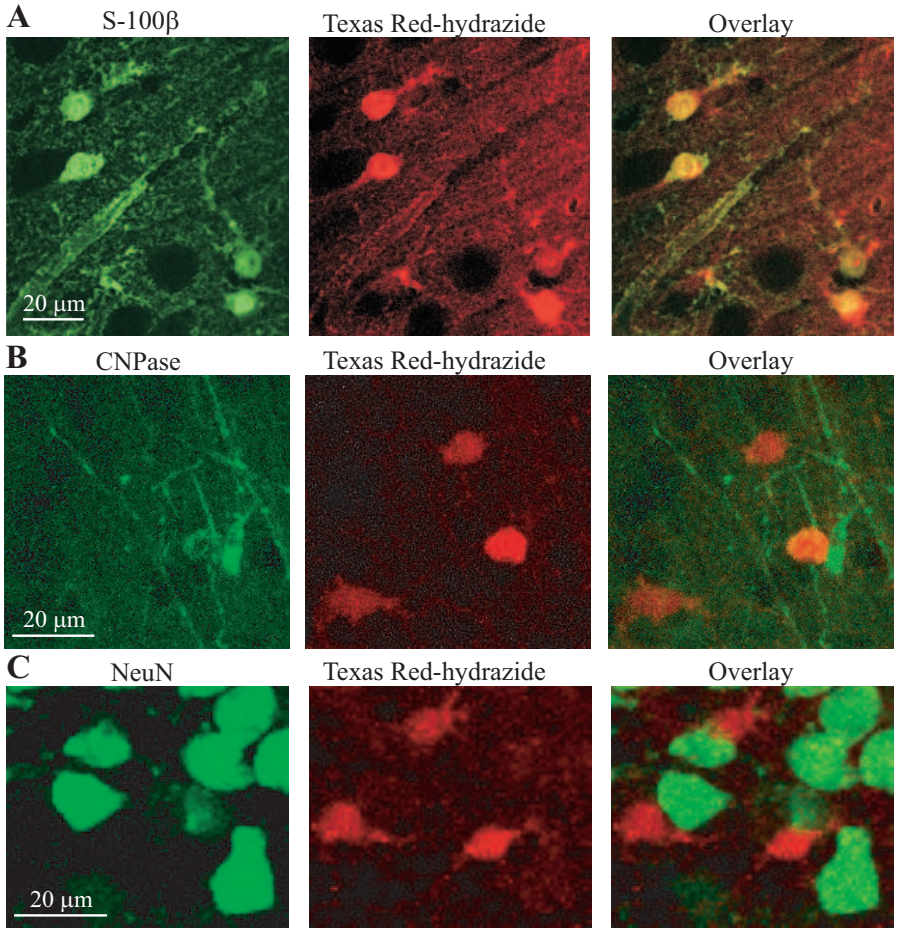

Figure 3.19: SR101-labeled cells are immunopositive for S-100β protein, but not for either the neuron-specific nuclear protein NeuN or, in the vast majority of cases, the enzyme CNPase in vitro. (**A**) Left, Pacific Blue fluorescence of anti-S-100β-labeled astrocytes in the green detection channel. Center, red fluorescence of cells stained with Texas Red-hydrazide, a paraformaldehyde-fixable analog of SR101. Right, overlay of green and red fluorescence channels. (**B**) Left, Pacific Blue fluorescence of an oligodendrocyte labeled with anti-CNPase. Center, red fluorescence of cells stained with Texas Red-hydrazide. Right, overlay of the green and red fluorescence channels. (**C**) Left, FITC fluorescence of neurons labeled with anti-NeuN in the green detection channel. Center, cells stained with Texas Red-hydrazide. Right, overlay of the fluorescence images.

	Overlap, %	Non-Overlap, %	Total cells
TgN(GFAP-EGFP) mice	97.2 ± 1.9	1.6	1064 (n = 5 animals)
CX_3CR1 mice	0.5	99.5	638 (n = 3 animals)

Table 3.2: Quantitative comparison between SR101-labeled and EGFP-expressing cells in the transgenic mice in vivo (mean ± SEM)

immunostaining for the neuron-specific nuclear protein NeuN showed no overlap between the two cell populations (Fig. 3.19C; zero overlap; n = 554 total cells; 3 animals). These results indicate that SR101 is selectively taken up by protoplasmic astrocytes when applied in vivo.

We further confirmed the astroglial specificity of SR101 uptake in experiments using transgenic mice that express EGFP in either astrocytes or microglia. We first applied SR101 to the cortex of transgenic mice (TgN(GFAP-EGFP)) in which the human glial fibrillary acidic protein (hGFAP) promoter controls EGFP expression. Only a fraction of neocortical astrocytes express EGFP in these mice [139]. In five animals tested, nearly all EGFP-expressing astrocytes (97.2 ± 1.9%; n = 1,064 total cells) were colabeled by SR101 (Fig. 3.20A, upper row; Suppl. Movie SA2 and Table 3.2). The few exceptions (17 of 1,064 total cells) were weakly EGFP-expressing cells. These cells most likely represent a subpopulation of astrocytes [124] [67] that previously have also been described as glial progenitor cells [47], and that are immunopositive for proteoglycan NG2 [67] and are not coupled by gap junctions [204]. In addition to the nearly complete overlap with EGFP-expressing cells, SR101 labeled many more cells showing similar morphology (Fig. 3.20A, upper row). In total, about half of the SR101-labeled cells were EGFP positive (52 ± 3%; n = 2,034 total cells; 5 animals). The EGFP-negative cells presumably represent the fraction of cortical astrocytes in which the GFAP-EGFP transgene was not active.

To examine whether microglial cells take up SR101, we took advantage of another genetically modified mouse line, in which the EGFP reporter gene is inserted into the *Cx3cr1* locus, encoding the chemokine receptor CX_3CR1 (also known as the fractalkine receptor) [93]. This genetic modification causes specific EGFP expression in resident microglial cells as well as macrophages. Microglial cells had anatomical features distinct from those of protoplasmic astrocytes, showing small rod-shaped somata from which numerous thin processes extended symmetrically [207]. Microglial cells and astrocytes could therefore be readily distinguished by their morphology. Consistent with this notion, we found that SR101 is not taken up by microglial cells, as indicated by lack of overlap between EGFP-expressing microglia and SR101-labeled astrocytes (Fig. 3.20A, lower row; Suppl. Movie SA3). The few exceptions found in the CX_3CR1-EGFP mice (3 of 638 total cells; 3 animals) appeared to be resident macrophages.

Based on immunohistochemistry and comparison of staining patterns in transgenic mice, we conclude that SR101 is specifically taken up by protoplasmic astrocytes in the neocortex of both rats and mice.

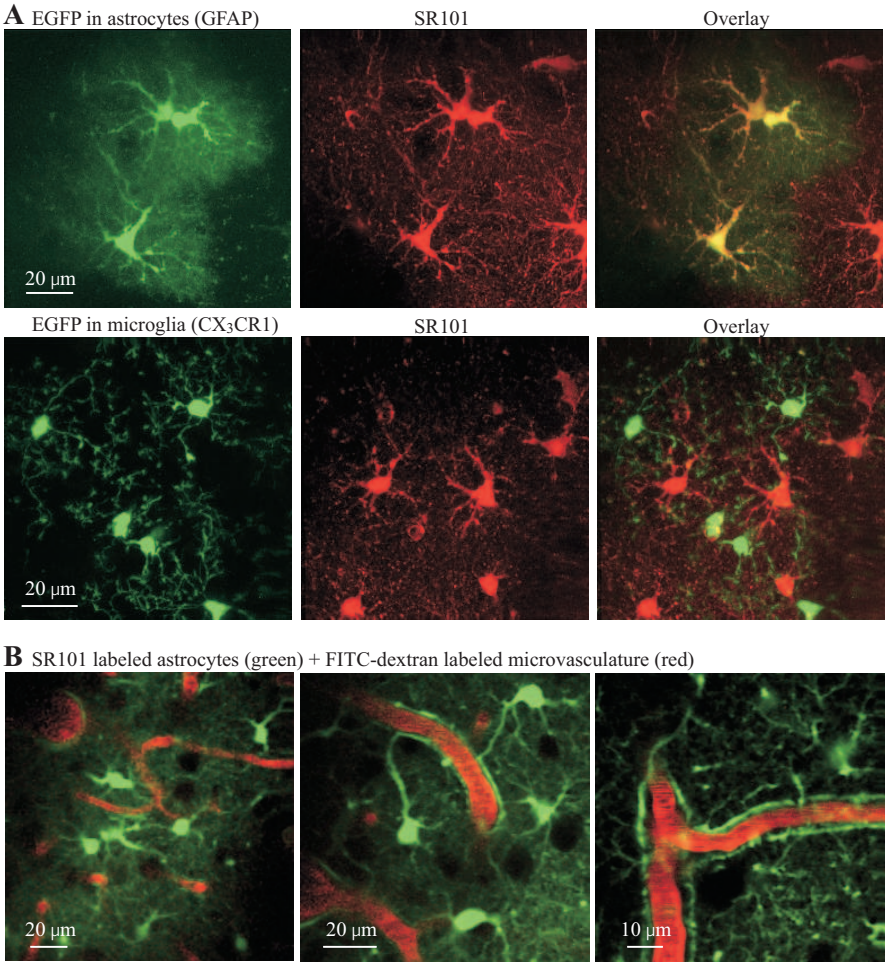

Figure 3.20: In vivo co-labeling in the neocortex using SR101. (**A**) SR101 labels astrocytes but not microglial cells in transgenic mice in vivo. Upper row: Left, astrocytes expressing EGFP under control of human GFAP promoter in a transgenic mouse line. Center, labeled cells in the same region after surface application of the red fluorescent dye SR101. Right, overlay of the green and red channel. Note that not all SR101-labeled astrocytes show green fluorescence, as the GFAP-EGFP transgene is not active in all cortical astrocytes. Lower row: Left, EGFP-expressing microglial cells in mutant mice. Center, red fluorescent cells in the same region after surface application of SR101. Right, overlay of the green and red channel. (**B**) SR101 can be used to visualize astrocytic processes such as those found at the gliovascular interface. Example images showing costaining of neocortical astroglia and microvasculature in vivo. Blood plasma was stained by tail-vein injection of FITC-labeled dextran. Note that green and red pseudocolor lookup tables were assigned to fluorescence images of SR101 labeled astrocytes and fluorescent labeled blood plasma, respectively.

3.3.3 Microglia

The CX_3CR1-EGFP mice were also used to investigate microglia behavior in the adult brain (see subsection 3.4.3). As mentioned earlier, these genetically modified mice were generated by replacing the open reading frame of the CX_3CR1 gene (fractalkine receptor) with the EGFP gene using homologous recombination [93]. In the cortex, this results in specific EGFP expression in microglia. For the study of microglial motility, heterozygous mice were used following interbreeding with C57BL6 wildtype mice. Heterozygous mice, carrying only one wildtype allel of the *Cx3cr1* locus beside the mutant EGFP-containing allel, did not show obvious abnormalities suggesting a similar level of CX_3CR1 expression.

3.4 Dynamic Processes in Neocortical Cell Populations In Vivo

We applied the above-mentioned fluorescence labeling techniques to study the structural dynamics of neurons, astrocytes and microglia in the intact adult brain. The corresponding results are presented in subsections 3.4.1.1, 3.4.2.1, and 3.4.3, respectively. Furthermore, we aimed to visualize the spatiotemporal activity patterns of the different cellular populations in vivo. In particular, we evaluated the use of virus-driven expression of genetically encoded calcium indicators (GECIs) for the purpose of visualizing neuronal activity (see subsection 3.4.1.2). Bolus loading of synthetic calcium indicators in conjunction with SR101 application was used to simultaneously monitor neuronal and astroglial signaling in vivo (see subsection 3.4.2.2). Functional labeling of microglial cells was not achieved.

3.4.1 Neurons

3.4.1.1 Structural Dynamics

Dendritic spines of principal neurons are the major targets of excitatory synapses in the brain [166]. They are unique functional compartments containing a variety of post-synaptic components. These include a varying number of glutamate receptors, anchoring cytoskeletal proteins (directly or indirectly linked to the receptors' intracellular C-terminal domains), signaling molecules and filamentous actin (F-actin), which provides an overall structural support for spines. Dendritic spines have been proposed as the locus of long-term synaptic plasticity, which is believed to be the primary molecular mechanism by which neuronal networks encode and store information. In addition, accumulating evidence indicates that changes in dendritic structural stability occur in response to synaptic activity in young as well as adult brain (reviewed in [174] [21]). Several studies reported, for example, the appearance of new filopodia (i.e. protuberances which may or may not form synaptic contacts) or spines and/or structural reorganization of synaptic contacts in response to induction of long-term potentiation (LTP) in hippocampal CA1 neurons in

vitro [55] [121] [189] [59]. Furthermore, deprivation of sensory inputs to the barrel cortex of one to two week-old rats in vivo, which induces downregulation of synaptic transmission between layer 4 to layer 2/3 projections [7], was shown to decrease rapid filopodial motility of layer 2/3 neurons [116]. These findings imply that the onset of synaptic plasticity, as manifested by changes in the efficacy of synaptic transmission, is followed by changes in structural organization of synaptic contacts.

What then might be the mechanisms that link synaptic plasticity to structural reorganization of synaptic contacts? Activation of NMDA-type glutamate receptors is a shared requirement for both the induction of LTP and structural changes, which occur typically with a delay of 30 min to 2 hours [55] [121] [189]. Such a temporal shift coincides well with transcriptional activation of immediate early genes (IEGs), suggesting that some of the neuronal IEGs known to be induced by synaptic activity may participate in structural plasticity of dendritic spines (reviewed in [111]).

The neurospecific IEG Homer1a was shown to be induced in vivo by seizures, LTP and exploratory behavior [24] [97] [201]. Here, we tested whether Homer1a might be involved in dendritic structural plasticity. We report that rapid overexpression of recombinant Myc-tagged Homer1a (^{Myc}Homer1a) in cortical layer 2/3 principal neurons results in the appearance of highly motile filopodia on distal dendritic branches in vivo. The steady state filopodia/spine density in ^{Myc}Homer1a expressing neurons, however, was not significantly increased compared to control conditions. Our results indicate that activity-driven expression of Homer1a might be involved in providing a possible molecular link between induction of synaptic plasticity and structural changes at the level of dendritic spines.

To address the question whether the IEG Homer1a might be involved in dendritic spine plasticity, we used the attenuated Sindbis vector [102] [49] containing two subgenomic promoters, termed SINrep(nsP2S^{726})2SP. This vector allowed us to simultaneously express ^{Myc}Homer1a and EGFP in the same cell (EGFP expression is used to outline the morphology of infected cells for two-photon imaging). Furthermore, due to its strong heterologous protein expression with a rapid onset after infection it is well suited for studying the function of IEGs as the SINrep(nsP2S^{726})2SP-driven expression approximately resembles the dynamics of IEG induction. As a control, we used a SINrep(nsP2S^{726})2SP vector expressing only EGFP and a defective ^{Myc}Homer1a variant, termed ^{Myc}Homer1a(W24A)+EGFP.

The SINrep(nsP2S^{726})2SP^{Myc}Homer1a+EGFP, SINrep(nsP2S^{726})2SP-EGFP or SINrep(nsP2S^{726})2SP^{Myc}Homer1a(W24A)+EGFP virus was stereotaxically injected at 350 - 500 μm depth in the somatosensory cortex of three week old rats. Virus injections resulted mainly in the infection of pyramidal neurons in layer 2/3, although some cells of different type were also labeled. After 24 to 36 hours, the animals were used for in vivo time-lapse imaging using two-photon microscopy. This method allowed us to analyze the filopodia/spine density and average length as well as their motility over time (Fig. 3.21A-C).

Analysis from image stacks taken in vivo showed no significant increase of filopodia/spine density for ^{Myc}Homer1a+EGFP expressing neurons compared to control EGFP- and ^{Myc}Homer1a(W24A)+EGFP expressing neurons (Fig. 3.21D; spines per 10 μm = 7.4

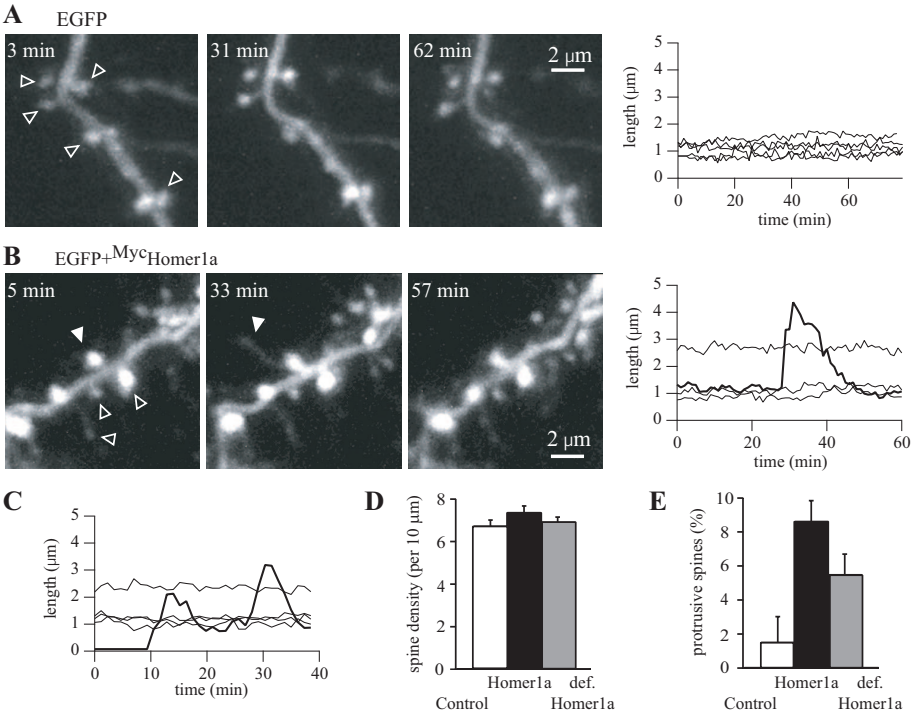

Figure 3.21: Homer1a-expression induces structural changes at the level of dendritic spines in vivo. (**A**) Example images from a time-lapse recording showing a spiny neuronal dendrite in layer 1 (90 μm below the pial surface). Acquisition times are indicated in the upper left corner. The length of the marked spines (arrow heads) were analyzed and are plotted as a function of time on the right. (**B**) Examples of two-photon images of a spiny neuronal dendrite (30 μm below the surface) expressing ^{Myc}Homer1a+EGFP. Acquisition times during the time-lapse recording are indicated. The time courses of spine length are shown on the right (solid arrow head indicates a transient filopodial outgrowth). (**C**) An additional example of a filopodia-like dendritic protrusion in a neuron expressing ^{Myc}Homer1a+EGFP. A new filopodium occurred and showed subsequent elongations and retractions. (**D**) Bar graph of spine density (per 10 μm dendritic branch length) of EGFP, ^{Myc}Homer1a+EGFP and defective ^{Myc}Homer1a+EGFP expressing neurons. (**E**) Bar graph of relative abundance of protrusive spines found in ^{Myc}Homer1a, versus EGFP and ^{Myc}Homer1a(W24A) expressing dendrites.

$\pm$ 0.3, 6.7 $\pm$ 0.3, and 6.9 $\pm$ 0.2, $n = 24$, $n = 20$ and $n = 18$ branches, respectively; P<0.15), with no change in the average filopodia/spine length per branch (^{Myc}Homer1a+EGFP = 1.5 $\pm$ 0.1 μm; EGFP = 1.6 $\pm$ 0.1 μm; ^{Myc}Homer1a(W24A)+EGFP = 1.5 $\pm$ 0.1 μm). Thus rapid expression of Homer1a in cortical pyramidal neurons does not significantly alter the density of dendritic filopodia and spine-like protuberances.

Next, we investigated whether Homer1a may induce dynamic changes of spine morphology in vivo. Time-lapse recordings were performed within cortical layer 1 on distal spiny dendrites of neurons expressing ^{Myc}Homer1a+EGFP, EGFP-only or ^{Myc}Homer1a(W24A)+EGFP. Image stacks containing a selected dendritic branch were collected at approximately 1 min intervals for about one hour, and spine length changes were quantified over time (Fig. 3.21A-C). In the case of EGFP-only expression the spine pattern remained stable over the time period investigated, with spines showing little or no changes in their length (Fig. 3.21A). Only one out of 66 spines analyzed showed a short extension of 0.7 μm. In contrast, ^{Myc}Homer1a+EGFP expressing cells displayed filopodial-like motility in their dendritic branches in about 9% of spines analyzed (Fig. 3.21B-C). This included newly formed protrusions as well as spine elongations and retractions of several micrometer length. Extensions were between 0.6 - 5.3 μm and occurred within 3 - 30 min (median 4.2 min; $n = 6$). Retractions were between 1.4 and 3.5 μm and occurred on a similar rapid time scale (4 - 20 min; $n = 4$). Interestingly, in two cases the outgrowth occurred from a preexisting spine head (Fig. 3.21B). Finally, in the case of ^{Myc}Homer1a(W24A)+EGFP expression 6 out of 109 spines analyzed showed either extension (1.5 - 2.3 μm) or retraction (0.8 - 2.5μm). We conclude that expression of Homer1a induces rapid filopodial outgrowth and/or retraction on dendritic branches of cortical neurons in young adult rats (Fig. 3.21E), which normally show few such structural changes at this age [116] [152]).

3.4.1.2 Calcium Dynamics with Genetically Encoded Calcium Indicators

Two-photon microscopy, however, not only allows optical recordings on the structural plasticity of fluorescently labeled neurons. Using fluorescent Ca^{2+} indicators [194] [146] [181], for example, it enables optical measurements of spatio-temporal intracellular Ca^{2+} dynamics in the intact brain [80] [184]. Ca^{2+} acts as intracellular second messenger controlling a variety of cellular phenomena including, for example, secretion, contraction, and neuronal plasticity. In excitable cells, Ca^{2+} fluxes are closely linked to the cells' electrical activity. Action potential (AP) firing and/or activation of synaptic receptor channels can cause Ca^{2+} influx, which is electrogenic and may itself contribute to regenerative membrane potential changes (such as Ca^{2+} action potentials). Thus, measurements of intracellular Ca^{2+} changes can subserve the monitoring of electrical activity of individual neurons or networks of neurons.

Synthetic Ca^{2+} indicators, however, have significant limitations. First, they cannot be targeted specifically to particular cell types or subcellular compartments. Second, once loaded, synthetic calcium indicators are cleared from the cytoplasm, making long-term imaging experiments difficult. However, genetically encoded Ca^{2+} indicators (GECIs) can

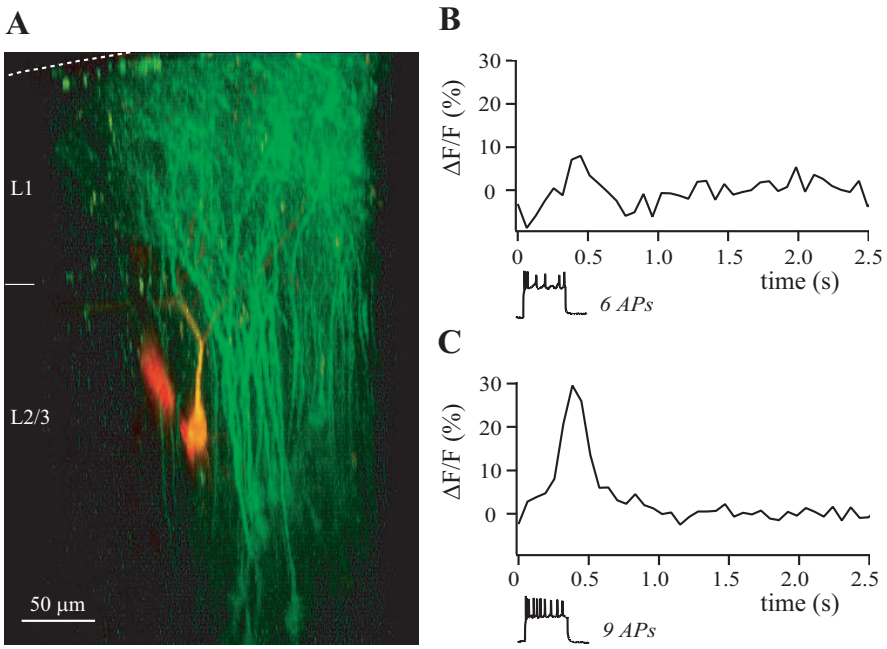

Figure 3.22: Two-photon imaging of GECI-expressing cells in vivo. (**A**) Overview, showing Lentivirus-infected GECI-expressing cells (green) and an Alexa Fluor 594 colabeled infected neuron (red). Colabeling was achieved through TPTP (the micropipette shank is visible as red cylinder left of the colabeled neuron). (**B** and **C**) Calcium transients in GCaMP-expressing cells following somatic current injection (300 ms; 700 pA) during two-photon targeted whole cell recordings. (B) Relative fluorescent change $\Delta F/F$ (in %) in response to 6 APs. (C) Calcium transient evoked by 9 APs.

be delivered efficiently to specific subsets of neurons or neuronal compartments using viral infection [215].

Here, we evaluated the use of lentivirus-mediated GECI expression for the purpose of monitoring neuronal activity in vivo. In particular, we focused on GECIs based on circularly permuted GFPs and the Ca^{2+}-binding protein calmodulin (CaM), namely GCaMP [130] and Inverse Pericam [128].

First, we investigated whether Inverse Pericam (InvP) might report neuronal activity through transient decreases in fluorescence ($n = 3$ animals). In imaging experiments with high temporal resolution (1 - 64 ms), we did not find any spontaneous Ca^{2+} transients in InvP-expressing cells, nor did we find any fluorescence changes in response to surface stimulation with a Tungsten electrode. To test, whether infected cells were still functional we performed two-photon targeted patch recordings (Fig. 3.22A) [122]. Cells recorded in this way, were activated via surface stimulation (50 - 800 ms duration; 10 μA - 3mA amplitude). We found, that even a train of 10 APs could not evoke measurable Ca^{2+} transients in the recorded InvP-expressing cells. In addition, no measurable fluorescence changes were found in response to up to 23 APs following somatic current injections during whole cell recordings ($n = 2$ cells).

Next, we evaluated whether GCaMP might be capable to report neuronal activity in vivo through transient increases in fluorescence ($n = 2$ animals). In one out of 12 cases, we found a measurable Ca^{2+} transient (∼400 ms decay time) as a result of spontaneous firing. However, we did not find clear Ca^{2+} transients in response to surface stimulation (50 - 300 ms duration; 10 μA - 3mA amplitude). To get a quantitative understanding of the relationship between neuronal activity and GECI fluorescence we performed two-photon targeted whole-cell recordings (Fig. 3.22B and C; $n = 2$ cells). Measurable calcium transient were observed above 8 APs at ∼25 Hz firing rate following somatic current injections.

In view of the low firing rates of pyramidal cells and the sparse coding in the neocortex [145], however, we conclude that virus-based GECI expression is currently not well suited for monitoring neuronal activity in the intact brain. However, functional measurements of neuronal calcium dynamics in vivo are feasible through bolus loading of synthetic calcium indicators (see subsection 3.4.2.2), though restricted to a few hours, limited in specificity and spatial precision. In some cases, partial discrimination between the different cell populations in bolus-loaded preparations is possible through counter-staining techniques (see subsection 3.3.2).

3.4.2 Astrocytes

3.4.2.1 Distribution and Structural Dynamics

To further characterize the SR101 staining presented in subsection 3.3.2, we analyzed the in vivo distribution of neocortical astrocytes in detail. Consistent with the territorial organization of protoplasmic astrocytes [133] [207], this distribution was rather homogeneous. Volume densities ranged from $14 \cdot 10^3$ to $28 \cdot 10^3$ cells/mm^3, with an approximately 55% higher density in layer 1 than in layer 2/3 (Table 3.3). In general, astrocyte densities in rats were about 25% higher than in mice. We also analyzed volume densities of microglial cells in CX_3CR1-EGFP mice, which were about 30 - 50% of those of SR101-labeled cells ($7.9 \pm 0.8 \cdot 10^3$ cells/mm^3 and $7.8 \pm 0.6 \cdot 10^3$ cells/mm^3 in layer 1 and layer 2/3, respectively; $n = 3$ animals). Furthermore, we analyzed the average radial density of SR101-labeled cells surrounding individual astrocytes (Fig. 3.17D). Distances between neighboring cell bodies were around 50 μm. The distribution also showed a distinct peak at a mean cell-to-cell distance of approximately 15 μm, corresponding to the frequent observation of pairs of astrocytes whose cell bodies were separated by only a small gap in extracellular space. These pairs constituted 10 - 15% of all SR101-labeled cells (13.5 ± 1.2% for rats, $n = 8$ animals; 9.9 ± 1.3% for mice, $n = 7$ animals; see Fig. 3.17A and Fig. 3.20A for examples).

Time-lapse imaging experiments of up to 10 h showed that SR101-labeled cells were morphologically stable. In addition, they showed no signs of acute phototoxicity such as disintegration of cellular processes (Fig. 3.23A). Furthermore, in TgN(GFAP-EGFP) mice, astrocytes showed no changes in morphology after multiple repeat SR101 application (500 μM) and imaging for up to 3 weeks (Fig. 3.23B). The exact same cells could be found in

	Layer 1 (10^3 cells/mm^3)	Layer 2/3 (10^3 cells/mm^3)
Rat (P13 - P28)	28.1 ± 1.2 (n = 8 animals)	17.9 ± 1.4 (n = 8 animals)
Mouse (P23 - P270)	22.5 ± 2.0 (n = 7 animals)	14.2 ± 1.1 (n = 7 animals)

Table 3.3: Density of SR101-labeled astrocytes in rat and mouse neocortex (mean ± SEM)

successive imaging sessions. In particular, the pairs of astrocytes described earlier remained morphologically unaltered over this time period. In addition, the same staining pattern was observed after repeated SR101 applications (Fig. 3.23C). These short- and long-term imaging experiments demonstrated that overall astrocytes are morphologically stable and that SR101 does not induce phototoxicity over hours, days and weeks and can be applied repeatedly.

Astrocytes form a functional, gap junction-coupled syncytium that is closely associated with microvasculature, presumably controlling extracellular milieu and regulating local blood flow [218] [172]. We were able to demonstrate this close apposition to cortical microvasculature by labeling astrocytes with SR101 and counterstaining the blood plasma with a green fluorescent dye via tail-vein injection. Using this approach, we obtained in vivo visualization of the entire cortical microvasculature being enveloped by processes of SR101-labeled cells (Fig. 3.20B; Suppl. Movie SA4). The endothelial sheet surrounding the blood vessels was visible as an unstained dark gap between astrocyte end feet and fluorescently labeled vessel lumen (Fig. 3.20B). The complete envelopment of microvasculature provides further evidence that all protoplasmic astrocytes are labeled by SR101 near the application site.

These examples demonstrate how SR101 labeling can be used in both short- and long-term studies to characterize morphological features of astrocytes as well as their close structural relationship to other cortical elements in vivo.

3.4.2.2 In Vivo Calcium Dynamics

As pointed out in subsection 3.4.1.2, SR101 labeling can be employed as a counterstain to discern astrocytes from other cortical cells in less specific staining techniques. In particular, it can be employed to enable functional imaging of astroglial and neuronal Ca^{2+} signaling in vivo.

Astrocytes form a cellular network that is closely associated with neuronal networks [18]. Changes in intracellular calcium levels are thought to be a prominent signaling mechanism not only between astrocytes but also for the communication between astrocytes and neurons [60] [8] [202]. Although slow Ca^{2+} oscillations [27] [149] and Ca^{2+} waves [32] [35] [27] have been characterized in cell culture and brain slices, the presence and characteristics of such signals in vivo have not been clearly established (but see ref. [83]).

Using SR101 as a specific marker for astrocytes, we were able to distinguish calcium signals unambiguously in the astroglial and neuronal network in vivo. For calcium-indicator

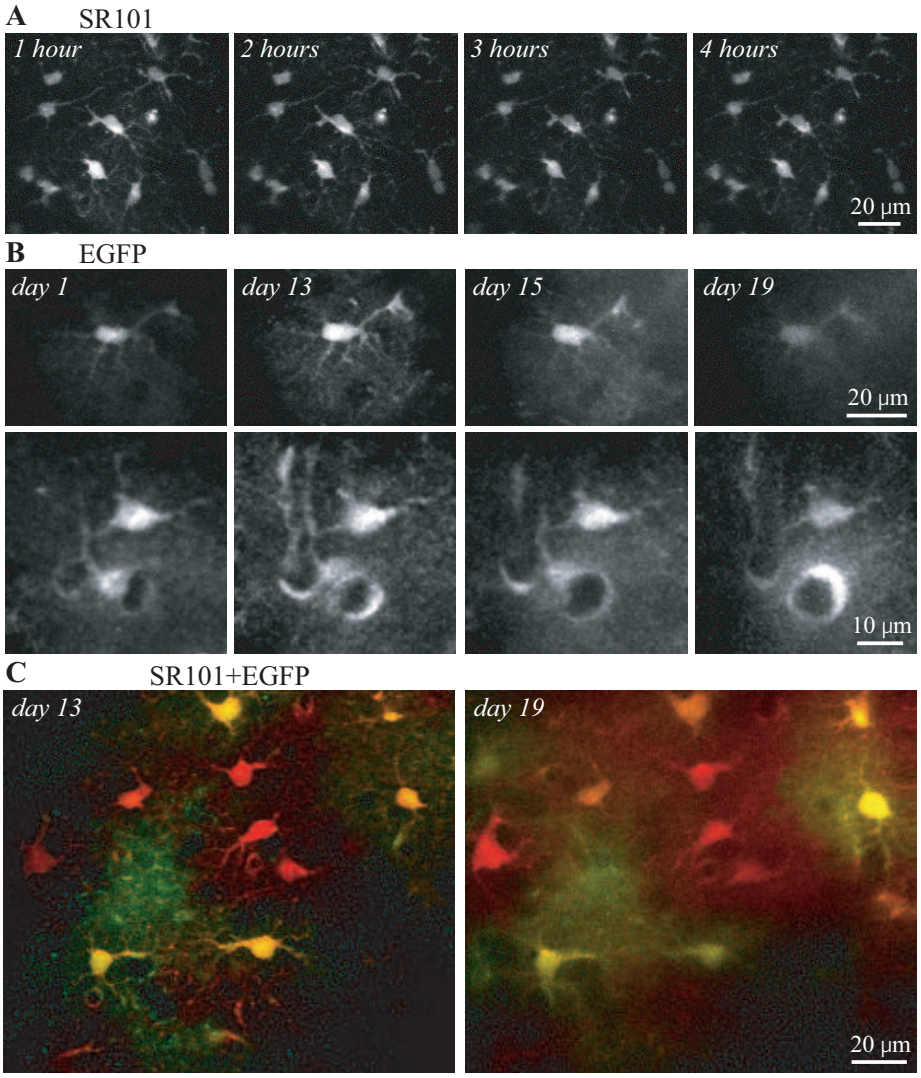

Figure 3.23: SR101 staining shows no signs of acute or long-term phototoxicity and can be applied repeatedly. (**A**) Example images from a 10 hour in vivo time-lapse recording in a P27 rat. Acquisition times are indicated. Each image is a maximum-intensity projection of a stack of fluorescence images that sampled a $105 \times 95 \times 16$ μm^3 cortical volume in 3 μm steps in layer 2/3. Stacks were recorded every 5 minutes. Astrocytes were labeled via brief surface application of 100 μM SR101. On a timescale of several hours, SR101-stained cells were morphologically stable with no signs of acute phototoxicity. (**B**) Example images from a long-term in vivo imaging experiment in a P223 TgN(GFAP-EGFP) transgenic mouse. Acquisition times during the time-lapse recording are indicated. Images are maximum-intensity projections of fluorescence image mini-stacks (2 μm steps). Each row shows an EGFP expressing SR101-positive astrocyte in cortical layer 2/3 that was imaged on four days within a period of three weeks. SR101 (500 μM) was applied repeatedly on days 1, 13 and 19. Under these conditions, the imaged cells showed preserved morphology with no signs of activation on a timescale of three weeks. (**C**) Overview recorded on day 13 and 19 (corresponding to the second and third application of SR101) in the same animal as in (B) about 220 μm below the pial surface. Images are maximum-intensity projections of three subsequent fluorescence image planes (2 μm axial spacing). The 'green' EGFP and the 'red' SR101 channel were merged to yield an RGB image. Cells that appear yellow are EGFP- and SR101-positive. The same cells were stained by SR101 following repeated application over the course of several days.

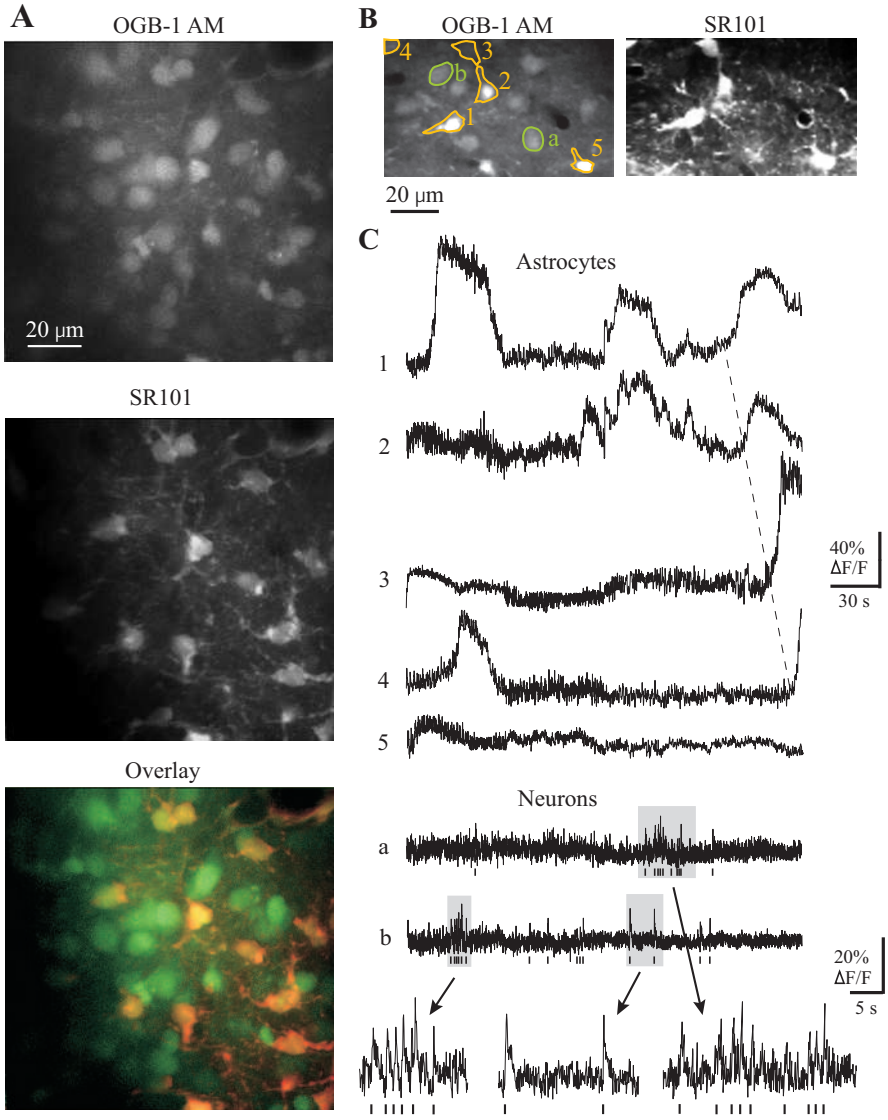

Figure 3.24: Simultaneous calcium imaging of neuronal and glial networks in vivo. (**A**) Two-photon fluorescence images of cells in layer 2/3 of rat neocortex labeled by intracortical pressure ejection of the membrane-permeant calcium indicator dye OGB-1 AM (top). Astrocytes were identified through additional surface application of 100 μM SR101 (center), which permitted a clear separation of the astroglial (yellow) and neuronal (green) network (overlay, bottom). (**B**) Left, OGB-1 AM-labeled cells in a different experiment. Right, corresponding SR101 reference image for astrocyte identification. Astrocytes and neurons are indicated with numbers and lower-case letters, respectively. (**C**) Spontaneous calcium transients in the astrocytes and neurons indicated in B measured as relative fluorescent change $\Delta F/F$ over a time course of several minutes. Neuronal calcium transients during the highlighted periods are shown on an expanded time scale (bottom traces). Presumed spike patterns are indicated as raster plots below the traces. Note the different time courses of the astroglial and neuronal transients.

loading of cell populations, we used multicell bolus loading [181] with Oregon Green 488 BAPTA-1 acetoxymethyl (AM) ester (OGB-1 AM), which resulted in the staining of virtually all cells within a sphere several hundred microns in diameter. After 30 min, all cells near the ejection site, including neurons and astrocytes, had taken up the calcium indicator (Fig. 3.24A). Although glial cells sometimes could be recognized because of a higher fluorescence intensity [181], a complete separation of neurons and astrocytes was not possible based on their appearance. Astrocytes, however, could be identified through additional staining with SR101 (Fig. 3.24A). Because the red fluorescence of SR101 can be easily separated from the green fluorescence of OGB-1, the red fluorescence channel can serve as a reference image to identify astrocytes (Fig. 3.24B).

We monitored spontaneous calcium signals in cortical layer 2/3 cells over several minutes at a temporal resolution of 15 Hz. Spontaneous calcium transients occurred in both neurons and astrocytes; however, they showed markedly different kinetics (Fig. 3.24C). Astroglial calcium signals were characterized by slow onsets of about 10 s (10 - 90% rise time 13.2 ± 6 s) and subsequent plateau-like elevations that lasted for several tens of seconds (half width 19.0 ± 2.4 s; $n = 6$). They often showed an oscillatory behavior, occurring repeatedly in individual astrocytes. Calcium signals were not necessarily synchronized between astrocytes. Rather, calcium elevations in some cases appeared to propagate from one astrocyte to neighboring cells in a wave-like fashion (Fig. 3.24C). In contrast, neuronal calcium signals were characterized by fast fluorescence transients (mean $\Delta F/F$ peak amplitude 11.2 ± 2%, $n = 4$) with a single-exponential decay and a time constant of 0.37 ± 0.05 s ($R^2 = 0.98$, $n = 4$). These transients are consistent with somatic calcium influx evoked by action potentials [184] [205] and therefore can be used to deduce an estimate of the neuronal spike patterns (Fig. 3.24C). There was no significant difference between neuronal calcium transients from preparations stained with both SR101 and OGB-1 and preparations that were stained with OGB-1 alone ($P = 0.87$).

Thus, SR101 application in conjunction with calcium indicator loading permits simultaneous measurements of neuronal spiking activity (with single AP precision [99]) and glial calcium signaling in vivo. Hence, this method promises to enable studies on neuron-glia communication and, in particular, imaging of cellular network activity in behaving animals (see subsection 3.2).

3.4.3 Microglia

Apart from astrocytes, there are two other major glial cell types present in the cortex, oligodendroctes and microglial cells. Microglial cells are the primary immune effector cells in the brain. In response to any kind of brain damage or injury, microglial cells become activated and undergo morphological as well as functional transformations. They are critically involved in lesions, neurodegenerative diseases, stroke, and brain tumors [109] [180] [182] [183]. Resident microglial cells in the healthy brain are thought to rest in a dormant state, while activation is associated with structural changes, such as motile branches or migration of somata [140] [179]. However, since most tissue preparations represent injuries by themselves, key aspects of microglia function have remained

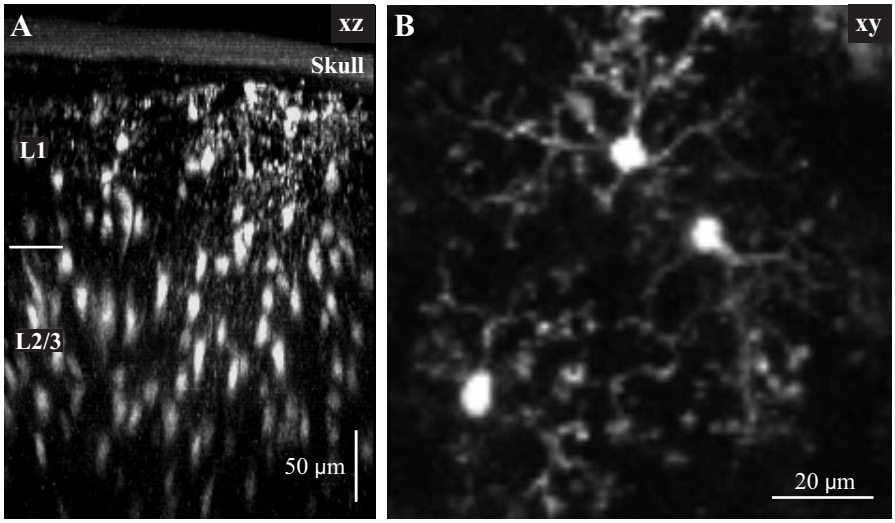

Figure 3.25: Transcranial 2-photon imaging of EGFP-expressing microglial cells in the neocortex of transgenic mice. (**A**) Side projection showing an even distribution of microglial cells in layers 1 through 2/3. The thinned (fluorescent) skull is visible on top. (**B**) Maximum-intensity projection of microglial cells in layer 1 of a 1 year old mouse (40 - 60 μm below the pial surface).

elusive.

3.4.3.1 Structural Dynamics in the Healthy Brain

Here, we investigated microglia behavior in the intact adult brain both during the resting state and immediately after local injury using in vivo two-photon microscopy [43]. Fluorescence images were acquired transcranially using a thinned-skull preparation (Fig. 3.25A) (see subsection 7.2.3), except for cases that required direct access to the brain. Microglial cells had small rod-shaped somata from which numerous thin and highly ramified processes extended symmetrically (Fig. 3.25B). Their three-dimensional distribution in vivo was rather homogeneous, displaying a territorial organization with typical cell-to-cell distances of 50 - 60 μm and volume densities of $6.5 \pm 0.6 \cdot 10^3$ cells/mm^3 and $6.4 \pm 0.4 \cdot 10^3$ cells/mm^3 in layer 1 and layer 2/3, respectively ($n = 6$ animals).

Time-lapse imaging experiments of up to ten hours, showed that somata of microglial cells generally remained fixed with only few signs of migration (5% of somata shifted their position by 1 - 2 μm per hour; 99 total cells; $n = 12$ animals). In contrast, microglial processes were remarkably motile, continuously undergoing cycles of de novo formation and withdrawal. This structural dynamics occurred on a time scale of minutes leading to

comprehensive changes in cellular morphologies within one hour except for a small scaffold of stable branches (Fig. 3.26A; Suppl. Movies SM1 and SM2). To quantify motility we measured the velocity of length changes of individual processes. On average, extensions and retractions had similar velocities of 1.47 ± 0.10 μm/min and 1.47 ± 0.08 μm/min, respectively (Fig. 3.26B and C; range: 0.4 - 3.8 μm/min; 95 extensions and 147 retractions in 14 cells, $n = 8$ animals; typically, thick branches were on the lower end of this range). Branch additions and losses occurred at every branch order and balanced each other (Fig. 3.26D).

Microglia processes also displayed highly motile filopodia-like protrusions of variable shape, typically forming bulbous endings (Fig. 3.26E; Suppl. Movie SM3). Such protrusions transiently and sometimes repeatedly appeared at various locations along the main processes and at their terminal endings. Often protrusive activity stalled for several minutes before further extension (or retraction) occurred (Fig. 3.26F). Time-lapse imaging at high temporal and spatial resolution revealed a high turn over of protrusions with velocities of up to 4.1 μm/min (extensions and retractions had similar rates; total average: 2.2 ± 0.2 μm/min; range: 0.6 - 4.1 μm/min; 22 extensions and 23 retractions on 2 cells in 2 animals). The average lifetime of such protrusions was 3.9 ± 0.2 min (Fig. 3.26F and G; 72 protrusions in 3 cells; $n = 3$ animals; range: 1.7 - 8.3 min). Despite the constantly changing decoration of microglial processes with protrusions, the number of sites per cell showing protrusive activity remained rather constant over time (Fig. 3.27A and B; mean 19.3 ± 5.3; $n = 8$ cells), as did the average total length of microglial processes (Fig. 3.27B).

Microglial processes and protrusions sampled the extracellular space in a seemingly random fashion and at a high turn over rate. To quantify the volume fraction surveyed by microglia per time, we analyzed cumulative maximum-intensity projections through time-lapse recordings (Fig. 3.28A; see also subsection 7.2.3), yielding a progressive filling rate of 14.4 ± 1.6% per hour ($n = 8$ animals; Fig. 3.28B). Considering that the volume fraction of extracellular space is estimated to be about 20% [115], this suggests that the brain parenchyma is completely screened by resting microglia once every few hours. In doing so, microglial cells vary their territories. Border zones between neighboring microglial cells were mutable and changes in favor of adjacent cells often occurred after retraction of thick processes in another cell. When processes of neighboring microglial cells encountered one other, endings mutually repelled each other.

This high resting motility may serve a housekeeping function, enabling microglial cells to effectively control the microenvironment and to clear the parenchyma of accumulated (low diffusible) metabolic products and deteriorated tissue components. Indeed, branch protuberances of microglial cells were short-lived and typically showed bulbous endings, indicating that tissue material had been collected. In a few cases, we observed spontaneous engulfments of tissue components, which subsequently were transported towards the soma (Fig. 3.28C; Suppl. Movie SM4). To further reveal the interaction between microglia and other cortical elements, we counterstained astroglia using the red fluorescent dye SR101 [138]. Control imaging experiments before, during, and after SR101 application showed no adverse effects of SR101 itself on microglia motility ($n = 4$ animals). Unlike microglial cells, astrocytes showed no comparable restructuring of their processes. The SR101 counterstain also enabled us to visualize neuronal cell bodies and cortical blood vessels, which appear as

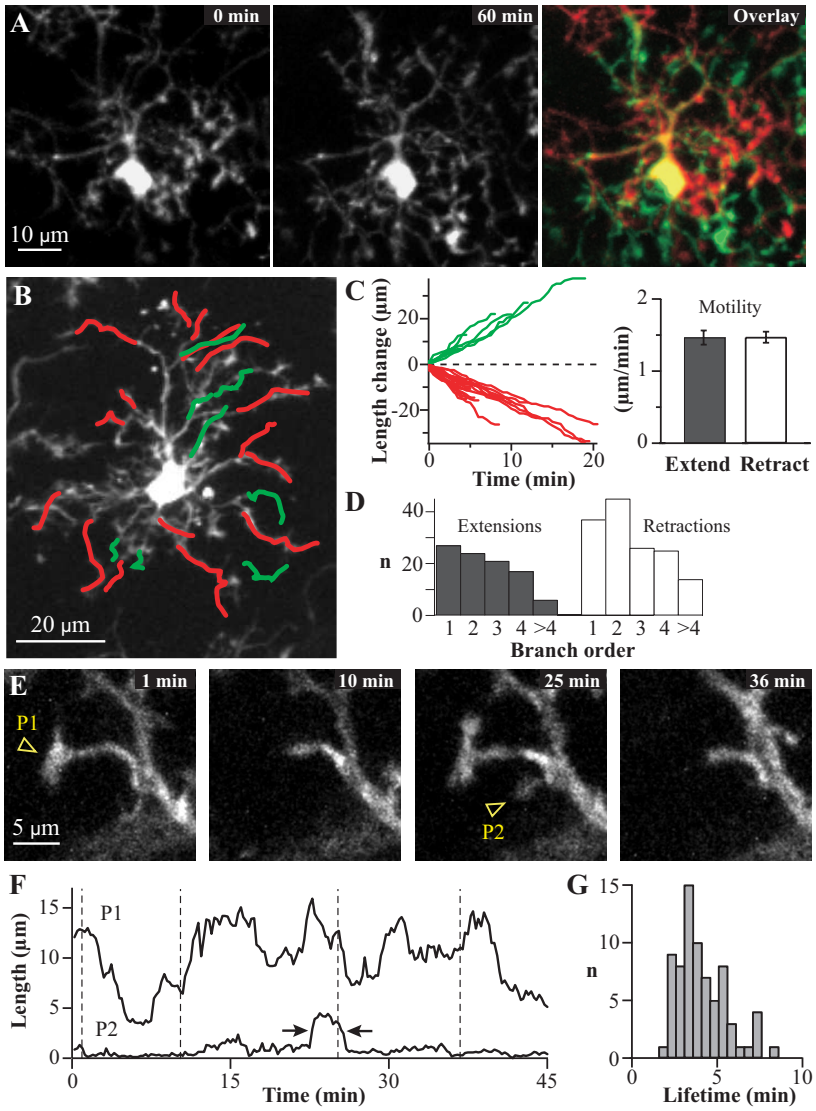

Figure 3.26: Microglial cells are highly dynamic in the resting state in vivo. (**A**) Maximum-intensity projections of an individual microglial cell (45 - 75 μm below the pia) at the beginning (left) and one hour after (center) the start of a transcranial time-lapse recording. Right, overlay showing extensive formation (green) and deletion (red) of microglial processes. (**B**) Extensions (green) and retractions (red) of processes over the time course of 20 minutes. (**C**) Length changes of the processes shown in (B) as a function of time. Right: Mean motility values in μm/min for extensions and retractions. (**D**) Branch motility occurred at every branch order. (**E**) Example images of microglial protrusions from a time-lapse recording. (**F**) Length changes over time of the two protrusions P1 and P2 indicated in (E). Vertical dashed lines mark the acquisition times of the images shown in (E). (**G**) Lifetime histogram of protrusions.

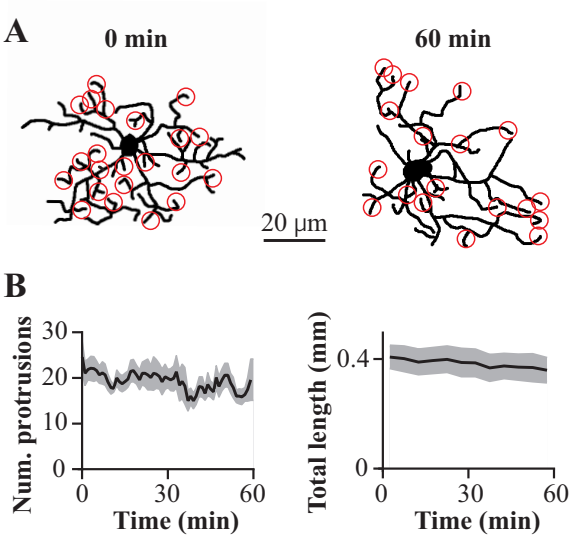

Figure 3.27: Microglia sample their microenvironment in a seemingly random fashion. (**A**) Sites of protrusive activity (red circles) overlaid on the scaffold of processes in an exemplary cell at time zero and one hour later. (**B**) Number of protrusive sites (left) and total length of microglial processes (right) as a function of time (mean and standard error from 8 cells in 5 animals are shown in grey).

unstained dark areas (Fig. 3.28D). Microglia processes and protrusions directly contacted astrocytes, neuronal cell bodies and blood vessels, suggesting that in the healthy brain microglia dynamically interact with other cortical elements (Fig. 3.28D; Suppl. Movie SM5).

Microglia are thought to monitor neuronal well-being through molecular changes in the microenvironment and to provide neurotrophic factors if required [200]. Therefore, we investigated whether microglia surveillance behavior is regulated by neuronal activity. The level of neuronal activity was either increased or reduced by surface application of the ionotropic GABA receptor blocker bicuculline (BCC; 50 μM) or the sodium channel blocker tetrodotoxin (TTX; 25 - 50 μM), respectively. The effectiveness of drug application was verified from simultaneous electrocorticogram (ECoG) recordings (Fig. 3.29A). Neither BCC nor TTX had a significant effect on microglia motility, as evaluated by the average velocity of microglial processes before and one hour after drug application (BCC: $p > 0.6$; 50 and 43 processes, respectively; $n = 3$ animals; TTX: $p > 0.25$; 67 and 97 processes, respectively; $n = 3$ animals; Mann-Whitney U-test). A change in microglia surveillance behavior was evaluated by measuring the ratio of fluorescence intensities before and after drug application in an outer (distal) and inner (proximal) ring surrounding individual microglial cell bodies (Fig. 3.29A, dashed red lines). In addition, the total length of processes per cell was evaluated. Application of BCC caused a significant increase in the outer-to-inner fluorescence ratio, indicating a more extensive volume sampling. (Fig. 3.29B, top; Suppl. Movie SM6; 129.1 $\pm$ 7.8%, values normalized to pre-application period; $p < 0.001$; t-test; 18 cells; $n = 3$ animals). The average total branch length per cell showed

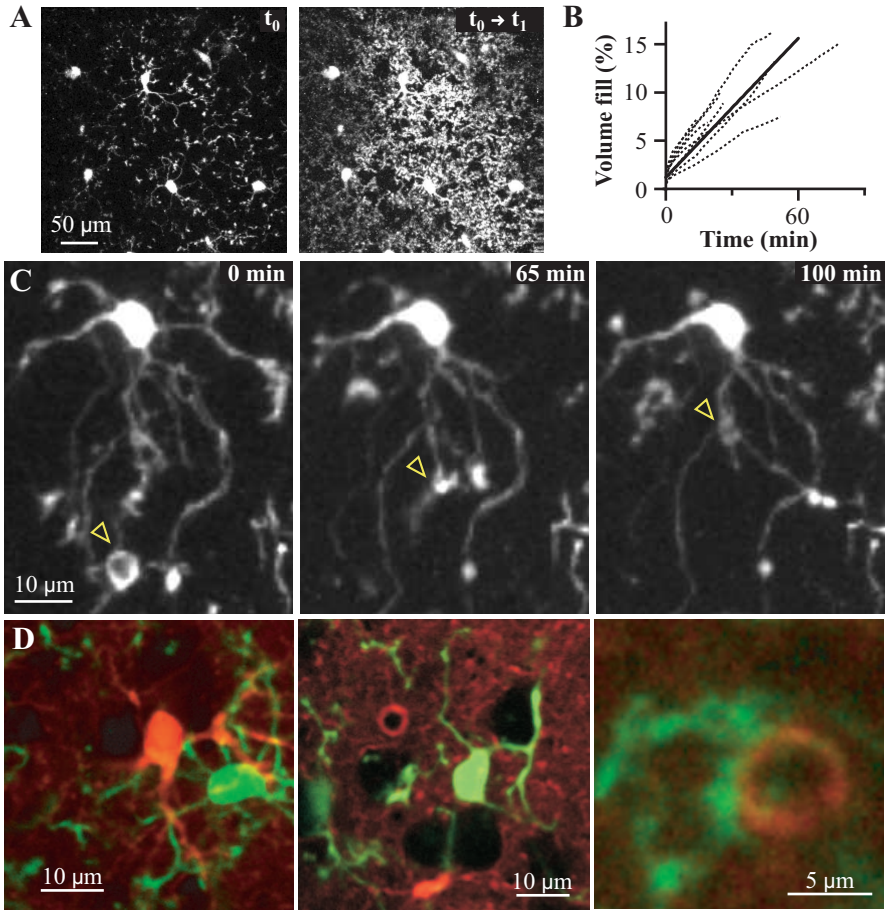

Figure 3.28: Resting microglia continuously sample their microenvironment and dynamically interact with other cortical elements. (**A**) Examples images illustrating cumulative volume sampling. Left, initial image at time t_0. Right, cumulative projection at a later time point t_1 (see subsection 7.2.3). (**B**) Quantitation of volume sampling. Dashed lines, percentage increases for individual cells; solid line, average trace. (**C**) Example images from a time-lapse recording showing spontaneous engulfment and subsequent evacuation of tissue components by microglial processes (yellow arrow-head). (**D**) Example images showing how microglial processes and protrusions contact neighboring astrocytes (left), neuronal cell bodies (center; unstained dark areas), and the astrocytic sheeth around a microvessel (right). Images are overlays of the green microglia and red SR101 stain.

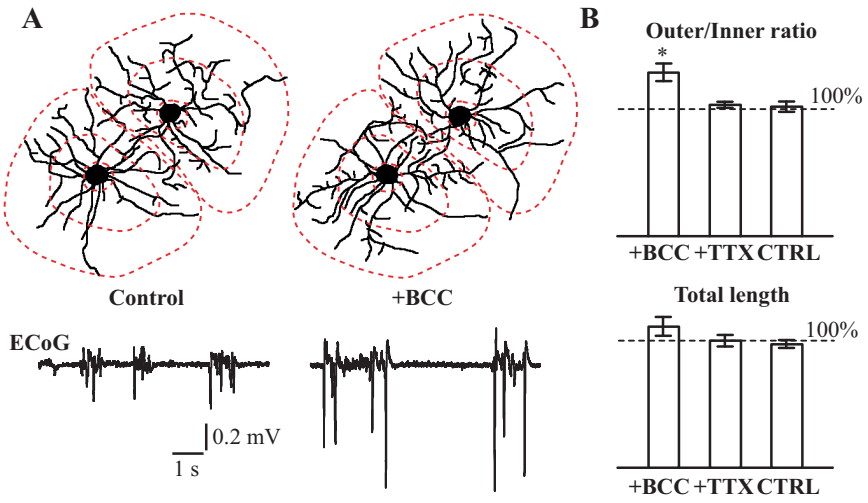

Figure 3.29: Dependence of microglia surveillance behavior on the level of neuronal activity. (**A**) Top, morphology of two exemplary microglial cells before and one hour after surface application of BCC. Dashed red lines indicate the outer (distal) and inner (proximal) rings used to evaluate changes in volume surveillance. Bottom, corresponding ECoG traces showing a BCC induced increase in neuronal activity by occurrence of large-amplitude, synchronized spikes. (**B**) Changes in the outer-to-inner fluorescence ratio (top) and the total length of microglial processes per cell (bottom) with surface application of BCC, TTX, or extracellular saline (CTRL). Ratios represent values one hour after, divided by values immediately before drug application (given in percentage). The mean total length before drug application was 482 ± 20 μm (32 total cells; $n = 7$ animals).

a small, yet not significant increase (Fig. 3.29B, bottom; 112.0 ± 7.4%; p = 0.13; 13 cells; n = 3 animals). Notably, the effect of BCC on microglia surveillance behavior was reversible and repeatable. In contrast, application of TTX had no significant effect on either the outer-to-inner fluorescence ratio or the average total branch length per cell (Fig. 3.29B; p > 0.05; 27 and 14 cells, respectively; $n = 3$ animals). In addition, no significant change was seen over time in three control experiments using surface application of extracellular saline (Fig. 3.29B; p > 0.4; 19 and 16 cells, respectively; $n = 3$ animals).

3.4.3.2 Response to Local Injury

Another likely function of the high resting microglia motility is to facilitate prompt reactions to brain injury [140]. We therefore characterized microglia activation immediately after targeted disruption of the BBB at the level of individual capillaries (Fig. 3.30). Vessel outlines were visualized using SR101 application. After a baseline imaging period, individual capillaries of about 6 μm diameter were damaged using highly localized laser lesions either through the thinned skull or through a small cranial window (Fig. 3.30A; Suppl. Movie SM7). Disruption of the BBB was indicated by local tissue expansion and detachment of astroglial end feet. Laser lesions caused extravasation of dye in 3 experiments, in which blood plasma was stained via tail-vein injection of a dextran-conjugated

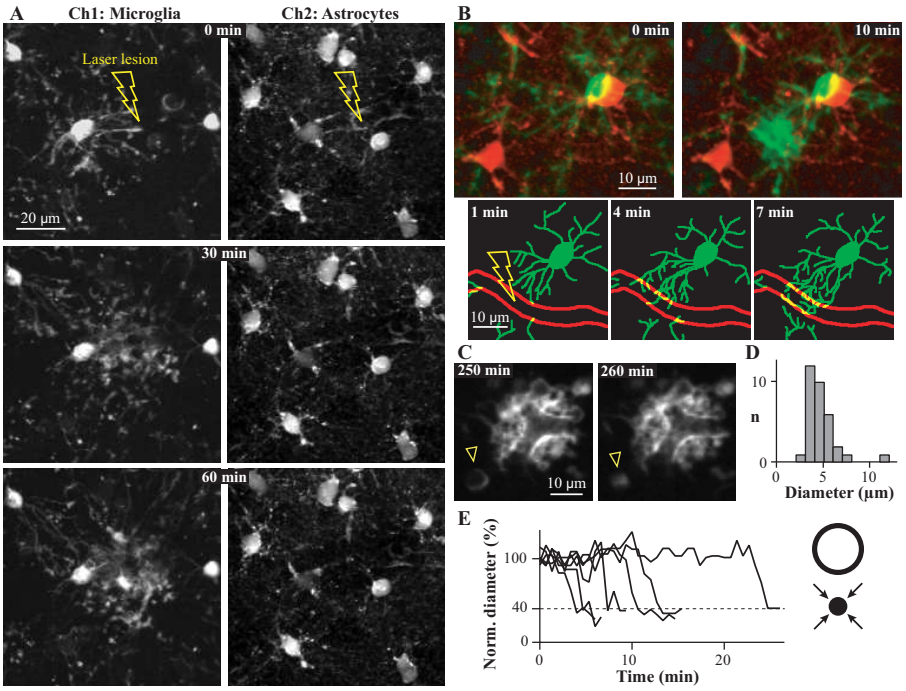

Figure 3.30: Microglia are rapidly activated following local BBB disruption. (**A**) Fluorescence images of EGFP-expressing microglial cells (Ch1) and SR101 counterstained astrocytes (Ch2) before, 30 min, and 60 min after a targeted laser-induced microlesion. The disrupted blood vessel is apparent in Ch2 (yellow flash indicates the site of injury). (**B**) Rapid shielding of a lesioned blood vessel section. Top, overlay of green microglia and red astrocyte stain before and 10 min after the laser-induced lesion. Bottom, microglia morphology at intermediate time points showing rapid, targeted movement of microglial processes towards the injured blood vessel (outlined in red; yellow flash indicates the site of injury). (**C**) Activated microglia processes at the site of laser lesion about 4 hours after injury. Several spherical engulfments are visible in the vicinity of the lesioned blood vessel arborization. (**D**) Histogram of the diameter distribution of 33 post-lesion engulfments. (**E**) Example time courses of spherical shaped engulfments. Diameters are normalized to initial values.

fluorescent dye (Suppl. Movie SM8). Laser lesions induced an immediate microglia response, indicated by a switch from undirected to targeted movement of nearby microglial processes towards the injured site (Fig. 3.30B; Suppl. Movie SM7 and SM9). The average velocity of extensions radially impinging on the injured site was similar to extension rates during the resting state (mean 1.8 $\pm$ 0.3 μm/min; $n = 5$ animals). Processes on the far side of activated microglial cells subsequently started to retract.

The number of responding microglial cells depended on the severity of the injury. In general, only microglial cells in the immediate vicinity of the microlesion were activated, while cells farther away (>90 μm) did not or not immediately respond. In two cases, laser lesions caused a transient activation of only a single microglial cell. In those cases, no measurable tissue expansion was observed, indicating only mild damage to the BBB. Yet in all lesion experiments, shielding of the injured area through accumulation of microglial

extensions was observed (Fig. 3.30B; Suppl. Movie SM10). In cases of severe BBB disruption, multiple spherical shaped inclusions started to form around 10 - 15 min after the lesion, indicating phagocytic activity by microglial processes. Inclusions were found within 15 - 25 μm radial distance of the injured site, showing diverse dimensions with an average diameter of 4.6 $\pm$ 0.3 μm (Fig. 3.30C and D; Suppl. Movie SM11; range: 4.6 - 11.1 μm; $n = 34$; 2 animals). Inclusions were stable for several minutes (mean: 11.6 $\pm$ 1.9 min; range: 1.8 - 23.9 min) before they rapidly collapsed (mean 2.0 $\pm$ 0.5 min; $n = 14$; 2 animals) to around 40% of their initial size (Fig. 3.30E). Notably, the larger the inclusions were the shorter their lifetime. Within the observation period (up to 5.5 hours), somata of microglial cells became more rounded. They did not, however, migrate towards the injured site. Interestingly, SR101 co-labeled astrocytes showed no morphological response to the laser-induced microstroke.

A switch from undirected surveillance behavior to targeted movement of microglial processes was also observed in response to local application of lipopolysaccharide (LPS; 1 mg/ml) as a means to mimic gram-negative infection [197] [1]. Brief intracortical application of the endotoxin through a micropipette (see subsection 7.2.3) evoked immediate and targeted outgrowth of microglial processes towards the application site ($n = 2$ animals). Microglial cells started to form a dense meshwork of processes ($\sim$40 μm diameter) around the LPS application site (Suppl. Movie SM12). Branches on the far side of activated microglial cells were retracted, resulting in a highly polar branch pattern. Within the observation period (up to 6.5 hours), distant microglial cells (>100 μm away from the application site) did not respond to the localized inflammatory stimulus.

Chapter 4

Discussion

In this work, we have advanced two-photon microscope miniaturization in parallel to developing in vivo fluorescence labeling techniques for the purpose of enabling functional imaging in behaving animals. We have combined both techniques to demonstrate fiber-based two-photon imaging of cellular populations in the intact brain [136], although currently not a functional level.

4.1 Advancements in Microscope Miniaturization

In vivo fluorescence labeling is a prerequisite for investigation of biological structure and function using two-photon fluorescence microscopy. Live imaging in awake behaving animals, in addition, requires microscope miniaturization.

4.1.1 Single Fiber Based Two-Photon Microscope

We have presented an improved miniature two-photon microscope based on fluorescence excitation through a hollow-core PCF for the purpose of high-resolution fluorescence imaging in behaving animals. Furthermore, we have demonstrated its application to imaging of cellular networks in layer 1 and 2 of the intact rat neocortex.

Using a hollow-core PCF allowed nearly distortion free propagation of high-energy femtosecond pulses close to the zero-dispersion wavelength ($\sim$810 nm) with $\geq$50% of the input power transmitted through the fiber. The delivery of high-peak-power pulses with preserved pulse width permits efficient two-photon excitation, increased imaging depth, and reduced photodamage. An increased imaging depth might also be achieved by shifting the optimal wavelength towards the 'red'. In particular, this would utilize the increased two-photon absorption cross-section of many fluorophores at higher wavelengths. A shift in the fiber's optimal wavelength, however, requires the use of appropriate dispersion delay lines, which comes at the cost of lower transmitted average power. Due to the quadratic dependence of the two-photon absorption rate on excitation intensity, a reduced transmitted average power may counterbalance the enhanced imaging depth achieved through use of longer wavelength light.

The only problem encountered so far with the hollow-core PCF was a reduction in transmitted average power over time (transmission drop to less than 20%), presumably caused by water condensation in the hollow cores of the photonic crystal at the fiber end faces. Although with a fresh cleave fiber transmittance can be restored to around 50%, repeated fiber cleaving is not viable at the scan end as it requires anew assembly and calibration of the scanner, as well as beam alignment in the microscope headpiece. A solution to this problem might be sealing the fiber end faces with ultra-thin glass plates or special adhesives.

Fluorescence light was collected through the microscope objective, coupled into a flexible large core OPF and detected with stationary PMTs. The use of a large-core fiber for fluorescent light collection effectively reduces the weight of the head-mounted microscope and enables dual-wavelength channel detection. However, employing a supplementary fiber for fluorescent light collection involves additional losses, particularly at large imaging depth, that can only in part be compensated for by improved detection capabilities. Improved fiber collection efficiencies might be achieved by employing liquid-core lightguides [46].

Remote positioning of the FOV was achieved using a custom-made motorized mirror-holder, capable of FOV changes on the order of several tens of micrometers. Although well suited for selecting an appropriate imaging spot or correcting image drifts, the motorized tilting stage does not allow for real time adjustment of sudden image shifts (e.g. following rapid head movements). In fact, FOV changes induced by sudden shifts of the brain relative to the skull are independent of microscope design and therefore difficult to balance [79].

A further reduction in weight of the miniature head-mounted microscope could be achieved by use of different materials for casing and holders. A different scanning mechanism [167] [45] may allow further miniaturization, as may the restriction to one aspheric lens for both light collimation and large-core fiber coupling using a modified headpiece layout. Weight reduction to below 3g (which then would allow application to mice), however, might be achieved only at the cost of lower resolution [64].

In conclusion, the improved miniature two-photon microscope based on fluorescence excitation through a single optical fiber is suited for in vivo imaging in a manner similar to a stationary two-photon microscope, although with somewhat reduced resolution and depth penetration [79]. In combination with the novel labeling techniques described in section 3.3, it is expected to yield first insights into the cortical activity patterns that underly animal behavior.

4.1.2 Coherent Fiber Bundle Based Two-Photon Microscope

Furthermore, we have developed an ultrasmall and light two-photon microscope based on the combination of a coherent fiber-optic image guide and a GRIN lens objective. Two-photon fiber-bundle microscope images with near-micrometer resolution were obtained in rat brain in vivo. The advantages of the fiber-bundle microscope are its compactness, flexibility, and the use of GRIN rod lenses, which can be endoscopically inserted in tissue [117] [91]. A major current limitation is suboptimal fluorescent excitation due to nonlinear pulse broadening in the fiber cores, which is mainly caused by self-phase modulation.

Although nonlinear pulse broadening can be entirely avoided in specialty single-air-core fibers [65], other approaches will have to be applied in the case of the fiber bundle, e.g., pulse shaping of the input pulses [31] [193] or pulse energy splitting by special lasers, providing n-fold higher repetition rate and $1/n$-fold shorter pulses (W. Denk; personal communication). Rapidly improving GRIN lens designs may enhance spatial resolution.

In contrast with confocal designs [105], the two-photon fiber-bundle microscope does not depend on fluorescent light collection through the illuminated fiber core but can utilize light collected through all the fiber cores. The detected signal possibly can be further increased with fluorescence collection through a separate large-core detection fiber.

Overall, we expect the fiber-bundle microscope to supplement standard two-photon microscopy, the penetration depth of which is limited to approximately 1 mm near the tissue surface [188]. The fiber-bundle microscope promises to permit flexible endoscopic imaging from deep within various tissues and thus may be useful for optical biopsy and for functional measurements from deep brain nuclei in behaving animals.

4.2 Fluorescence Labeling and Imaging of Neocortical Cell Populations In Vivo

Furthermore, we have developed population staining techniques for neurons, astrocytes and microglia. We have shown, that viral infection allows targeted and specific expression of fluorescent proteins in pyramidal cells. Expression of GECIs for the purpose of functional population imaging, however, was found to be impractical due to the currently low sensitivity of these indicators at low firing rates. We have discovered a simple method for rapid and specific staining of neocortical astrocytes in vivo. In combination with functional synthetic calcium indicators this allows simultaneous imaging of astroglial and neuronal calcium signalling. In particular, we found that astrocytes and neurons exhibit strikingly different calcium dynamics. In addition, we provide first evidence that astroglial calcium oscillations and waves do exist in vivo. Furthermore, we employed transgenic mice expressing EGFP in microglial cells. Functional labeling of microglia was not achieved.

We applied the above-mentioned staining techniques to investigate the structural dynamics of neurons, astrocytes and microglia in the adult brain. We found that neurons and astrocytes are highly stable structures with only very little changes occurring on a synaptic level and on a timescale of several hours. Other studies have shown, that this is true even on a longer timescale (days to weeks) [69] [190]. In contrast, microglia were found to be highly dynamic, undergoing continuous restructuring of their processes on a timescale of minutes and to react promptly to brain injury. The following subsections discuss the above-mentioned results in more detail.

4.2.1 Neurons

(a) Sindbis Virus-Based Expression System.

We have shown that our modified Sindbis-virus expression system is well suited for rapid short-term FP expression in neurons with attenuated cytotoxicity [102].

Furthermore, we have demonstrated high-resolution time-lapse imaging of dendritic spine morphology of cortical neurons in vivo, similar to a recent report [116]. In addition, we have employed a SINrep(nsP2S^{726}) vector containing two subgenomic promoters to overexpress the neurospecific IEG Homer1a (together with EGFP outlining cell morphology). In mammals, there are three Homer gene families, Homer1-3, which comprise seven isoforms (reviewed in [209]). Constitutively expressed Homer isoforms contain two distinct protein modules: a C-terminal Ena/VASP homology 1 (EVH1) domain and an N-terminal coiled-coil (CC) domain. The IEG Homer1a notably lacks the CC domain. Homer EVH1 domain binds to the metabotropic-type glutamate receptors (type I mGluRs), postsynaptic cytoskeletal protein Shank, inositol-1,4,5-triphosphate (IP_3) receptor and ryanodine receptor (reviewed in [56]). The Homer CC domains, in turn, can dimerize, allowing Homer proteins to act as molecular linkers for their EVH1 domain-binding partners. The lack of the CC domain in Homer1a suggests that Homer1a may antagonize protein-protein interactions mediated by Homer dimers by acting as a dominant negative. Thus, overexpression of Homer1a may disrupt protein-protein interactions mediated by Homer dimers and interfere with the Homer1b-Shank postsynaptic scaffold, leading to less stable cytoskeletal organization of dendritic spines and/or decoupling internal calcium stores from synaptic signaling. Although the SINrep(nsP2S^{726})2SP-driven expression well resembles the dynamics of activity-based endogenous Homer1a, we did not find a significant effect of Homer1a overexpression on overall spine density in vivo. Nevertheless, dendritic spines of ^{Myc}Homer1a-expressing pyramidal neurons in layer 1 showed increased protrusive dynamics, as compared to EGFP and ^{Myc}Homer1a(W24A)-expressing cells. Other studies have found, that Homer1a overexpression in hippocampal neurons in culture [164] induces overall loss of spines, from ∼4 to ∼2 per 10 μm of dendritic length, with concomitant loss of synaptic accumulation of Shank, PSD-95 and GKAP, and decrease of AMPA receptor synaptic currents [164]. The morphology of the transfected neurons, however, was evaluated after a much longer expression period than used in our study (4 - 5 days versus 1 - 1.5 days, respectively) and it is possible that a transient period of filopodial outgrowth eventually results in the collapse of the affected spines. In addition, neurons in culture may show a differential response to Homer1a expression compared to neurons in vivo.

(b) Lentivirus-Based Expression System.

We have shown that - in contrast to the Sindbis virus - the Lentivirus expression system is well suited for stable long-term expression of FPs in small neuronal networks in the intact neocortex [48]. In addition, we have demonstrated in vivo time-lapse imaging of pre- and postsynaptic structures up to several hours. Our results support recent in vivo findings on the overall stability of dendritic spines in the adult cortex [69] [85]. Lentivirus-based expression of FPs in cortical and subcortical areas might be used to perform simultaneous imaging of pre- and postsynaptic components in vivo.

Furthermore, we have shown that virus-mediated siRNA expression via spatially confined and temporally defined stereotactic injection offers the possibility to genetically manipulate small neuronal populations in vivo. This possibility may allow one to investigate in vivo functions of genes that otherwise would be possible to study only by the use of

in vitro methods, especially when the corresponding transgenic approach is expected to result in a lethal phenotype or in activation of compensatory mechanisms.

Finally, we found that virus-mediated GECI expression is currently not well suited to report neuronal activity in the intact neocortex. While Inverse Pericam did not show any activity evoked Ca^{2+} transients even following strong stimulation, GCaMP showed moderate responses at high firing rates. Our findings on the low sensitivity of GECIs at low AP firing rates is supported by a recent, more detailed study by Pologruto et al. in vitro [151]. In their work, cultured hippocampal slices were transfected with three different GECIs (including Inverse Pericam and GCaMP) using particle-mediated biolistic gene transfer. Pologruto et al. found that all GECIs produced robust signals to high-frequency trains of APs but had poor sensitivity at low firing rates as compared with synthetic Ca^{2+} indicators with similar affinities for Ca^{2+}. In addition, all GECIs showed complex responses to trains of APs (including sublinear and supralinear regimes), had relatively less brightness compared with GFP, and showed dynamic ranges and Ca^{2+} sensitivities not optimal for measurements of activity in vitro. In contrast, an ideal neural activity sensor would be bright, respond linearly to a large range of stimuli (in terms of AP number and frequency) and would rapidly follow Ca^{2+} transients, allowing detection of individual APs. Although GECIs therefore are currently not well suited for functional imaging in vivo, their rapid advancement promises to offer targeted expression and long-term monitoring of neuronal activity in various cellular compartments in the near future, for example, to relate subcellular activity to structural changes [120]. Functional imaging of neuronal and glial population dynamics on a timescale of hours, however, is possible through multi-cell bolus loading of membrane-permeable calcium indicator dyes [138] [181], yet without genetic manipulation capabilities or synaptic level resolution.

4.2.2 Astrocytes

A robust stain of neocortical protoplasmic astrocytes in vivo was achieved through brief exposure of the intact brain to the red fluorescent dye sulforhodamine 101. The specificity of SR101 labeling for astroglia was verified by immunohistochemistry and by applying SR101 in transgenic mice that express EGFP in different glial cell types. We have used this staining method for a morphometric analysis of the distribution of neocortical astrocytes, for visualization of complete glial envelopment of cortical microvasculature, and for dissection of distinct calcium dynamics in astroglial and neuronal networks.

Specific uptake of SR101 by glial cells has been previously reported for rabbit retina [52], in which intravitreal application of SR101 caused specific, robust labeling of a subpopulation of cells that were identified as oligodendrocytes. In contrast, we did not find preferential uptake by neocortical oligodendrocytes, as confirmed by counter-immunostaining for CNPase. This difference indicates that the uptake of SR101 varies in different regions and needs to be assessed for each particular brain area. For example, we did not find SR101 uptake by Bergmann glia in cerebellum in vivo. A number of in vitro studies have reported activity-dependent SR101 uptake in presynaptic terminals [118] and neurons [98]. In both our in vivo and counter-immunostaining experiments, there was no indication of activity-

dependent uptake in neocortical neurons, although they are known to be spontaneously active [9] [150]. The very few, exceptional cases where SR101 stained additional cells other than protoplasmic astrocytes might represent uptake by macrophages or a specific subtype of oligodendrocytes.

The mechanism of SR101 uptake by astrocytes is not known. Although previous studies of activity-dependent uptake presumed that endocytosis is the predominant mechanism [118] [98], the efficacy and rapid time course of SR101 loading into neocortical astrocytes, together with the initial homogenous cytoplasmic staining, suggest that a specific transporter system acts as the uptake mechanism [52]. Furthermore, we found that SR101 spreads through gap junctions, consistent with the gap-junctional spread of other fluorescent dyes of similar size and charge [163]. So far, we have not observed any damaging effects of SR101 on astrocytes or other cortical cells, as indicated by normal cell morphologies after repeated SR101 applications and repeated imaging sessions (for several hours and up to 3 weeks) as well as by the unperturbed calcium signaling. The preserved morphology, however, does not exclude anatomical changes on the synaptic level [84].

Three findings indicate that SR101 selectively labels all protoplasmic astrocytes in the vicinity of the application site. First, cortical microvasculature was completely enveloped by end feet of SR101-labeled astrocytes. Second, gap junctions are involved in rapid spread of the dye. Third, distribution and densities of SR101-labeled cells in upper layers of cortex are in agreement with previous results in situ [207]. SR101 labeling thus might enable the study of changes in density and distribution of astrocytes in vivo, for instance in mouse models of neurodegenerative diseases [206]. In addition, colabeling of associated cortical elements, such as blood vessels and neurons, should enable studies of structural plasticity at the gliovascular and the neuron-glia interface, respectively. Counterstaining of blood plasma might be particularly useful when investigating the role of astrocytes in blood-brain barrier integrity [206]. Colabeling of neuronal structures, for example by combining SR101 application with viral infection [116] [102] or using transgenic mice [57], will make it possible to address the role of astrocytes at the synaptic level in vivo. In particular, simultaneous time-lapse imaging of astroglial processes with pre- and postsynaptic structures may help to elucidate their contribution to synapse formation at the tripartite synapse [198].

We also combined SR101 labeling with bulk loading of membrane-permeable calcium indicators [181], which enabled the simultaneous functional measurement of astroglial and neuronal network dynamics in the living animal. Accumulating evidence suggests that communication between astrocytes and neurons is bidirectional [60] [18]. In particular, astrocytes can release glutamate in a calcium-dependent manner [148] [132] and thus influence neuronal signaling pathways [60] [8] [202]. In vitro, astrocytic calcium signals have been found in the form of slow calcium elevations as well as calcium waves [32] [35] [27], which can propagate among astrocytes over long distances. The physiological relevance of these calcium oscillations [27] [149] and waves is, however, still unclear. Our results together with another study [83] provide first direct evidence that astrocytic calcium oscillations and waves do occur in vivo. The kinetics of these spontaneous signals was markedly different from those of the fast calcium transients observed in neurons, which were consistent with action potential-induced somatic calcium influx [205]. This methodological approach for

in vivo calcium imaging is thus well suited to correlate the activities in neuronal and astroglial networks and is expected to provide new insights into neuron-glia communication as well as into the role of astrocytes in activity-dependent regulation of cerebral blood flow [218] [172].

4.2.3 Microglia

Furthermore, we have demonstrated that microglial cells are highly dynamic structures during the 'resting' state in vivo, and not only after activation. For several reasons, we believe that continuous restructuring of microglial cells represents their natural behavior in the resting state and is not by itself a sign of activation. First, microglia branch motility was observed in the neocortex using a minimally invasive imaging approach more than 100 μm below the pial surface. In time-lapse recordings of up to several hours, microglia maintained their highly ramified morphology, with no signs of morphological transformation (e.g. thickening of proximal processes or decrease in ramification of distal branches). Second, the high degree of branch motility was specific to microglia, as astrocytes counterstained with SR101 showed no comparable restructuring of their processes. Third, microglial cells immediately switched their behavior after local activating stimuli.

The extent of ongoing structural changes far exceeds what has been described for both neurons [69] [190] and astrocytes [84] on a similar time scale. The pronounced and ongoing structural changes of resting microglial cells presumably serve an immune surveillance function. From our space filling analysis we estimate that microglial cells screen the entire brain parenchyma on a daily basis. Based on a mean microglia density of 6500 cells/mm^3 [114], a total mouse brain volume of 112 mm^3 [165], and a conservative assumption of an average branch turn over of about 600 μm per cell and hour, we calculate that about 10 kilometers of microglial processes are turned over every day in an adult mouse brain.

Microglia can sense subtle changes in their microenvironment through a variety of surface receptors, such as receptors for complement fragments, immunoglobulins, adhesion molecules, and inflammatory stimuli [155]. Microglia, in addition, are equipped with purino- and fractalkine-receptors as well as receptors for neurotransmitters [200], which allow them to detect changes in neuronal activity. A persistent increase in neuronal activity could serve as a first warning signal to microglia, indicating pathologic changes in brain metabolism. Our experiments show that volume surveillance is indeed enhanced by increased neuronal activity. Interestingly, we did not find a significant change in microglia surveillance behavior with reduced neuronal activity. This may indicate that microglia exhibit a baseline level of motility rather independent of neurotransmitter release, although we can not exclude a direct effect of TTX on microglia itself [33] [51]. Microglia, in addition, can respond to these changes, for example, through expression of neurotrophic factors or release of pro- and anti-inflammatory cytokines upon activation [200]. Our experiments suggest that microglia perform this surveillance function by continuously sampling their environment with highly motile protrusions. These protrusions may also be involved in collecting tissue debris. Microglia motility most likely is based on actin, a cytoskeletal protein shown to be critically involved in growth and motility in many cells. Indeed, microglia contain high levels of filamentous actin [26] and inhibitors of actin polymerization

have been shown to affect the motility and migration of activated microglial cells [140].

Activated microglia are thought to exert neuroprotective as well as neurotoxic functions on neurons. Overall this effect may depend on both pathologic conditions and the severity of the injury [200] [155]. In our microlesion experiments, the shielding of injured sites indicated a neuroprotective role for microglia. Furthermore, the early formation of spherical shaped inclusions suggests immediate phagocytic engulfment and removal of damaged tissue or leaked blood components. Together, this is consistent with the idea that microglia constitute the first line of defense against invading pathogens [200] [203]. In conjunction with animal models of brain disease, our in vivo imaging approach presents the opportunity to study the role of microglia in various pathologies in the intact brain.

Chapter 5

Summary & Publications

In conclusion, we have advanced miniaturized two-photon microscopy towards functional imaging of cellular networks in awake, behaving animals. The main achievements are summarized below:

1. Miniaturized two-photon microscopy is based on the use of optical fibers, providing flexible light guidance towards a head-mounted end piece [79]. A major problem with light guidance through standard single-mode fibers had been that propagation of near-infrared femtosecond pulses through these optical waveguides is associated with severe linear and nonlinear pulse broadening [81]. Efficient two-photon fluorescence excitation deep within cortical tissue, however, requires delivery of short light pulses at high power. Here, we demonstrated distortion-free delivery of near-infrared femtosecond light pulses to the output face of hollow-core photonic crystal fibers for pulse energies up to 4.6 nJ [65]. This effectively overcomes the problem of pulse broadening in single-fiber based miniature two-photon microscopes and allows efficient two-photon excitation at the fiber output face.

2. We successfully applied an improved single-fiber based miniature microscope to imaging of cellular networks in the intact rat neocortex [136]. In particular, we demonstrated multi-color fluorescence detection of differentially labeled cell populations in vivo and remote control over the microscope's field of view, enabling correction of image shifts (e.g. due to sudden animal movements).

3. We developed and applied an ultra-small and lightweight miniaturized two-photon microscope based on fluorescence excitation and detection through a flexible coherent fiber bundle in combination with a gradient-index lens objective [64]. Although inferior in resolution, the fiber-bundle microscope promises to permit flexible endoscopic imaging from deep within various tissues. Thus, in the future it may be useful for optical biopsy or for functional measurements from deep brain nuclei in behaving animals.

4. We developed two virus-based systems for targeted expression of fluorescent proteins in neocortical pyramidal neurons for the purpose of their anatomical and functional

fluorescent staining in vivo [102] [48]. We showed that a Sindbis virus-based expression system is well suited for rapid short-term labeling and investigation of dendritic structural plasticity in vivo. We demonstrated stable long-term labeling of pyramidal neurons using a Lentivirus expression system. In addition, we showed that Lentivirus-mediated expression of genetically encoded calcium indicators is currently not well suited for monitoring neuronal population dynamics in vivo.

5. We discovered a robust method to specifically label neocortical astroglia in vivo using the organic red fluorescent dye sulforhodamine 101 [138]. We applied this technique to characterize astroglial structure and function in the intact brain. In particular, we showed that astroglia in the adult brain display overall stable morphology. Furthermore, we demonstrated simultaneous calcium imaging of neuronal and glial networks in vivo, thereby revealing their distinct calcium dynamics. In addition, we provided first evidence that astroglial calcium waves and oscillations (phenomena thought to be important in astroglial signalling and communication) do exist in vivo.

6. We employed transgenic mice to characterize microglia behavior in the healthy brain and in response to local injury [137]. We showed that, in contrast to the prevailing view, microglial cells are highly dynamic structures continuously undergoing morphological changes. We provided first direct evidence, that they dynamically interact with other cortical elements, and that their structural dynamics serves a steady state immune surveillance function. Furthermore, our results on microglia response to local blood brain barrier disruption provide first insights into the immediate reaction of the primary brain immune effector cells to cerebral hemorrhage.

Taken together, this work presents important steps in the field of high-resolution two-photon imaging of neocortical networks in vivo. It has resulted in a number of publications and manuscripts listed on the following page:

Publications in Peer Reviewed Journals

1. Sullivan, M.R., Nimmerjahn, A., Sarkisov, D.V., Helmchen, F., Wang, S.S.-H. (2005) In vivo calcium imaging of circuit activity in cerebellar cortex. *J. Neurophysiol.* **Epub ahead of print**.

2. Nimmerjahn, A., Kirchhoff, F., Helmchen, F. (2005) Resting microglial cells are highly dynamic surveillants of brain parenchyma in vivo. *Science* **Epub ahead of print**.

3. Dittgen, T., Nimmerjahn, A., Komai, S., Licznerski, P., Waters, J., Margrie, T.W., Helmchen, F., Denk, W., Brecht, M. and Osten, P. (2004) Genetic manipulation of single cortical neurons and their optical and electrophysiological monitoring in vivo. *PNAS* **101** (52): 18206-18211.

4. Goebel, W., Kerr, J.N.D., Nimmerjahn, A., and Helmchen, F. (2004) A miniaturized two-photon microscope using a flexible coherent fiber bundle and a gradient-index lens objective. *Optics Letters* **29** (21): 2521-2523.

5. Nimmerjahn, A., Kirchhoff, F., Kerr, J.N.D., Helmchen, F. (2004) Sulforhodamine 101 as a specific marker of astroglia in the neocortex in vivo. *Nature Methods* **1** (1): 31-37.

6. Goebel, W., Nimmerjahn, A., and Helmchen, F. (2004) Distortion-free delivery of nanojoule femtosecond pulses from a Ti:sapphire laser through a hollow core photonic crystal fiber. *Optics Letters* **29** (11): 1285-1287.

7. Kim, J., Dittgen, T., Nimmerjahn, A., Waters, J., Pawlak, V., Helmchen, F., Schlesinger, S., Seeburg, P.H., Osten, P. (2004) Sindbis vector SINrep(nsP2S^{726}): a tool for rapid heterologous expression with attenuated cytotoxicity in neurons. *J. Neurosci. Methods* **133** (1-2): 81-90.

Manuscripts in Preparation

1. Nimmerjahn, A., Denk, W., Helmchen, F. Optical pulse compression using a pair of multi-prism arrays as compact low-loss dispersion compensation technique.

2. Nimmerjahn, A., Theer, P., Helmchen, F. Ultrashort Laser Pulses in Biology and Medicine: Two-photon laser scanning microscopy. (Eds. W. Zinth, M. Braun & P. Gilch) (Springer, Heidelberg).

Chapter 6

Future Perspectives

Based on the findings presented in this thesis, one can think of a multitude of future directions:

Functional imaging in behaving animals. Miniaturization of two-photon microscopy has enabled high-resolution imaging of blood vessels and single cortical neurons in freely moving animals [79]. However, functional imaging in freely moving rodents so far has not been achieved, one major obstacle being the lack of efficient fluorescence staining techniques.

In this thesis, we have shown efficient labeling and simultaneous functional imaging of astroglial and neuronal networks in the intact brain [138]. Furthermore, using our improved miniature two-photon microscope in combination with novel labeling techniques we have demonstrated in vivo imaging of astroglial and neuronal networks in cortical layers 1 and 2 [136]. Experiments in freely moving animals are under way, aiming to study the correlation between peripheral muscle activity (e.g. in the whisker muscle pad) and cellular activity in the corresponding cortical motor areas [16] [4]. Those high-resolution functional maps [143] may help to understand the precise micro-architecture in motor cortex, and in particular the potential role of glia in certain aspects of information processing.

Functional endoscopic two-photon imaging. The development of optical fiber-based two-photon endoscopes holds the promise to eventually yield diagnostic tools for biomedical research. In particular, such devices may find applications in optical biopsy, photodynamic therapy, microsurgery, and early cancer detection [19] [64].

We have shown, that our miniaturized two-photon microscope based on a flexible coherent fiber bundle and a GRIN lens objective permits imaging of cortical microvasculature in vivo. It provides an ultra-small and ultra-light (yet lower resolution) alternative to our hollow-core PCF miniature microscope.

In the future, further development of fiber-based microendoscopy may enable direct observation of hippocampal place cells during animal behavior. Those cells are

thought to be critically involved in spatial learning, i.e. in forming a cognitive map of the environment [90]. Alternatively, the use of a high-power laser system to concurrently feed a pair of microendoscopes may permit simultaneous high-resolution imaging from thalamic output and neocortical input regions.

Functional labeling of deep-seated cellular structures in these applications might be achieved through stereotactic injections of membrane permeable calcium indicator dyes or upcoming genetically encoded indicators [216] [196].

Investigation of viral impact or gene function in vivo. The Sindbis virus offers a convenient method for rapid heterologous protein expression in neurons in the intact brain. We have shown, that it can be used, for example, to investigate the structural plasticity of neocortical neurons in vivo. Following a 48 - 72 h expression period, however, progressive shut down of host cell protein synthesis leads to infection-associated cytotoxicity and eventually to apoptosis [102] [131]. Although this side effect may not be desirable in many applications, one can leverage this property of the Sindbis virus. For example, as an alphavirus of the Togaviridae family (which causes encephalitis in mice) the Sindbis virus might serve as a model to study the demeanor of closely related human encephalitic viruses in vivo. In particular, Sindbis virus infection of CX_3CR1-EGFP mice [93] may serve as a model to study infection-related mechanisms of immune defense.

In contrast, Lentiviral vectors have been proposed as a promising tool for gene therapy, potentially opening new perspectives for genetic treatment of a wide array of hereditary as well as acquired disorders [192].

Generally, genetic manipulation using localized viral infections offers several unique advantages over current transgenic/knockout technologies. First, stereotactic injection makes it easy to control the delivery of recombinant genetic material to a discreet region and to produce expression in a defined time window. Second, the fact that only a small number of neurons (or other cells, depending on the promoter) in the intact brain will be altered obviates problems associated with entire brain or whole-brain subregions being affected (e.g. a lethal phenotype or activation of compensatory mechanisms). Therefore, in vivo functions of genes might be studied in ways otherwise impossible by the use of in vitro methods.

In this thesis, we have demonstrated that our approach can be used for efficient gene expression or knockdown in a small population of cortical neurons. Thus, in the future, combination of the lentivirus-based genetic manipulations with high-resolution two-photon time-lapse imaging or TPTP might be used to study the function of specific gene products in a small population of neurons in vivo, either during early postnatal development or in the adult.

Imaging of astrocyte function in vivo. Astrocytes are key players in a metabolic network between neurons, glia and vascular cells that sustains brain activity. They are

thought to be involved in blood flow regulation, water homeostasis, and metabolic trafficking [172] [173]. In particular, they extend specialized end foot processes to perivascular and perineuronal regions, which allow them to mediate bidirectional flow of metabolic, ionic, and other transmissive substances between neurons and the blood stream [214].

Little is known, however, about the functional signals that underly such regulatory processes. Calcium has been identified as an important mediator of functional signals. In particular, calcium signaling has been shown to underly bidirectional communication among astrocytes and with neighboring neurons [18] [133]. Astroglial calcium signaling, in addition, is proposed to be involved in regulation of cerebrovascular tone [127] [218]. Most studies on neuron-glia and glia-vascular communication, however, have been carried out in vitro. Hence, the significance and spatiotemporal dynamics of calcium signaling in vivo remains unclear.

In this thesis, we have presented a method for simultaneous imaging of astroglial and neuronal calcium signaling in vivo. We are able to resolve calcium transients in astroglial end foot processes (data not shown), as well as single action potentials in neurons [99]. Thus, investigation of functional calcium signals that may underly homeostatic regulation processes in vivo is entirely feasible. In particular, monitoring alteration of such signaling in appropriate animal models of disease may help to better understand the role of astrocytes in brain pathology [11] [134].

Imaging of microglia behavior in animal models of disease. Microglial cells represent the endogenous immune system of the brain [182]. As such, they are critically involved in all major brain pathologies, including viral infections (e.g. HIV), lesions, stroke and neurodegenerative diseases [109] [155].

In this thesis, we have presented an in vivo imaging approach that allows for the minimally-invasive study of microglia in the intact brain, and in particular under pathological conditions. Our micro-lesion experiments (which present a new model for hypertension-induced stroke), for example, have revealed first insights into the immediate reaction of microglia to local cerebral hemorrhage. Importantly, our imaging approach can be easily transferred to other animal models of disease. Double-transgenic mouse lines over-expressing mutant human amyloid precursor protein (APP) and EGFP in microglia, for example, might enable to investigate the role of microglia in Alzheimers disease [183] [30]. Brain implanted GRIN lenses [92] [117] may serve as a new model for brain lesions, potentially allowing to study microglia-mediated repair processes over the course of several days to weeks in vivo.

Chapter 7

Materials & Methods

This chapter provides detailed information on all methodological aspects of the thesis. In particular, section 7.1 presents details on miniature microscope design, while section 7.2 gives an overview of the materials and methods used for in vivo fluorescence labeling. Staining technique evaluation and applications was performed on a standard two-photon microscope setup. The operability of the fiber-based microscopes was evaluated in anaesthetized animals. All animal experimental procedures were carried out according to the animal welfare guidelines of the Max-Planck-Society.

7.1 Fiber-Based Two-Photon Microscopes

7.1.1 Single Fiber Based Two-Photon Microscope

Animals and Surgical Preparation. Six Wistar rats (P21 - 28) were used for experiments. Animals were anesthetized with an intraperitoneal injection of either ketamine (100 mg/kg)/xylazine (10 mg/kg) or urethane (1.6 - 2 g/kg body weight). For details on surgical preparation, see section 7.2.2.

Labeling Procedures. Fluorescence labeling was performed as described in subsection 7.2.2.

Mechanical and Optical Fiber Microscope Design. The fiber microscope setup (using a single optical fiber for fluorescence excitation) comprised three modules (see Fig. 3.1). Modules one and three were stationary and included all bulky components concerned with fluorescence excitation and detection, respectively.

Fixed components in module one comprised a Ti:Sapphire laser (Mira 900-F and Verdi-10 pump laser; Coherent), providing ultrashort laser pulses (pulse width ∼100 fs) at a center wavelength between 790 - 850 nm (for evaluation of the PCF; for application of the miniature microscope the laser was set to the optimal of ∼812 nm to prevent pulse broadening), a galvo-scanner mounted crystalline quartz plate based on the principle of Berek's compensator for laser intensity control [39], concave mirrors for beam size

adjustment (Linos), a quarter waveplate (ThorLabs) to reduce back-reflections into the laser, and a fiber coupler equipped with an aspheric lens (f = 18.4 mm; NA 0.15; Geltech). Module three contained all parts needed for two-channel fluorescence detection, i.e. a lens (f = 27 mm; Linos) collimating light that emerges from the fluorescence collection fiber, a 570 nm dichroic mirror to separate 'red' (longer wavelength) from 'green' (shorter wavelength) fluorescent light, and two photomultiplier tubes (R6357, Hamamatsu). In addition, the 'green' and 'red' detection channel employed a BG39-colored glass filter and a 610/75 bandpass filter, respectively. Finally, module two comprised all parts of the miniature head-mounted microscope. In particular, it included a small resonant fiber scanner (see below), a small silver coated mirror (6 mm diameter; 1 mm thickness; R > 99%; Linos) mounted on a tilting stage (see subsection 3.1.1), and an aspheric lens (f = 18.4 mm; NA 0.15; Geltech) for excitation light collimation. Furthermore, a miniature objective (1 mm focal length; NA 0.9; 1.1 g; Manfred Throl Optical Systems), a 570 nm dichroic mirror (10×10 mm^2) for separation of fluorescence and excitation light, and a second aspheric lens (f = 4.5 mm; NA 0.55; Geltech) for fluorescence light coupling into the fluorescence collection fiber. All optical components were set up on a small aluminium baseplate ($5.5 \times 3.0 \times 1.8$ cm^3) using custom-made aluminium or plastic holders. A small DC motor (3 mm 'smoovy' gearmotor; gear ratio 1:125; RMB Miniature Bearings), attached to the second aspheric lens holder and connected to the objective holder through a threaded rod, enabled remote focusing. Axial movement of the objective was ensured by means of a vertical rail in which the objective holder could slide.

Modules one and two were interconnected via a hollow-core photonic crystal fiber (HC-800-01; BlazePhotonics), while modules two and three were linked together using a flexible multi-mode large-core optical plastic fiber (M02-534, Edmund Industrie Optik GmbH) for fluorescence collection. A precision angle-cleaver (8° cutting angle; AFC-2008; Oxford Fiber Ltd.) was used to cut the hollow-core PCF endings after removing the fiber coating with a fiber stripper (Thorlabs). Fibers endings of the large core fiber were polished using 3, 1, and 0.3 μm lapping film (ThorLabs).

Resonant Fiber Scanning. A small resonant fiber scanner was constructed as previously described [79]. Briefly, the distal hollow-core PCF fiber end (with the protective fiber jacket removed) was glued to a piezoelectric element leaving a short end (1 - 2 cm) free to vibrate. Flexural vibrations of the freestanding fiber end were induced by driving the piezoelectric element at the fiber end's vibrational resonance frequency. For a 125 μm (standard-)diameter fiber, resonance frequencies f_{res} were in the range between 300 Hz and 500 Hz. In general, for transverse vibration of a cylindrical rod, f_{res} is given by [20]

$$f_{\text{res}} = \frac{s_0^2}{4\pi} \frac{R}{L^2} \sqrt{\frac{E}{\rho}} \tag{7.1}$$

where R is the radius, L the length of the rod, ρ the density ($\sim$2.3 g/cm^3), E the elasticity module of the fiber ($\sim$75 GPa), and $s_0 = 1.875$. Thus, f_{res} depends inversely on the square of the length L.

Two-dimensional scanning was achieved by stiffening the fiber tip in one direction with a short piece of bare fiber (2 - 4 mm) glued to the lower edge of the piezo and to the fiber at about 2 - 3 mm distance from the piezo. This results in two resonance frequencies of the fiber tip, which can be determined by driving the piezo with a sinusoidal waveform that is swept in frequency. Because the resonance widths are typically only 5 - 10 Hz, it was necessary to sweep the frequency slowly and finely so as not to miss the resonance. Near resonance and peak-to-peak drive amplitudes up to 100 V, fiber deflections up to a millimeter (peak-to-peak amplitude) were achieved.

For accurate measurement of the resonance curve, the fiber tip was imaged onto a 2D position-sensitive detector. This approach also permitted a direct measurement of the scan pattern in the form of a Lissajous figure [119]. Such pattern is excited when the piezo is driven with a superposition of the two sine waves with the resonance frequencies for the orthogonal directions. The main features of this scan pattern (area coverage, resolution, and repeat frequency) are determined by the ratio of the two chosen frequencies f_x, f_y. Our goal was to obtain a self-repeating scan pattern with high area coverage. Though not absolutely necessary, this choice of a stable pattern repeating itself with a certain frequency is convenient for image reconstruction purposes. A repetitive pattern is obtained if this ratio is a rational number, i.e. if $f_x/n_x = f_y/n_y = f_R$, where n_x and n_y are the smallest possible integers with the ratio n_x/n_y equal to f_x/f_y. f_R is the pattern repeat frequency. The numbers n_x and n_y roughly determine the resolution of the pattern (i.e. the density of the intersections of the trajectory). Based on these considerations, we first selected frequencies as close as possible to the peak of the resonances to ensure that the lateral vibration modes were nearly orthogonal. Second, the frequency ratio was adjusted so that a repeat frequency of about 2 Hz resulted. This frequency provides sufficient spatial resolution and enables online image reconstruction and display. For frequencies in the range of 300 - 800 Hz, n_x and n_y therefore were in the range of 150 - 400. Thus, all pixels were sampled at least once during a 0.5 s frame with a pixel resolution of either 64×64 or 128×128 used for image reconstruction.

Although the motion of the fiber tip is completely determined by the voltage driving the piezoelectric element (which is a superposition of the x and y signal), the drive signals do not directly represent the position of the fiber tip because, particularly near resonance, a strong phase shift exists between driving force and response. Nevertheless, we could reconstruct the tip position precisely from the x and y drive signals after correcting for that phase difference. Phase shifts were determined by directly measuring the scan pattern with a two-dimensional position-sensitive detector before an experiment. In addition, phases were fine tuned during the experiment by minimizing double and quadruple images, which result from errors in phase settings. The fluorescence intensities measured by the stationary PMTs were then assigned to the corresponding pixels in order to form an image.

In addition to full-frame scans, measurements at high temporal resolution were feasible through implementation of a line scan mode in which the piezoelectric element is excited with only one of the two resonance frequencies. This results in motion of the fiber tip along only one direction and in principle allows an increase of time resolution up to one half of the oscillation period ($\sim$1 - 2 ms in our case). To get sufficient signal, however, fluorescence intensities generally have to be averaged over a few oscillation

periods, resulting in an effective time resolution of ∼10 ms [79].

Fiber Microscope Control and Image Acquisition. Two digital frequency generators (model DS345; Stanford Research Systems) provided sinusoidal voltages at the chosen frequencies f_x, f_y. The electronic superposition of these signals was the input to a high-voltage amplifier (0 - 50 V; Burleigh) driving the piezoelectric bending element. At the same time, the output signals of the frequency generators were fed through custom-built electronics that mimicked the mechanical response of the fiber. This circuit permitted us to independently shift the x and y signal in their phase and, in addition, to eliminate some residual cross-talk between the x and y direction (<5% amplitude). The output signals of this circuit were then used as accurate reference signals for the actual position of the fiber tip. Amplitude and phase settings were adjusted by comparing the generated reference signals with the actual scan pattern, which was directly measured with a position-sensitive detector (ON-TRAK Photonics). In addition, even small errors in phase setting became apparent during the experiment as doubling of edge structures in the reconstructed images and could be corrected for empirically.

For image reconstruction, the PMT current signals were preamplified (DLPCA-200, Femto) and digitized together with the x and y reference signals at 100 kHz/channel (MIO-16E-1 board; National Instruments). The PMT intensity values were assigned to the pixel corresponding to the x and y readout (the total number of pixels was chosen beforehand; typically we used 64 × 64 or 128 × 128 arrays). This assignment was performed online using custom-written software in LabView (National Instruments). In a Lissajous scan pattern, individual pixels are not sampled with the same frequency (in particular, pixels near the image edges are hit more often). To adjust for this uneven scan density and in order not to waste information, a second array was held in the background in which the number of hits was stored for each pixel. The final image for one exposure time then contained the average intensity value for each pixel. The same strategy was applied in line scan mode.

Two-Photon Imaging. The miniature microscope was attached to a focusing unit (Nikon) fixed to an x-y-translation table to allow three-dimensional positioning of the headpiece with respect to the animal's head. All experiments were performed in complete darkness.

7.1.2 Coherent Fiber Bundle Two-Photon Microscope

Animals and Surgical Preparation. Wistar rats (P21 - 28) were used for experiments. Animals were anesthetized with an intraperitoneal injection of urethane (1.6 - 2 g/kg body weight). For details on surgical preparation, see section 7.2.2.

Labeling Procedures. Fluorescence labeling was performed as described in subsection 7.2.2.

Mechanical and Optical Fiber Bundle Microscope Design. The miniaturized two-photon fiber bundle microscope was constructed based on a flexible coherent fiber bundle and a gradient-index lens objective. The coherent fiber bundle (IGN-08/30; Sumitomo Electric Industries) comprised 30,000 individual fibers (core diameter: 2.4 μm; core distance: 4 μm; NA of 0.35) fused together to yield an image area of 0.8 mm diameter. At the distal end of the fiber bundle (i.e. close to the specimen) a GRIN lens objective system was attached to image the fiber bundle end face onto the sample. The GRIN lens objective was composed of two different gradient index rod lenses, both with a diameter of 1.0 mm. In particular, the imaging lens (collimating the light emerging from the single fibers) had a pitch of 0.25 and a NA of 0.2 (GT-LFRL-100-25-20-NC; GRINTECH), while the objective lens (refocusing the light at a working distance of 300 μm in the object plane) had a pitch of 0.20 and a NA of 0.5. The lenses were glued to each other using UV curing adhesive (Norland) and an UV-curing-lamp (Thorlabs). For proper lens alignment a custom-made alignment tool was employed, consisting of a cubic Teflon piece with two straight cuts (diameter: 0.5 mm and 0.9 mm). A custom-made plexiglass clamp was used to connect the GRIN lens system to the fiber bundle.

Two-Photon Imaging. The fiber bundle was fixated under the objective (10×/0.25 air objective; ZEISS Achrostigmat) of our custom-made two-photon laser-scanning microscope using a special holder. Femtosecond laser pulses from a Ti:sapphire laser system (Coherent; 76 MHz repetition rate; ∼880 nm center wavelength; ∼100 fs initial pulse length) were coupled into individual fibers of the fiber bundle after double passing a pair of diffraction gratings (400 grooves/mm; 9.7° blaze angle; Richardson Grating Laboratory) for dispersion compensation. A Pockel's cell (Conoptics) and telescope lenses (Linos) were used for intensity control and beam size adjustment, respectively. Backreflections towards the laser were averted using a wavelength tunable optical isolator (Linos).

Fluorescent light was collected through the GRIN lens objective system and the fiber bundle. At the proximal end of the fiber bundle (i.e. distal to the specimen), a dichroic beamsplitter was used to separate excitation from fluorescent light. Fluorescent light was detected by a photomultiplier tube (R6357; Hamamatsu).

7.2 In Vivo Fluorescence Labeling and Two-Photon Imaging

7.2.1 Neurons

(a) Sindbis Virus-Based Expression System.

Animals. Wildtype rats (Wistar; P19 - 24) were used for experiments.

Viral Constructs. In this study, we used three viral constructs: SINrep(nsP2S^{726})2SP-EGFP, SINrep(nsP2S^{726})2SP-^{Myc}Homer1a+EGFP, and SINrep(nsP2S^{726})2SP-^{Myc}Homer1a(W24A)+EGFP. All Sindbis virus constructs were ob-

tained from Pavel Osten (Department Molecular Neurobiology, Max-Planck-Institute for Medical Research, Heidelberg, Germany). For details on Sindbis viral vector production and in vitro evaluation see [102].

In Vivo Infection of Cortical Neurons. For viral infection, rats were anaesthetized with an intraperitoneal injection of a fully antagonisable anaesthetic (150 μg/kg metetomidin, 6 mg/kg midazolam, 3.75 μg/kg fentanyl) and transferred to an ultra precise small animal stereotaxic apparatus. Animal temperature was monitored with a rectal probe and maintained at 36 - 37°C using a heating blanket (Watlow). Depth of anesthesia was assessed by monitoring pinch withdrawal, eyelid reflex, corneal reflex, respiration rate and vibrissae movements. Glass pipettes (Blaubrand intraMARK) were pulled on a Sutter puller (model P-97) and the tips were broken to an outer diameter of 27 - 40 μm. The skull of the rat was exposed and cleaned. One to three holes (approximately 700 μm in diameter) were drilled in the skull above somatosensory cortex. The remaining skull was nicked using a 30 gauge injection needle tip for pipette insertion. The pipette tip was filled by suction with several hundred nanoliters of virus-containing solution, inserted into the brain at a shallow (about 45 degrees) angle, and lowered to a depth of approximately 350 and 500 μm below the pia mater. 29 - 48 nl of solution were delivered by pressure ejection (approximately 5 - 8 nl/s). 20 - 30 s after each injection the pipette was slowly retracted. Subsequent to suturing the skin and subcutaneous administration of anesthesia antagonists (750 μg/kg atipamezol, 600 μg/kg flumazenil, 90 μg/kg naloxon) animals were returned to their cages and allowed to recover.

In Vivo Two-Photon Imaging. For two-photon imaging 24 - 36 h after infection, animals were re-anaesthetized using urethane (2 g/kg body weight). A metal plate was attached to the skull with dental acrylic cement as described [103]. The center hole of the base plate was positioned above the injection site. A small craniotomy (2 - 3 mm diameter) was opened above this area and the dura was carefully removed. During this procedure, the exposed cortex was superfused with warm Hepes buffered normal rat Ringer solution (NRR: 135mM NaCl, 5.4mM KCl, 5mM HEPES, 1.8mM $CaCl_2$, and 1mM $MgCl_2$, pH 7.2 with NaOH). To dampen heartbeat- and breathing-induced brain motion, the craniotomy was filled with agarose (1.5%, type III-A, Sigma) in NRR and covered with an immobilized coverslip. In vivo images of infected neurons expressing EGFP were acquired with a custom-built 2-photon laser scanning microscope equipped with a 40× water-immersion objective lens (0.8 NA; Zeiss) using custom-written software (R. Stepnoski and M. Müller, Lucent Technologies, New Jersey and MPImF, Heidelberg). To minimize photodamage the excitation laser intensity was kept at a minimum for a sufficient signal-to-noise ratio. No apparent changes in dendritic morphology resulted from laser illumination during time-lapse recordings (stacks of 10 - 32 images; 30 - 70 s stack interval; 0.5 - 1.0 μm z-spacing; 10 - 80 min, total acquisition time).

Time-lapse imaging was performed in 5 animals for each Sindbis virus construct. We focused on dendritic branches in cortical layer 1 with imaging depth ranging from 30 to 230 μm below the pial surface. Time-lapse recordings typically lasted for about 1 hour (range 20 - 80 min). Small image stacks (10 - 30 focal planes at 0.5 - 1 micron increments)

were acquired approximately once per minute (interval range 30 - 70 s). Minimal intensity levels were used for the excitation light to avoid light-induced cell impairment.

Analysis of In Vivo Data. Image and movie analysis was done using NIH Image. For every image stack a maximum-intensity projection was created in z-direction. To determine spine densities and average spine length, maximum-intensity projections from time-lapse recordings or single image stacks were analyzed for EGFP, ^{Myc}Homer1a-EGFP, and ^{Myc}Homer1a(W24A)-EGFP labeled branches. For density measurements, spiny protrusions in both lateral and axial dimensions were counted. Since the axial resolution was relatively poor we can not exclude that some small protrusions were missed along this direction. The lengths of laterally projecting spines (defined as tip-to-base distance) were measured from maximum-intensity projections, which might result in slight underestimates. Analysis of dynamic length changes of dendritic protrusions was performed on time series of maximum-intensity projections of the individual image stacks. Projections were laterally aligned with a custom-written algorithm based on cross-correlation between subsequent images.

(b) Lentivirus-Based Expression System.

Animals. Wistar rats (aged P8 - P28) or C57BL6 or NMR1 mice (P10 to P61) were used for experiments.

Viral Constructs. In this study, we used four Lentiviral constructs: FCK(1.3)GW, FSy(1.1)GW, FCK(1.3)InvPW and FCK(1.3)GCaMPW. All Lentiviral constructs were obtained from Pavel Osten (Department Molecular Neurobiology, Max-Planck-Institute for Medical Research, Heidelberg, Germany). For details on Lentiviral vector production and in vitro evaluation see [48].

In Vivo Infection of Cortical Neurons. Lentiviral infection was performed as described above. Briefly, animals were anesthetized with an i.p. injection of ketamine (100 mg/kg)/xylazine (10 mg/kg), in some cases, with addition of atropine (0.02 mg/kg). Animals were kept deeply anesthetized as assessed by monitoring pinch withdrawal, eyelid reflex, corneal reflex, respiration rate, and vibrissae movements. Body temperature was maintained at 37°C by using a heating blanket (Watlow). One to three craniotomies, ∼300 - 400 μm in diameter, were drilled above the somatosensory cortex. Viral stock, ∼30 nl, was slowly injected, by using an ultraprecise small animal stereotaxic apparatus (Kopf Instruments, Tujunga, CA) at target depths of 300 - 500 μm below the pia mater with pulled glass pipettes (Blaubrand intraMARK, tips broken to an outer diameter of ∼30 μm).

In Vivo Two-Photon Imaging. Four to eight days after infection, animals were anesthetized with urethane (2 g/kg of body weight). A metal plate was attached to the skull with dental acrylic cement as described [103], and a large craniotomy (1.5 - 3 mm diameter) was opened. The dura was removed to improve optical access in rats (this procedure was not necessary in mice). To dampen heartbeat/breathing-induced brain

motion, the craniotomy was filled with agarose (1.5%, type III-A, Sigma) in normal rat Ringer and covered with a coverslip. In vivo images were acquired with a custom-built two-photon laser-scanning microscope with a 40× water-immersion objective lens (0.8 numerical aperture, Zeiss), by using custom-written software (R. Stepnoski, Lucent Technologies, Murray Hill, NJ, and M. Müller, Max Planck Institute for Medical Research, Heidelberg). No apparent changes in morphology resulted from laser illumination during time-lapse recordings (stacks of 10 - 34 images, 45 - 300 s stack interval, 0.5 - 1.5 μm z spacing, and 20 - 350 min total acquisition time). For an overview fluorescence image stack, a maximum-intensity side projection was created in the z direction. Consecutive projection images of time-lapse recordings were aligned based on the position shift of the crosscorrelation peak by using custom-written macros in NIH Image.

In Vivo Two-Photon Targeted-Patch Recording. Ten to 25 days after viral delivery of GECIs, a craniotomy was prepared as for in vivo two-photon imaging (see above). Patch pipettes were fabricated using filamented borosilicate glass (OD at 2.0 mm, ID at 1.5 mm; Hilgenberg GmbH, Germany). Patch recordings were obtained using pipettes with 4 - 6 MΩ tip resistance. Recording pipettes were filled with an intracellular solution containing 135 mM K gluconate, 4 mM KCl, 10 mM HEPES, 10 mM Na_2-phosphocreatine, 4 mM Mg-ATP, and 0.3 Na-GTP (pH 7.2). For pipette visualization, 50 μM Alexa Fluor 594 (Molecular Probes) was included in the pipette. Two-photon targeted-patch recordings were achieved similar to Margrie et al. [122]. Briefly, positive pressure (100 - 300 mbar) was applied to the pipette as it was inserted through the agar and the pial surface of the cortex. The positive pressure was reduced to 25 - 30 mbar when the tip was ∼20 μm below the pia. The pipette was then advanced under visual control to target individual EGFP labeled somata in L2/3. Voltage pulses were applied to the pipette (10 - 20 mV, 30 ms, 10 Hz), and the current response was monitored. Positive pressure was relieved when the series resistance of the electrode abruptly increased immediately after a 2 μm step, indicating that the tip of the pipette may have been pushed against a neuronal plasma membrane. Gentle suction (up to 100 mbar) was applied where necessary to obtain a gigaohm seal. Initial access resistances were typically 30 - 60 MΩ at the soma. All recordings were obtained using an Axoclamp-2B amplifier (Axon Instruments).

Extracellular Electrical Stimulation. Extracellular stimulation was performed using a coated tungsten electrode (part number TM31A10KT; shaft diameter, 216 μm; tip diameter, 1 μm; impedance, ∼1 MΩ; Parylene-C coating; WPI, Sarasota, FL). The stimulation electrode was mounted on a manipulator, inserted under the glass coverslip, and pushed through the agar and into layer 1. These electrodes are fluorescent, which allowed us to place the tip of the electrode 50 - 100 μm below the pial surface under visual guidance. Stimulus strength was adjusted to be just sufficient to evoke single to few APs (1 ms pulses; intensity range, 0.01 - 3 mA).

Data Analysis. Image stacks and time series were analyzed using NIH Image and ImageJ software. Analysis of dynamic length changes of axons and the rate of

photobleaching was performed on time series of maximum-intensity projections of the individual image stacks. If necessary, focal drifts were manually corrected before calculating the maximum intensity projections. Lateral drifts were corrected using a custom-written alignment routine based on the position shift of the cross-correlation peak of successive projection images.

7.2.2 Astrocytes

Animals and Surgical Preparation. Rats (P13 - 28; Wistar) and mice (P32 - 272; C57Bl6 wildtype or transgenic mouse lines with various genetic backgrounds) were used for experiments. Transgenic animals used in this study included mice expressing EGFP under control of human GFAP promoter [139] as well as CX_3CR1 mice expressing EGFP in microglia [93].

Animals were anesthetized with an intraperitoneal injection of either ketamine (100 mg/kg)/xylazine (10 mg/kg) or urethane (1.6 - 2 g/kg body weight). Animal temperature was monitored with a rectal probe and maintained at 36 - 37°C using a heating blanket (Watlow). Depth of anesthesia was assessed by monitoring pinch withdrawal, eyelid reflex, corneal reflex, respiration rate and vibrissae movements. The animal skull was exposed and cleaned. For short-term experiments (several hours), a metal plate was attached to the skull with dental acrylic cement as described [103]. A craniotomy (approximately 1 - 2 mm in diameter) was opened above somatosensory cortex (between -1 to -3 mm post bregma and 3 to 6 mm lateral; in some cases also above cerebellum). In rats, the dura mater was carefully removed in the majority of cases. During this procedure, the exposed cortex was superfused with warm HEPES buffered normal rat Ringer solution (NRR: 135 mM NaCl, 5.4 mM KCl, 5 mM HEPES, 1.8 mM CaCl2, pH 7.2 with NaOH). To dampen heartbeat- and breathing-induced brain motion, the craniotomy was filled with agarose (1.5%, type III-A, Sigma) in NRR and covered with an immobilized coverslip.

For long-term experiments (days to weeks), a small plastic head plate was permanently attached to the skull using dental acrylic. The head plate served as an adaptor for a metallic apparatus fixing the head in the same position at every imaging session. A craniotomy was made at the center region of the plastic head plate as described. An optical chamber was constructed by covering the craniotomy with agarose and a cover glass (Menzel, CB00070RA1), and sealing it with dental acrylic at the cover glass edge. This optical chamber was renewed before every imaging session where SR101 was applied. Animals were returned to their cages to recover in-between imaging sessions.

In Vivo Two-Photon Imaging. Two-photon imaging in intact neocortex was performed using a custom-built two-photon laser scanning microscope equipped with two fluorescence detection channels. Laser wavelength varied in the range between 840 and 890 nm (laser system Mira 900-F and Verdi-10 pump laser; Coherent). Fluorescence light was collected in the epifluorescence configuration. The 'red' (longer wavelength) fluorescence from SR101 was separated from the 'green' (shorter wavelength) fluorescence using a 570 nm dichroic mirror and detected simultaneously by two photomultiplier tubes (R6357,

Hamamatsu). Reflected excitation light in the 'green' and 'red' pathways was eliminated using a BG39-colored glass filter and a 610/75 bandpass filter, respectively. To minimize photodamage the excitation laser intensity was kept at a minimum for a sufficient signal-to-noise ratio.

Labeled cells could be imaged down to 700 μm below the pia. Subsequent image stacks of time-lapse recordings were corrected for focal drift. PMT settings and excitation power were kept constant during time-lapse imaging. Movement artifacts associated with the animal's heartbeat were overcome by triggering image acquisition from the animal's heartbeat.

Labeling Procedures. All labeling procedures were performed during anesthesia and during head fixation.

For in vivo labeling of cortical astrocytes, SR101 (Molecular Probes or Sigma) was dissolved in extracellular saline and briefly (1 - 5 min) applied either directly to exposed neocortical surface or on top of the craniotomy filled with 1.5% agar. In a few experiments SR101 was locally pressure-ejected from a micropipette. Typical concentrations used were in the range of 25 - 100 μM. Following surface application, the craniotomy was rinsed repeatedly using pre-warmed extracellular saline.

For the counter-immunostaining experiments, 100 - 500 μM Texas Red-hydrazide (Molecular Probes), a paraformaldehyde-fixable analog of SR101, was applied to the cortical surface in vivo as described above. After rinsing, the dye was allowed to be taken up by cortical astrocytes for 50 - 70 min before transcardial perfusion.

Multi-cell bolus loading of layer 2/3 cells with calcium indicator was performed as described in Stosiek et al. [181]. Briefly, Oregon Green 488 BAPTA-1 AM (Molecular Probes) was dissolved in DMSO plus 20% Pluronic F-127 and then diluted with normal rat Ringer solution (NRR: 135 mM NaCl, 5.4 mM KCl, 5 mM HEPES, 1.8 mM $CaCl_2$, pH 7.2 with NaOH) to a final concentration of 0.5 - 1 mM. This dye was then ejected via a micropipette using a short pressure pulse (1 min, 0.3 - 0.7 bar). This resulted in temporally stable, but unspecific labeling of cells (neurons and glial cells) with calcium indicator within approximately 300 μm around the injection site.

Blood plasma was stained via tail vein injection [103] of FITC-labeled dextran (77 kDa, 5% w/v in NRR, 0.1 - 0.2 ml; Sigma).

Tissue Fixation and Immunostaining. Animals were transcardially perfused with 4% paraformaldehyde in phosphate buffer solution. Brains were kept in fixative for 1 - 2 days. 60 μm thick coronal brain vibratome (Campden) sections were immunostained for S-100β protein and CNPase enzyme as described [67]. Briefly, slices were permeabilized (0.4% Triton X-100/PBS) for 30 min, blocked for 30 min in 4% horse serum (HS) with 0.2% Triton X-100 in PBS and incubated overnight at 4°C in 1% HS and 0.05 - 0.5% Triton X-100 in PBS with the primary antibody (anti-S-100β, rabbit polyclonal, 1:5000; Swant; anti-CNPase, mouse monoclonal, 1:300; Sigma). After two washing steps (PBS) slices were incubated with a Pacific Blue-conjugated secondary antibody (1:1000; Molecular Probes) in 1.5% HS in PBS for two hours, washed again and mounted using Moviol.

For immunostaining of the neuron-specific protein NeuN slices were treated with

5% normal goat serum (NGS) and 1% Triton X-100 in PBS for 60 min, incubated overnight at 4°C in 1% NGS and 0.3% Triton X-100 in PBS with anti-NeuN (mouse monoclonal, 1:1000; Chemicon). After three washing steps slices were incubated with a FITC-conjugated secondary antibody (1:200; Dianova) in 1% NGS and 0.3% Triton X-100 in PBS for two hours. The Texas Red-hydrazide and counter-immunostain were simultaneously visualized using a custom-built two-photon laser scanning microscope (870 - 920 nm excitation wavelength) and could be well separated in the two fluorescence detection channels.

Data Analysis. Maximum intensity projections and analysis of astrocyte distribution were performed on image stacks using custom-written macros in NIH Image. Volume densities were evaluated by counting cells within layer 1 or layer 2/3 and dividing by the analysis volume (at least $0.1 \times 0.1 \times 0.1$ mm^3). Radial density was analyzed by calculating the distances r between all labeled cells within a volume of 0.3 mm side length, calculating the histogram (bin width 3 μm), and then dividing the histogram by $4\pi r^2$.

Calcium transients were measured using 64 $\times$ 128 pixel scans with 1 ms line scan duration (15 Hz frame rate). Fluorescence was averaged over cell body areas and expressed as relative fluorescence changes ($\Delta F/F$) after subtraction of background fluorescence from a neighboring region. All data are presented as mean $\pm$ SEM.

7.2.3 Microglia

Animals and Surgical Preparation. Transgenic CX_3CR1 mice [93] (1.5 to 15 months old) generally were anesthetized with an intraperitoneal injection of ketamine (100 mg/kg body weight)/xylazine (10 mg/kg). Experiments used for morphometric analysis of microglial density and distribution were done under urethane anesthesia (1.6 - 2 g/kg). Isoflurane (1.5 - 2.5%; mixed with 0.6 to 0.8 litres/min O_2) was employed in most experiments that used surface application of pharmacological agents (BCC or TTX). Microglial motility was similar under the different types of anesthesia. Animal temperature was monitored with a rectal probe and maintained at 36 - 37°C using a heating blanket. Depth of anesthesia was assessed by monitoring pinch withdrawal, eyelid reflex, corneal reflex, respiration rate and vibrissae movements. The animal skull was exposed above somatosensory cortex (between -0.5 to -1.5 mm post bregma and 1.0 to 3.5 mm lateral) and cleaned. A metal plate was attached to the skull with dental acrylic cement as described [103]. In most experiments a thinned-skull preparation was used [30] [69]. A 1 mm diameter region above somatosensory cortex was carefully thinned to 20 - 40 μm thickness using a high-speed drill and scraping the cranial surface with a micro-surgical blade. To avoid damage of the underlying cortex by friction-induced heat, extracellular saline was added to the skull periodically, and drilling was interrupted to permit heat dissipation. For sulforhodamine 101 co-labeling of astrocytes [138] a small hole (around 200 μm in diameter; >600 μm away from the imaging site) was made with a sharp 30 gauge needle at the edge of the exposed area similar to Christie et al. [30].

In experiments that required direct access to brain parenchyma, a small cranial

window (1 - 1.5 mm in diameter) was opened. In cases where a pipette was inserted into the brain, the dura mater was carefully removed. During this procedure, the exposed cortex was superfused with warm extracellular saline (135 mM NaCl, 5.4 mM KCl, 5 mM HEPES, 1.8 mM $CaCl_2$, pH 7.2 with NaOH). To dampen heartbeat- and breathing-induced brain motion, the craniotomy was filled with agarose (1.5%) in extracellular saline and covered with an immobilized coverglass. In addition, image acquisition was triggered from the animal's heartbeat if necessary. In imaging experiments where a cranial window was cut, only cells deeper than 80 μm below the pial surface were considered for image analysis to eliminate possible effects of the surgical preparation. Microglial cells at this depth did not show any signs of altered morphology or motility as determined in 4 experiments comprising imaging before and after craniotomy over a time course of several hours.

In Vivo Two-Photon Imaging. Two-photon imaging in the intact neocortex was performed as described [138]. To minimize photodamage, the average excitation laser power P was kept at a minimum for a sufficient signal-to-noise ratio (mean average power P $< 9 \pm 1$ mW and P $< 18 \pm 3$ mW at the sample surface for preparations with and without craniotomy, respectively). Unintentional photoactivation was observed only occasionally in experiments that used several fold higher light intensities (e.g. due to a suboptimal thinned skull preparation). Those experiments were excluded from analysis. Photobleaching was negligible, even in time-lapse recordings up to several hours. Laser wavelength was between 840 and 930 nm. Two-color detection was achieved using a 570 nm dichroic mirror and two photomultiplier tubes. Emission filters were a BG39-colored glass filter and a 610/75 bandpass filter in the 'green' and 'red' channel, respectively.

Time-lapse imaging of small cortical subvolumes was performed by repeated acquisition of small fluorescence image stacks (15 - 25 focal planes with 1 - 2 μm axial spacing). PMT settings and excitation power were kept constant during time-lapse recordings. Typically, subsequent image stacks were recorded every 20 - 45 s (sampling range: 0.25 s to 3 min). A sampling interval of 30 - 45 s was found to be sufficient to capture even the fastest morphological changes occurring on microglial processes (see also Fig. 3.26F). The presence of a thinned skull did not interfere with our ability to resolve the fine motile protrusions on microglial cell branches up to a depth of 200 μm below the pial surface, as evidenced by imaging the very same cells with and without skull.

Counterstains. In vivo labeling of cortical astrocytes was performed as described [138]. Briefly, sulforhodamine 101 was dissolved in extracellular saline (typically 100 - 300 μM) and briefly (around 1 min) applied to the exposed neocortical surface. Following application, the craniotomy was rinsed several times using pre-warmed extracellular saline. In some experiments, the blood plasma was stained via tail vein injection of FITC-labeled dextran (77 kDa, 1 - 5% w/v in extracellular saline, 0.1 - 0.2 ml) and/or Texas Red-dextran (3000 MW, 0.5 - 4.0% w/v in extracellular saline) [103].

Laser Lesions and LPS Application. Laser lesions were induced by exposing a confined area (spot size: 6 - 13 μm laterally; $\sim$1 μm axially) at 70 - 150 μm depth to transiently elevated laser illumination intensities (20 - 40 s duration, 20 - 30 mW and 45 -

60 mW average laser power for preparations with and without craniotomy, respectively). SR101 counterstaining of astroglial end feet, which enwrap the cortical microvasculature, was used to target the lesion at small blood vessels. Laser lesions were induced either through the thinned skull or using a small craniotomy (∼1 mm diameter).

For local intracortical application of LPS, a micropipette (borosilicate glass; 2.0 mm outer diameter; 4 - 7 MΩ tip resistence) was loaded with the endotoxin dissolved in extracellular saline (1 mg/ml). In addition, the pipette solution contained 100 μM Alexa Fluor 594 to allow for two-photon guided positioning of the micropipette. Following a baseline recording period, LPS was delivered using a brief pressure pulse on the micropipette (20 - 40 s; 0.1 - 0.2 bar).

Drug Application and ECoG Recording. To test whether microglia resting behavior depends on neural activity, the level of neural activity was either upregulated using the ionotropic GABA receptor blocker bicuculline (BCC; 50 μM in extracellular saline) or dampened using the sodium channel blocker tetrodotoxin (TTX; 25 - 50 μM in extracellular saline). Drugs were topically applied in experiments employing a small craniotomy (∼1 mm diameter) covered with agarose. The effectiveness of drug application was monitored by simultaneous electrocorticogram (ECoG) recordings. For ECoG recordings, the tip of a 85 μm diameter, teflon-coated silver wire was placed against the pial surface in one corner of the craniotomy. A reference electrode, made from a 280 μm diameter wire, was placed in a small hole over the cerebellum and immobilized with dental acrylic. ECoGs were recorded using a custom-built AC-coupled amplifier (input impedance 1 MΩ; bandwidth 0.1 Hz to 8 kHz) and sampled at 10 kHz using a 16-bit AD-converter and custom-written software.

Data Analysis. Image stacks and time series were analyzed using NIH Image and ImageJ software. All data are presented as mean ± SEM.

Volume densities of microglial cells were evaluated from fluorescence image stacks (2 μm axial spacing) by counting cells and dividing by the analysis volume (at least 0.0025 mm^3). Structural dynamics of microglial cells was quantified from time-lapse recordings at the level of individual somata, processes and fine protrusions. The analysis was performed on maximum-intensity projections of fluorescence image stacks. If necessary, focal drifts were manually corrected before calculating the maximum intensity projections. Lateral drifts were corrected using a custom-written alignment routine based on the position shift of the cross-correlation peak of successive projection images. In the majority of cases, image analysis was done blind with regard to experimental condition. The length of microglial processes and the velocity of length changes were evaluated from maximum-intensity projections and thus represent slight underestimates of the true values. The total length of processes per cell was always measured in average images representing 5 minute periods of recording. The number and distribution of fine protrusions on individual cells were evaluated by counting and marking the sites of protrusive activity in every projection image of a time-lapse recording. The lifetime of fine protrusions was determined as the full width at half maximum of the transient protrusions apparent in plots of protrusion length versus time (Fig. 3.26F).

To quantify volume surveillance by microglial cells we analyzed the time course of volume sampling in individual optical sections. A time series of cumulative volume sampling was created by producing maximum-intensity projections through an increasing number of frames of the original, drift corrected time series. Thus, each bright pixel in the cumulative images indicates that this particular subvolume had been sampled by a microglia process or protrusion in the time period between the first and last frame included in the projection. Cumulative time series were despeckled with a 1-point median filter, thresholded, and the rate of volume sampling was determined from the increase of the volume fraction occupied by microglia. Note that for illustration purposes only, projection images of stacks were used to generate the cumulative maximum-intensity projection shown in Fig. 3.28A.

In experiments employing drug application (BCC or TTX), the extensiveness of microglia tissue sampling was evaluated by measuring the total length of microglial processes and by analyzing the fluorescence intensity ratio between outer (distal) and inner (proximal) rings surrounding individual cells during 30 min periods immediately before and 1 hour after drug application. The area of these rings was chosen according to the territories occupied by individual microglial cells as evaluated from an average image of the corresponding time series (Fig. 3.29A). Background values, calculated from nearby dark areas (e.g. blood vessel lumen), were subtracted before taking the ratio. An increase of the outer-to-inner ring ratio thus indicates a more extensive sampling of outer microglia territory areas. The duration of drug application varied between 40 - 50 min and 70 - 140 min for BCC and TTX, respectively.

In several laser lesion experiments, spherical engulfments developed with time, indicating microglial phagocytotic activity. The diameter of these engulfments was measured in maximum-intensity projections of 2 - 3 focal planes. To analyze the time course of phagocytosis, diameters were normalized to inital values and a sigmoidal function was fitted to the temporal traces, yielding the percentage of shrinkage as well as the duration (time of 90 - 10% decrease from initial to final value) of the collapse step.

Bibliography

[1] E. M. Abdelbasset and S. Fedoroff. Dynamics of actin-filaments in microglia during fc receptor-mediated phagocytosis. *Acta Neuropathologica*, 88(6):527–537, 1994.

[2] D. A. Agard, Y. Hiraoka, P. J. Shaw, and J. W. Sedat. Fluorescence microscopy in three dimensions. *Methods Cell Biol.*, 30:353–378, 1989.

[3] G. P. Agrawal. *Nonlinear Fiber Optics*. Academic Press, 3rd edition, 2001.

[4] K. F. Ahrens and D. Kleinfeld. Current flow in vibrissa motor cortex can phase-lock with exploratory rhythmic whisking in rat. *Journal of Neurophysiology*, 92(3):1700–1707, 2004.

[5] M. Albota, D. Beljonne, J. L. Bredas, J. E. Ehrlich, J. Y. Fu, A. A. Heikal, S. E. Hess, T. Kogej, M. D. Levin, S. R. Marder, D. McCord-Maughon, J. W. Perry, H. Rockel, M. Rumi, C. Subramaniam, W. W. Webb, X. L. Wu, and C. Xu. Design of organic molecules with large two-photon absorption cross sections. *Science*, 281(5383):1653–1656, 1998.

[6] M. A. Albota, C. Xu, and W. W. Webb. Two-photon fluorescence excitation cross sections of biomolecular probes from 690 to 960 nm. *Applied Optics*, 37(31):7352–7356, 1998.

[7] C. B. Allen, T. Celikel, and D. E. Feldman. Long-term depression induced by sensory deprivation during cortical map plasticity in vivo. *Nature Neuroscience*, 6(3):291–299, 2003.

[8] A. Araque, G. Carmignoto, and P. G. Haydon. Dynamic signaling between astrocytes and neurons. *Annual Review of Physiology*, 63:795–813, 2001.

[9] A. Arieli, D. Shoham, R. Hildesheim, and A. Grinvald. Coherent spatiotemporal patterns of ongoing activity revealed by real-time optical imaging coupled with single-unit recording in the cat visual cortex. *Journal of Neurophysiology*, 73(5):2072–2093, 1995.

[10] J. Art. *Handbook of Biological Confocal Microscopy*, chapter Photon detectors for confocal microscopy. Plenum Press, J. B. Pawley, ed., New York, 1995.

[11] P. Ballabh, A. Braun, and M. Nedergaard. The blood-brain barrier: an overview - structure, regulation, and clinical implications. *Neurobiology of Disease*, 16(1):1–13, 2004.

[12] E. Beaurepaire and J. Mertz. Epifluorescence collection in two-photon microscopy. *Applied Optics*, 41(25):5376–5382, 2002.

[13] E. Beaurepaire, M. Oheim, and J. Mertz. Ultra-deep two-photon fluorescence excitation in turbid media. *Optics Communications*, 188(1-4):25–29, 2001.

[14] M. Beierlein, K. R. Gee, V. V. Martin, and W. G. Regehr. Presynaptic calcium measurements at physiological temperatures using a new class of dextran-conjugated indicators. *Journal of Neurophysiology*, 92(1):591–599, 2004.

[15] G. Bejerano, M. Pheasant, I. Makunin, S. Stephen, W. J. Kent, J. S. Mattick, and D. Haussler. Ultraconserved elements in the human genome. *Science*, 304(5675):1321–1325, 2004.

[16] R. W. Berg and D. Kleinfeld. Vibrissa movement elicited by rhythmic electrical microstimulation to motor cortex in the aroused rat mimics exploratory whisking. *Journal of Neurophysiology*, 90(5):2950–2963, 2003.

[17] J. Bewersdorf, R. Pick, and S. W. Hell. Multifocal multiphoton microscopy. *Optics Letters*, 23(9):655–657, 1998.

[18] P. Bezzi and A. Volterra. A neuron-glia signalling network in the active brain. *Current Opinion in Neurobiology*, 11(3):387–394, 2001.

[19] D. Bird and M. Gu. Two-photon fluorescence endoscopy with a micro-optic scanning head. *Optics Letters*, 28(17):1552–1554, 2003.

[20] R. E. D. Bishop and D. C. Johnson. *Mechanics of vibration.* Cambridge University Press, Cambridge, United Kingdom, 1960.

[21] T. Bonhoeffer and R. Yuste. Spine motility: Phenomenology, mechanisms, and function. *Neuron*, 35(6):1019–1027, 2002.

[22] C. Bonne. L'ecorce cerebrale. *Rev. Gen. Histol.*, 2:291–581, 1906.

[23] G. Bouwmans, F. Luan, J. C. Knight, P. S. J. Russell, L. Farr, B. J. Mangan, and H. Sabert. Properties of a hollow-core photonic bandgap fiber at 850 nm wavelength. *Optics Express*, 11(14):1613–1620, 2003.

[24] P. R. Brakeman, A. A. Lanahan, R. Obrien, K. Roche, C. A. Barnes, R. L. Huganir, and P. F. Worley. Homer: A protein that selectively binds metabotropic glutamate receptors. *Nature*, 386(6622):284–288, 1997.

[25] R. E. Campbell, O. Tour, A. E. Palmer, P. A. Steinbach, G. S. Baird, D. A. Zacharias, and R. Y. Tsien. A monomeric red fluorescent protein. *Proceedings of the National Academy of Sciences of the United States of America*, 99(12):7877–7882, 2002.

[26] F. Capani, M. H. Ellisman, and M. E. Martone. Filamentous actin is concentrated in specific subpopulations of neuronal and glial structures in rat central nervous system. *Brain Research*, 923(1-2):1–11, 2001.

[27] A. C. Charles, J. E. Merrill, E. R. Dirksen, and M. J. Sanderson. Intercellular signaling in glial-cells - calcium waves and oscillations in response to mechanical stimulation and glutamate. *Neuron*, 6(6):983–992, 1991.

[28] D. B. Chklovskii, B. W. Mel, and K. Svoboda. Cortical rewiring and information storage. *Nature*, 431(7010):782–788, 2004.

[29] S. H. Cho, F. X. Kartner, U. Morgner, E. P. Ippen, J. G. Fujimoto, J. E. Cunningham, and W. H. Knox. Generation of 90-nj pulses with a 4-mhz repetition-rate kerr-lens mode-locked ti : Al2o3 laser operating with net positive and negative intracavity dispersion. *Optics Letters*, 26(8):560–562, 2001.

[30] R. H. Christie, B. J. Bacskai, W. R. Zipfel, R. M. Williams, S. T. Kajdasz, W. W. Webb, and B. T. Hyman. Growth arrest of individual senile plaques in a model of alzheimer's disease observed by in vivo multiphoton microscopy. *Journal of Neuroscience*, 21(3):858–864, 2001.

[31] S. W. Clark, F. O. Ilday, and F. W. Wise. Fiber delivery of femtosecond pulses from a ti : sapphire laser. *Optics Letters*, 26(17):1320–1322, 2001.

[32] A. H. Cornellbell, S. M. Finkbeiner, M. S. Cooper, and S. J. Smith. Glutamate induces calcium waves in cultured astrocytes - long-range glial signaling. *Science*, 247(4941):470–473, 1990.

[33] M. Craner, T. Damarjian, S. Liu, B. Hains, A. Lo, J. Black, J. Newcombe, M. Cuzner, and S. Waxman. Sodium channels contribute to microglia/macrophage activation and function in eae and ms. *Glia*, 49:220–229, 2005.

[34] R. F. Cregan, B. J. Mangan, J. C. Knight, T. A. Birks, P. S. Russell, P. J. Roberts, and D. C. Allan. Single-mode photonic band gap guidance of light in air. *Science*, 285(5433):1537–1539, 1999.

[35] J. W. Dani, A. Chernjavsky, and S. J. Smith. Neuronal-activity triggers calcium waves in hippocampal astrocyte networks. *Neuron*, 8(3):429–440, 1992.

[36] J. DeFelipe. Cortical interneurons: from cajal to 2001. *Progress in Brain Research*, 136:215–238, 2002.

[37] J. DeFelipe, L. Alonso-Nanclares, and J. I. Arellano. Microstructure of the neocortex: Comparative aspects. *Journal of Neurocytology*, 31(3-5):299–316, 2002.

[38] J. DeFelipe and I. Farinas. The pyramidal neuron of the cerebral-cortex - morphological and chemical characteristics of the synaptic inputs. *Progress in Neurobiology*, 39(6):563–607, 1992.

[39] W. Denk. Optical beam power controller using a tiltable birefringent plate, u.s. patent no. us 6,249,379 b1, 2001.

[40] W. Denk. *Imaging in Neuroscience and Development - A Laboratory Manual*, chapter Principles of Multiphoton-excitation Fluorescence Microscopy, pages 53–58. Cold Spring Harbor Laboratory Press, Cold Spring Harbor, New York, r. yuste and a. konnerth, eds. edition, 2005.

[41] W. Denk, D. W. Piston, and W. W. Webb. *The Handbook of Biological Confocal Microscopy, J. B. Pawley, ed.*, chapter Two-photon molecular excitation in laser-scanning microscopy., pages 445–458. Plenum Press, New York, 1995.

[42] W. Denk, J. H. Strickler, and W. W. Webb. 2-photon laser scanning fluorescence microscopy. *Science*, 248(4951):73–76, 1990.

[43] W. Denk and K. Svoboda. Photon upmanship: Why multiphoton imaging is more than a gimmick. *Neuron*, 18(3):351–357, 1997.

[44] M. M. Dickens, M. P. Houlne, S. Mitra, and D. J. Bornhop. Method for depixelating micro-endoscopic images. *Optical Engineering*, 38(11):1836–1842, 1999.

[45] D. L. Dickensheets and G. S. Kino. Micromachined scanning confocal optical microscope. *Optics Letters*, 21(10):764–766, 1996.

[46] S. Diemer, J. Meister, R. Jung, S. Klein, M. Haisch, W. Fuss, and P. Hering. Liquid-core light guides for near-infrared applications. *Applied Optics*, 36(34):9075–9082, 1997.

[47] M. Diers-Fenger, F. Kirchhoff, H. Kettenmann, J. M. Levine, and J. Trotter. An2/ng2 protein-expressing glial progenitor cells in the murine cns: Isolation, differentiation, and association with radial glia. *Glia*, 34(3):213–228, 2001.

[48] T. Dittgen, A. Nimmerjahn, S. Komai, P. Licznerski, J. Waters, T. W. Margrie, F. Helmchen, W. Denk, M. Brecht, and P. Osten. Lentivirus-based genetic manipulations of cortical neurons and their optical and electrophysiological monitoring in vivo. *PNAS*, 101(52):18206–11, 2004.

[49] S. A. Dryga, O. A. Dryga, and S. Schlesinger. Identification of mutations in a sindbis virus variant able to establish persistent infection in bhk cells: The importance of a mutation in the nsp2 gene. *Virology*, 228(1):74–83, 1997.

[50] V. Dubaj, A. Mazzolini, A. Wood, and M. Harris. Optic fibre bundle contact imaging probe employing a laser scanning confocal microscope. *Journal of Microscopy-Oxford*, 207:108–117, 2002.

[51] C. Eder. Ion channels in microglia (brain macrophages). *American Journal of Physiology-Cell Physiology*, 44(2):C327–C342, 1998.

[52] B. Ehinger, C. L. Zucker, A. Bruun, and A. Adolph. In-vivo staining of oligodendroglia in the rabbit retina. *Glia*, 10(1):40–48, 1994.

[53] M. U. Ehrengruber, S. Hennou, H. Bueler, H. Y. Naim, N. Deglon, and K. Lundstrom. Gene transfer into neurons from hippocampal slices: comparison of recombinant semliki forest virus, adenovirus, adeno-associated virus, lentivirus, and measles virus. *Molecular and Cellular Neuroscience*, 17:855–871, 2001.

[54] S. M. Elbashir, J. Harborth, W. Lendeckel, A. Yalcin, K. Weber, and T. Tuschl. Duplexes of 21-nucleotide rnas mediate rna interference in cultured mammalian cells. *Nature*, 411(6836):494–498, 2001.

[55] F. Engert and T. Bonhoeffer. Dendritic spine changes associated with hippocampal long-term synaptic plasticity. *Nature*, 399(6731):66–70, 1999.

[56] L. Fagni, P. Worley, and F. Ango. Homer as both a scaffold and transduction molecule. *Sci STKE 2002:RE8*, 2002.

[57] G. P. Feng, R. H. Mellor, M. Bernstein, C. Keller-Peck, Q. T. Nguyen, M. Wallace, J. M. Nerbonne, J. W. Lichtman, and J. R. Sanes. Imaging neuronal subsets in transgenic mice expressing multiple spectral variants of gfp. *Neuron*, 28(1):41–51, 2000.

[58] J. R. Fetcho and D. M. O'Malley. Imaging neuronal networks in behaving animals. *Current Opinion in Neurobiology*, 7(6):832–838, 1997.

[59] J. C. Fiala, B. Allwardt, and K. M. Harris. Dendritic spines do not split during hippocampal ltp or maturation. *Nature Neuroscience*, 5(4):297–298, 2002.

[60] R. D. Fields and B. Stevens-Graham. Neuroscience - new insights into neuron-glia communication. *Science*, 298(5593):556–562, 2002.

[61] A. Fine. *Imaging in Neuroscience and Development - a Laboratory Manual*, chapter Confocal Microscopy: Principles and Practice, pages 43–51. Cold Spring Harbor Laboratory Press, R. Yuste and A. Konnerth, eds., Cold Spring Harbor, New York, 2005.

[62] K. Fleischhauer. Fluoreszenzmikroskopische untersuchungen an der faserglia, i. beobachtungen an den wandungen der hirnventrikel der katze (seitenventrikel, iii. ventrikel). *Z. Zellf.*, 51:467–496, 1960.

[63] R. L. Fork, O. E. Martinez, and J. P. Gordon. Negative dispersion using pairs of prisms. *Optics Letters*, 9:150–152, 1984.

[64] W. Gobel, J. N. D. Kerr, A. Nimmerjahn, and F. Helmchen. Miniaturized two-photon microscope based on a flexible coherent fiber bundle and a gradient-index lens objective. *Optics Letters*, 29(21):2521–2523, 2004.

[65] W. Gobel, A. Nimmerjahn, and F. Helmchen. Distortion-free delivery of nanojoule femtosecond pulses from a ti : sapphire laser through a hollow-core photonic crystal fiber. *Optics Letters*, 29(11):1285–1287, 2004.

[66] M. Goeppert-Mayer. *Ueber Elementarakte mit zwei Quantenspruengen.* PhD thesis, 1930.

[67] D. Grass, P. G. Pawlowski, J. Hirrlinger, N. Papadopoulos, D. W. Richter, F. Kirchhoff, and S. Hulsmann. Diversity of functional astroglial properties in the respiratory network. *Journal of Neuroscience*, 24(6):1358–1365, 2004.

[68] O. Griesbeck, G. S. Baird, R. E. Campbell, D. A. Zacharias, and R. Y. Tsien. Reducing the environmental sensitivity of yellow fluorescent protein - mechanism and applications. *Journal of Biological Chemistry*, 276(31):29188–29194, 2001.

[69] J. Grutzendler, N. Kasthuri, and W. B. Gan. Long-term dendritic spine stability in the adult cortex. *Nature*, 420(6917):812–816, 2002.

[70] M. Gu. Resolution in 3-photon fluorescence scanning microscopy. *Opt. Lett.*, 21:988–990, 1996.

[71] M. Gu and C. J. R. Sheppard. Effects of finite-sized detector on the otf of confocal fluorescent microscopy. *Optik*, 89:65–69, 1991.

[72] K. Haas, W. C. Sin, A. Javaherian, Z. Li, and H. T. Cline. Single-cell electroporation for gene transfer in vivo. *Neuron*, 29(3):583–591, 2001.

[73] A. K. Hadjantonakis, M. E. Dickinson, S. E. Fraser, and V. E. Papaioannou. Technicolour transgenics: Imaging tools for functional genomics in the mouse. *Nature Reviews Genetics*, 4(8):613–625, 2003.

[74] P. E. Hanninen, E. Soini, and S. W. Hell. Continuous-wave excitation 2-photon fluorescence microscopy. *Journal of Microscopy-Oxford*, 176:222–225, 1994.

[75] M. T. Hasan, R. W. Friedrich, T. Euler, M. E. Larkum, G. Giese, M. Both, J. Duebel, J. Waters, H. Bujard, O. Griesbeck, R. Y. Tsien, T. Nagai, A. Miyawaki, and W. Denk. Functional fluorescent ca2+ indicator proteins in transgenic mice under tet control. *PLoS Biol.*, 2(6):e163, 2004.

[76] A. A. Heikal, S. T. Hess, G. S. Baird, R. Y. Tsien, and W. W. Webb. Molecular spectroscopy and dynamics of intrinsically fluorescent proteins: Coral red (dsred) and yellow (citrine). *Proceedings of the National Academy of Sciences of the United States of America*, 97(22):11996–12001, 2000.

[77] F. Helmchen. Miniaturization of fluorescence microscopes using fibre optics. *Experimental Physiology*, 87(6):737–745, 2002.

[78] F. Helmchen and W. Denk. New developments in multiphoton microscopy. *Current Opinion in Neurobiology*, 12(5):593–601, 2002.

[79] F. Helmchen, M. S. Fee, D. W. Tank, and W. Denk. A miniature head-mounted two-photon microscope: High-resolution brain imaging in freely moving animals. *Neuron*, 31(6):903–912, 2001.

[80] F. Helmchen, K. Svoboda, W. Denk, and D. W. Tank. In vivo dendritic calcium dynamics in deep-layer cortical pyramidal neurons. *Nature Neuroscience*, 2(11):989–996, 1999.

[81] F. Helmchen, D. W. Tank, and W. Denk. Enhanced two-photon excitation through optical fiber by single-mode propagation in a large core. *Applied Optics*, 41(15):2930–2934, 2002.

[82] F. Helmchen and J. Waters. Ca2+ imaging in the mammalian brain in vivo. *European Journal of Pharmacology*, 447(2-3):119–129, 2002.

[83] H. Hirase, L. F. Qian, P. Bartho, and G. Buzsaki. Calcium dynamics of cortical astrocytic networks in vivo. *Plos Biology*, 2(4):494–499, 2004.

[84] J. Hirrlinger, S. Hulsmann, and F. Kirchhoff. Astroglial processes show spontaneous motility at active synaptic terminals in situ. *European Journal of Neuroscience*, 20(8):2235–2239, 2004.

[85] A. Holtmaat, J. T. Trachtenberg, L. Wilbrecht, G. M. Shepherd, X. Q. Zhang, G. W. Knott, and K. Svoboda. Transient and persistent dendritic spines in the neocortex in vivo. *Neuron*, 45(2):279–291, 2005.

[86] J. D. Hommel, R. M. Sears, D. Georgescu, D. L. Simmons, and R. J. DiLeone. Local gene knockdown in the brain using viral-mediated rna interference. *Nature Medicine*, 9(12):1539–1544, 2003.

[87] A. Hopt and E. Neher. Highly nonlinear photodamage in two-photon fluorescence microscopy. *Biophysical Journal*, 80(4):2029–2036, 2001.

[88] T. Hosokawa, T. V. P. Bliss, and A. Fine. Quantitative three-dimensional confocal microscopy of synaptic structures in living brain tissue. *Microsc. Res. Tech.*, 29:290–296, 1994.

[89] J. D. Jackson. *Classical Electrodynamics*. John Wiley and Sons, Inc., New York, 3 edition, 1999.

[90] K. Jeffery and R. Hayman. Plasticity of the hippocampal place cell representation. *Rev Neurosci.*, 15(5):309–31, 2004.

[91] J. C. Jung, A. D. Mehta, E. Aksay, R. Stepnoski, and M. J. Schnitzer. In vivo mammalian brain imaging using one- and two-photon fluorescence microendoscopy. *Journal of Neurophysiology*, 92(5):3121–3133, 2004.

[92] J. C. Jung and M. J. Schnitzer. Multiphoton endoscopy. *Optics Letters*, 28(11):902–904, 2003.

[93] S. Jung, J. Aliberti, P. Graemmel, M. J. Sunshine, G. W. Kreutzberg, A. Sher, and D. R. Littman. Analysis of fractalkine receptor cx(3)cr1 function by targeted deletion and green fluorescent protein reporter gene insertion. *Molecular and Cellular Biology*, 20(11):4106–4114, 2000.

[94] W. Kaiser and C. G. B. Garrett. 2-photon excitation in caf2 - eu2+. *Physical Review Letters*, 7(6):229, 1961.

[95] E. R. Kandel, J. H. Schwartz, and T. M. Jessell. *Principles of Neural Science*. McGraw-Hill Education, 2000.

[96] K. A. Kasischke, H. D. Vishwasrao, P. J. Fisher, W. R. Zipfel, and W. W. Webb. Neural activity triggers neuronal oxidative metabolism followed by astrocytic glycolysis. *Science*, 305(5680):99–103, 2004.

[97] A. Kato, F. Ozawa, Y. Saitoh, K. Hirai, and K. Inokuchi. vesl, a gene encoding vasp/ena family related protein, is upregulated during seizure, long-term potentiation and synaptogenesis. *Febs Letters*, 412(1):183–189, 1997.

[98] J. Keifer, D. Vyas, and J. C. Houk. Sulforhodamine labeling of neural circuits engaged in motor pattern generation in the in vitro turtle brainstem-cerebellum. *J Neurosci*, 12(8):3187, 1992.

[99] J. N. D. Kerr and F. Helmchen. In vivo calcium imaging reveals heterogenous patterns of network activity during cortical up-states, society for neuroscience meeting abstract, 2004.

[100] H. Kettenmann and B. R. Ransom. *Neuroglia*. Oxford University Press, 2 edition, 2004.

[101] P. Kettunen, J. Demas, C. Lohmann, N. Kasthuri, Y. D. Gong, R. O. L. Wong, and W. B. Gan. Imaging calcium dynamics in the nervous system by means of ballistic delivery of indicators. *Journal of Neuroscience Methods*, 119(1):37–43, 2002.

[102] J. Kim, T. Dittgen, A. Nimmerjahn, J. Waters, V. Pawlak, F. Helmchen, S. Schlesinger, P. H. Seeburg, and P. Osten. Sindbis vector sinrep(nsp2s(726)): a tool for rapid heterologous expression with attenuated cytotoxicity in neurons. *Journal of Neuroscience Methods*, 133(1-2):81–90, 2004.

[103] D. Kleinfeld and W. Denk. Two-photon imaging of neocortical microcirculation. In R. Yuste, F. Lanni, and A. Konnerth, editors, *Imaging Neurons: A Laboratory Manual*. Cold Spirng Harbor Press, Cold Spring Harbor, 1999.

[104] D. Kleinfeld, P. P. Mitra, F. Helmchen, and W. Denk. Fluctuations and stimulus-induced changes in blood flow observed in individual capillaries in layers 2 through 4 of rat neocortex. *Proceedings of the National Academy of Sciences of the United States of America*, 95(26):15741–15746, 1998.

[105] J. Knittel, L. Schnieder, G. Buess, B. Messerschmidt, and T. Possner. Endoscope-compatible confocal microscope using a gradient index-lens system. *Optics Communications*, 188(5-6):267–273, 2001.

[106] H. J. Koester, D. Baur, R. Uhl, and S. W. Hell. Ca2+ fluorescence imaging with pico- and femtosecond two-photon excitation: Signal and photodamage. *Biophysical Journal*, 77(4):2226–2236, 1999.

[107] K. Konig, T. W. Becker, P. Fischer, I. Riemann, and K. J. Halbhuber. Pulse-length dependence of cellular response to intense near-infrared laser pulses in multiphoton microscopes. *Optics Letters*, 24(2):113–115, 1999.

[108] A. C. Kreitzer, K. R. Gee, E. A. Archer, and W. G. Regehr. Monitoring presynaptic calcium dynamics in projection fibers by in vivo loading of a novel calcium indicator. *Neuron*, 27(1):25–32, 2000.

[109] G. W. Kreutzberg. Microglia: A sensor for pathological events in the cns. *Trends in Neurosciences*, 19(8):312–318, 1996.

[110] J. R. Lakowicz and I. Gryczynski. *Topics in Fluorescence Spectroscopy*, volume 5. 1997.

[111] A. Lanahan and P. Worley. Immediate-early genes and synaptic function. *Neurobiology of Learning and Memory*, 70(1-2):37–43, 1998.

[112] E. T. Larsen, M. Valo, J. Berg-Johnsen, and I. A. Langmoen. Isoflurane reduces synaptic glutamate release without changing cytosolic free calcium in isolated nerve terminals. *European Journal of Anaesthesiology*, 15(2):224–229, 1998.

[113] D. R. Larson, W. R. Zipfel, R. M. Williams, S. W. Clark, M. P. Bruchez, F. W. Wise, and W. W. Webb. Water-soluble quantum dots for multiphoton fluorescence imaging in vivo. *Science*, 300:1434–1436, 2003.

[114] L. J. Lawson, V. H. Perry, P. Dri, and S. Gordon. Heterogeneity in the distribution and morphology of microglia in the normal adult-mouse brain. *Neuroscience*, 39(1):151–170, 1990.

[115] A. Lehmenkuhler, E. Sykova, J. Svoboda, K. Zilles, and C. Nicholson. Extracellular-space parameters in the rat neocortex and subcortical white-matter during postnatal-development determined by diffusion analysis. *Neuroscience*, 55(2):339–351, 1993.

[116] B. Lendvai, E. A. Stern, B. Chen, and K. Svoboda. Experience-dependent plasticity of dendritic spines in the developing rat barrel cortex in vivo. *Nature*, 404(6780):876–881, 2000.

[117] M. J. Levene, D. A. Dombeck, K. A. Kasischke, R. P. Molloy, and W. W. Webb. In vivo multiphoton microscopy of deep brain tissue. *Journal of Neurophysiology*, 91(4):1908–1912, 2004.

[118] J. W. Lichtman, R. S. Wilkinson, and M. M. Rich. Multiple innervation of tonic endplates revealed by activity-dependent uptake of fluorescent probes. *Nature*, 314:357–359, 1985.

[119] J. A. Lissajous. Note sur une methode nouvelle applicable a l'etude des mouvements vibratoires. *Comptes Rendus des Seances de l'Academie des Sciences*, 41:814–817, 1855.

[120] C. Lohmann, A. Finski, and T. Bonhoeffer. Local calcium transients regulate the spontaneous motility of dendritic filopodia. *Nature Neuroscience*, 8(3):305–312, 2005.

[121] M. Maletic-Savatic, R. Malinow, and K. Svoboda. Rapid dendritic morphogenesis in ca1 hippocampal dendrites induced by synaptic activity. *Science*, 283(5409):1923–1927, 1999.

[122] T. W. Margrie, A. H. Meyer, A. Caputi, H. Monyer, M. T. Hasan, A. T. Schaefer, W. Denk, and M. Brecht. Targeted whole-cell recordings in the mammalian brain in vivo. *Neuron*, 39(6):911–918, 2003.

[123] H. Markram, M. Toledo-Rodriguez, Y. Wang, A. Gupta, G. Silberberg, and C. Z. Wu. Interneurons of the neocortical inhibitory system. *Nature Reviews Neuroscience*, 5(10):793–807, 2004.

[124] K. Matthias, F. Kirchhoff, G. Seifert, K. Huttmann, M. Matyash, H. Kettenmann, and C. Steinhauser. Segregated expression of ampa-type glutamate receptors and glutamate transporters defines distinct astrocyte populations in the mouse hippocampus. *Journal of Neuroscience*, 23(5):1750–1758, 2003.

[125] X. Michalet, F. F. Pinaud, L. A. Bentolila, J. M. Tsay, S. Doose, J. J. Li, G. Sundaresan, A. M. Wu, G. S. S., and S. Weiss. Quantum dots for live cells, in vivo imaging, and diagnostics. *Science*, 307:538–544, 2005.

[126] M. Muller, J. Squier, R. Wolleschensky, U. Simon, and G. J. Brakenhoff. Dispersion pre-compensation of 15 femtosecond optical pulses for high-numerical-aperture objectives. *Journal of Microscopy-Oxford*, 191:141–150, 1998.

[127] S. J. Mulligan and B. A. MacVicar. Calcium transients in astrocyte endfeet cause cerebrovascular constrictions. *Nature*, 431(7005):195–199, 2004.

[128] T. Nagai, A. Sawano, E. S. Park, and A. Miyawaki. Circularly permuted green fluorescent proteins engineered to sense ca2+. *Proceedings of the National Academy of Sciences of the United States of America*, 98(6):3197–3202, 2001.

[129] J. I. Nagy, A. V. Ionescu, B. D. Lynn, and J. E. Rash. Coupling of astrocyte connexins cx26, cx30, cx43 to oligodendrocyte cx29, cx32, cx47: Implications from normal and connexin32 knockout mice. *Glia*, 44(3):205–218, 2003.

[130] J. Nakai, M. Ohkura, and K. Imoto. A high signal-to-noise ca2+ probe composed of a single green fluorescent protein. *Nature Biotechnology*, 19(2):137–141, 2001.

[131] V. E. Nava, A. Rosen, M. A. Veliuona, R. J. Clem, B. Levine, and J. M. Hardwick. Sindbis virus induces apoptosis through a caspase-dependent, crma-sensitive pathway. *Journal of Virology*, 72(1):452–459, 1998.

[132] M. Nedergaard. Direct signaling from astrocytes to neurons in cultures of mammalian brain-cells. *Science*, 263(5154):1768–1771, 1994.

[133] M. Nedergaard, B. Ransom, and S. A. Goldman. New roles for astrocytes: Redefining the functional architecture of the brain. *Trends in Neurosciences*, 26(10):523–530, 2003.

[134] B. Nico, L. Roncali, D. Mangieri, and D. Ribatti. Blood-brain barrier alterations in mdx mouse, an animal model of the duchenne muscular dystrophy. *Current Neurovascular Research*, 2(1):47–54, 2005.

[135] A. Nimmerjahn. Aufbau und optimierung eines faseroptischen systems zur effizienten zwei-photonen fluoreszenzanregung nach der faser. Master's thesis, Universitaet Heidelberg, Heidelberg, 2001.

[136] A. Nimmerjahn, W. Denk, and F. Helmchen. Two-photon fiberscope imaging of cellular networks in the neocortex in vivo, society for neuroscience meeting abstract, 2003.

[137] A. Nimmerjahn, F. Kirchhoff, and F. Helmchen. Resting microglial cells are highly dynamic surveillants of brain parenchyma in vivo. *Science*, Epub ahead of print, 2005.

[138] A. Nimmerjahn, F. Kirchhoff, J. N. D. Kerr, and F. Helmchen. Sulforhodamine 101 as a specific marker of astroglia in the neocortex in vivo. *Nature Methods*, 1(1):31–37, 2004.

[139] C. Nolte, M. Matyash, T. Pivneva, C. G. Schipke, C. Ohlemeyer, U. K. Hanisch, F. Kirchhoff, and H. Kettenmann. Gfap promoter-controlled egfp-expressing transgenic mice: A tool to visualize astrocytes and astrogliosis in living brain tissue. *Glia*, 33(1):72–86, 2001.

[140] C. Nolte, T. Moller, T. Walter, and H. Kettenmann. Complement 5a controls motility of murine microglial cells in vitro via activation of an inhibitory g-protein and the rearrangement of the actin cytoskeleton. *Neuroscience*, 73(4):1091–1107, 1996.

[141] T. B. Norris. Femtosecond pulse amplification at 250 khz with a ti-sapphire regenerative amplifier and application to continuum generation. *Optics Letters*, 17(14):1009–1011, 1992.

[142] M. Oheim, E. Beaurepaire, E. Chaigneau, J. Mertz, and S. Charpak. Two-photon microscopy in brain tissue: parameters influencing the imaging depth. *Journal of Neuroscience Methods*, 111(1):29–37, 2001.

[143] K. Ohki, S. Chung, Y. H. Ch'ng, P. Kara, and R. C. Reid. Functional imaging with cellular resolution reveals precise micro-architecture in visual cortex. *Nature*, 433(7026):597–603, 2005.

[144] T. Okada, N. Yamada, W. Kakegawa, K. Tsuzuki, M. Kawamura, H. Nawa, M. Iino, and S. Ozawa. Sindbis viral-mediated expression of ca2+-permeable ampa receptors at hippocampal ca1 synapses and induction of nmda receptor-independent long-term potentiation. *European Journal of Neuroscience*, 13(8):1635–1643, 2001.

[145] B. A. Olshausen and D. J. Field. Sparse coding of sensory inputs. *Current Opinion in Neurobiology*, 14(4):481–487, 2004.

[146] D. M. Omalley, Y. H. Kao, and J. R. Fetcho. Imaging the functional organization of zebrafish hindbrain segments during escape behaviors. *Neuron*, 17(6):1145–1155, 1996.

[147] S. Pakalnis, V. Sitas, H. Schneckenburger, and R. Rotomskis. Picosecond absorption spectroscopy of biologically active pigments nadh, fmn and fluorescence marker rhodamine-123. In *The Third Internet Photochemistry and Photobiology Conference*, 2000.

[148] V. Parpura, T. A. Basarsky, F. Liu, K. Jeftinija, S. Jeftinija, and P. G. Haydon. Glutamate-mediated astrocyte neuron signaling. *Nature*, 369(6483):744–747, 1994.

[149] L. Pasti, A. Volterra, T. Pozzan, and G. Carmignoto. Intracellular calcium oscillations in astrocytes: A highly plastic, bidirectional form of communication between neurons and astrocytes in situ. *Journal of Neuroscience*, 17(20):7817–7830, 1997.

[150] C. C. H. Petersen, A. Grinvald, and B. Sakmann. Spatiotemporal dynamics of sensory responses in layer 2/3 of rat barrel cortex measured in vivo by voltage-sensitive dye imaging combined with whole-cell voltage recordings and neuron reconstructions. *Journal of Neuroscience*, 23(4):1298–1309, 2003.

[151] T. A. Pologruto, R. Yasuda, and K. Svoboda. Monitoring neural activity and ca2+ with genetically encoded ca2+ indicators. *Journal of Neuroscience*, 24(43):9572–9579, 2004.

[152] C. Portera-Cailliau, D. T. Pan, and R. Yuste. Activity-regulated dynamic behavior of early dendritic protrusions: Evidence for different types of dendritic filopodia. *Journal of Neuroscience*, 23(18):7129–7142, 2003.

[153] A. Privat, M. Gimenez-Ribotta, and J.-L. Ridet. Morphology of astrocytes. In B. R. Ransom and H. Kettenmann, editors, *Neuroglia*, pages 3–22. Oxford University Press, Oxford, 1995.

[154] T. Ragan, H. Huang, and P. T. C. So. In vivo and ex vivo tissue applications of two-photon microscopy. *Methods in Enzymology*, 361:481–505, 2003.

[155] G. Raivich, M. Bohatschek, C. U. A. Kloss, A. Werner, L. L. Jones, and G. W. Kreutzberg. Neuroglial activation repertoire in the injured brain: graded response, molecular mechanisms and cues to physiological function. *Brain Research Reviews*, 30(1):77–105, 1999.

[156] M. Ramaswamy, M. Ulman, J. Paye, and J. G. Fujimoto. Cavity-dumped femtosecond kerr-lens mode-locked ti-al2o3 laser. *Optics Letters*, 18(21):1822–1824, 1993.

[157] J. K. Ranka, A. L. Gaeta, A. Baltuska, M. S. Pshenichnikov, and D. A. Wiersma. Autocorrelation measurement of 6-fs pulses based on the two-photon-induced photocurrent in a gaasp photodiode. *Optics Letters*, 22(17):1344–1346, 1997.

[158] B. Ransom, T. Behar, and M. Nedergaard. New roles for astrocytes (stars at last). *Trends in Neurosciences*, 26(10):520–522, 2003.

[159] J. Rathenberg, T. Nevian, and V. Witzemann. High-efficiency transfection of individual neurons using modified electrophysiology techniques. *Journal of Neuroscience Methods*, 126(1):91–98, 2003.

[160] D. A. Rubinson, C. P. Dillon, A. V. Kwiatkowski, C. Sievers, L. L. Yang, J. Kopinja, M. D. Zhang, M. T. McManus, F. B. Gertler, M. L. Scott, and L. Van Parijs. A lentivirus-based system to functionally silence genes in primary mammalian cells, stem cells and transgenic mice by rna interference. *Nature Genetics*, 33(3):401–406, 2003.

[161] U. Rudolph and B. Antkowiak. Molecular and neuronal substrates for general anaesthetics. *Nature Reviews Neuroscience*, 5(9):709–720, 2004.

[162] Y. S. Sabharwal, A. R. Rouse, L. Donaldson, M. F. Hopkins, and A. F. Gmitro. Slit-scanning confocal microendoscope for high-resolution in vivo imaging. *Applied Optics*, 38(34):7133–7144, 1999.

[163] R. G. A. Safranyos, S. Caveney, J. G. Miller, and N. O. Petersen. Relative roles of gap junction channels and cytoplasm in cell-to-cell diffusion of fluorescent tracers. *Proceedings of the National Academy of Sciences of the United States of America*, 84(8):2272–2276, 1987.

[164] C. Sala, K. Futai, K. Yamamoto, P. F. Worley, Y. Hayashi, and M. Sheng. Inhibition of dendritic spine morphogenesis and synaptic transmission by activity-inducible protein homer1a. *Journal of Neuroscience*, 23(15):6327–6337, 2003.

[165] A. Schuz and G. Palm. Density of neurons and synapses in the cerebral-cortex of the mouse. *Journal of Comparative Neurology*, 286(4):442–455, 1989.

[166] M. Segal. Dendritic spines and long-term plasticity. *Nature Reviews Neuroscience*, 6(4):277–284, 2005.

[167] E. J. Seibel and Q. Y. J. Smithwick. Unique features of optical scanning, single fiber endoscopy. *Lasers in Surgery and Medicine*, 30(3):177–183, 2002.

[168] N. C. Shaner, R. E. Campbell, P. A. Steinbach, B. N. G. Giepmans, A. E. Palmer, and R. Y. Tsien. Improved monomeric red, orange and yellow fluorescent proteins derived from discosoma sp red fluorescent protein. *Nature Biotechnology*, 22(12):1567–1572, 2004.

[169] P. J. Shaw. *Handbook of biological confocal microscopy*, chapter Comparison of widefield/deconvolution and confocal microscopy for 3D imaging, pages 373–387. Plenum Press, J. B. Pawley, ed., New York, 2 edition, 1995.

[170] C. J. R. Sheppard and M. Gu. Image-formation in 2-photon fluorescence microscopy. *Optik*, 86:104–106, 1990.

[171] O. Shimomura, F. H. Johnson, and Y. Saiga. Extraction, purification and properties of aequorin, a bioluminescent protein from luminous hydromedusan, aequorea. *Journal of Cellular and Comparative Physiology*, 59(3):223, 1962.

[172] M. Simard, G. Arcuino, T. Takano, Q. S. Liu, and M. Nedergaard. Signaling at the gliovascular interface. *Journal of Neuroscience*, 23(27):9254–9262, 2003.

[173] M. Simard and M. Nedergaard. The neurobiology of glia in the context of water and ion homeostasis. *Neuroscience*, 129(4):877–896, 2004.

[174] F. M. Smart and S. Halpain. Regulation of dendritic spine stability. *Hippocampus*, 10(5):542–554, 2000.

[175] P. T. C. So, C. Y. Dong, B. R. Masters, and K. M. Berland. Two-photon excitation fluorescence microscopy. *Annual Review of Biomedical Engineering*, 2:399–429, 2000.

[176] G. Sohl, S. Maxeiner, and K. Willecke. Expression and functions of neuronal gap junctions. *Nature Reviews Neuroscience*, 6(3):191–200, 2005.

[177] J. Squier and M. Muller. High resolution nonlinear microscopy: A review of sources and methods for achieving optimal imaging. *Review of Scientific Instruments*, 72(7):2855–2867, 2001.

[178] E. H. K. Stelzer, S. Hell, and S. Lindek. Nonlinear absorption extends confocal fluorescence microscopy into the ultra-violet regime and confines the illumination volume. *Optics Commun.*, 104:223–228, 1994.

[179] N. Stence, M. Waite, and M. E. Dailey. Dynamics of microglia activation: A confocal time-lapse analysis in hippocampal slices. *Glia*, 33:256–266, 2001.

[180] G. Stoll and S. Jander. The role of microglia and macrophages in the pathophysiology of the cns. *Progress in Neurobiology*, 58(3):233–247, 1999.

[181] C. Stosiek, O. Garaschuk, K. Holthoff, and A. Konnerth. In vivo two-photon calcium imaging of neuronal networks. *Proceedings of the National Academy of Sciences U.S.A.*, 100(12):7319–7324, 2003.

[182] W. J. Streit. Microglia as neuroprotective, immunocompetent cells of the cns. *Glia*, 40(2):133–139, 2002.

[183] W. J. Streit. Microglia and alzheimer's disease pathogenesis. *Journal of Neuroscience Research*, 77(1):1–8, 2004.

[184] K. Svoboda, W. Denk, D. Kleinfeld, and D. W. Tank. In vivo dendritic calcium dynamics in neocortical pyramidal neurons. *Nature*, 385(6612):161–165, 1997.

[185] K. Svoboda, F. Helmchen, W. Denk, and D. W. Tank. Spread of dendritic excitation in layer 2/3 pyramidal neurons in rat barrel cortex in vivo. *Nature Neuroscience*, 2(1):65–73, 1999.

[186] J. Szentagothai. *Synaptology of the Visual Cortex*, volume VII/3 of *Handbook of Sensory Physiology*. Springer, Berlin, New York, 1973.

[187] P. Theer. *On the fundamental imaging-depth limit in two-photon microscopy*. PhD thesis, Heidelberg, Univ., 2004.

[188] P. Theer, M. T. Hasan, and W. Denk. Two-photon imaging to a depth of 1000 mu m in living brains by use of a ti : Al2o3 regenerative amplifier. *Optics Letters*, 28(12):1022–1024, 2003.

[189] N. Toni, P. A. Buchs, I. Nikonenko, C. R. Bron, and D. Muller. Ltp promotes formation of multiple spine synapses between a single axon terminal and a dendrite. *Nature*, 402(6760):421–425, 1999.

[190] J. T. Trachtenberg, B. E. Chen, G. W. Knott, G. P. Feng, J. R. Sanes, E. Welker, and K. Svoboda. Long-term in vivo imaging of experience-dependent synaptic plasticity in adult cortex. *Nature*, 420(6917):788–794, 2002.

[191] E. B. Treacy. Optical pulse compression with diffraction gratings. *IEEE Journal of Quantum Electronics QE 5*, (9):454, 1969.

[192] D. Trono. Lentiviral vectors: turning a deadly foe into a therapeutic agent. *Gene Therapy*, 7(1):20–23, 2000.

[193] M. Tsang, D. Psaltis, and F. G. Omenetto. Reverse propagation of femtosecond pulses in optical fibers. *Optics Letters*, 28(20):1873–1875, 2003.

[194] R. Y. Tsien. Fluorescent-probes of cell signaling. *Annual Review of Neuroscience*, 12:227–253, 1989.

[195] R. Y. Tsien. The green fluorescent protein. *Annual Review of Biochemistry*, 67:509–544, 1998.

[196] R. Y. Tsien. Building and breeding molecules to spy on cells and tumors. *Febs Letters*, 579(4):927–932, 2005.

[197] R. J. Ulevitch and P. S. Tobias. Receptor-dependent mechanisms of cell stimulation by bacterial-endotoxin. *Annual Review of Immunology*, 13:437–457, 1995.

[198] E. M. Ullian, S. K. Sapperstein, K. S. Christopherson, and B. A. Barres. Control of synapse number by glia. *Science*, 291(5504):657–661, 2001.

[199] C. Van den Haute, K. Eggermont, B. Nuttin, Z. Debyser, and V. Baekelandt. Lentiviral vector-mediated delivery of short hairpin rna results in persistent knockdown of gene expression in mouse brain. *Human Gene Therapy*, 14(18):1799–1807, 2003.

[200] D. van Rossum and U. K. Hanisch. Microglia. *Metabolic Brain Disease*, 19(3-4):393–411, 2004.

[201] A. Vazdarjanova, B. L. McNaughton, C. A. Barnes, P. F. Worley, and J. F. Guzowski. Experience-dependent coincident expression of the effector immediate-early genes arc and homer 1a in hippocampal and neocortical neuronal networks. *Journal of Neuroscience*, 22(23):10067–10071, 2002.

[202] A. Verkhratsky and H. Kettenmann. Calcium signalling in glial cells. *Trends in Neurosciences*, 19(8):346–352, 1996.

[203] F. Vilhardt. Microglia: phagocyte and glia cell. *International Journal of Biochemistry and Cell Biology*, 37(1):17–21, 2005.

[204] A. Wallraff, B. Odermatt, K. Willecke, and C. Steinhaeuser. Distinct types of astroglial cells in the hippocampus differ in gap junction coupling. *Glia*, 48(11):36–43, 2004.

[205] J. Waters, M. Larkum, B. Sakmann, and F. Helmchen. Supralinear ca2+ influx in dendritic tufts of layer 2/3 neocortical pyramidal neurons in vitro and in vivo. *Journal of Neuroscience*, 23(24):8558–8567, 2003.

[206] C. L. Willis, C. C. Nolan, S. N. Reith, T. Lister, M. J. W. Prior, C. J. Guerin, G. Mavroudis, and D. E. Ray. Focal astrocyte loss is followed by microvascular damage, with subsequent repair of the blood-brain barrier in the apparent absence of direct astrocytic contact. *Glia*, 45(4):325–337, 2004.

[207] J. R. Wolff and T. I. Chao. Cytoarchitectonics of non-neuronal cells in the central nervous system. In L. Hertz, editor, *Advances in Molecular and Cell Biology*, volume 31, pages 1–51. Elsevier, 2004.

[208] H. B. Xia, Q. W. Mao, H. L. Paulson, and B. L. Davidson. sirna-mediated gene silencing in vitro and in vivo. *Nature Biotechnology*, 20(10):1006–1010, 2002.

[209] B. Xiao, J. C. Tu, and P. F. Worley. Homer: a link between neural activity and glutamate receptor function. *Current Opinion in Neurobiology*, 10(3):370–374, 2000.

[210] C. Xu and W. W. Webb. Measurement of two-photon excitation cross sections of molecular fluorophores with data from 690 to 1050 nm. *Journal of the Optical Society of America B-Optical Physics*, 13(3):481–91, 1996.

[211] C. Xu, R. M. Williams, W. R. Zipfel, and W. W. Webb. Multiphoton excitation cross sections of molecular fluorophores. *Bioimaging*, 4(3):198–207, 1996.

[212] C. Xu, W. Zipfel, J. B. Shear, R. M. Williams, and W. W. Webb. Multiphoton fluorescence excitation: New spectral windows for biological nonlinear microscopy. *Proceedings of the National Academy of Sciences of the United States of America*, 93(20):10763–10768, 1996.

[213] J. P. Ying, F. Liu, and R. R. Alfano. Spatial distribution of two-photon-excited fluorescence in scattering media (vol 38, pg 224, 1999). *Applied Optics*, 38(10):2151–2151, 1999.

[214] E. J. Yoder. Modifications in astrocyte morphology and calcium signaling induced by a brain capillary endothelial cell line. *Glia*, 38(2):137–145, 2002.

[215] D. H. Yu, G. S. Baird, R. Y. Tsien, and R. L. Davis. Detection of calcium transients in drosophila mushroom body neurons with camgaroo reporters. *Journal of Neuroscience*, 23(1):64–72, 2003.

[216] J. Zhang, R. E. Campbell, A. Y. Ting, and R. Y. Tsien. Creating new fluorescent probes for cell biology. *Nature Reviews Molecular Cell Biology*, 3(12):906–918, 2002.

[217] W. R. Zipfel, R. M. Williams, and W. W. Webb. Nonlinear magic: multiphoton microscopy in the biosciences. *Nature Biotechnology*, 21(11):1368–1376, 2003.

[218] M. Zonta, M. C. Angulo, S. Gobbo, B. Rosengarten, K. A. Hossmann, T. Pozzan, and G. Carmignoto. Neuron-to-astrocyte signaling is central to the dynamic control of brain microcirculation. *Nature Neuroscience*, 6(1):43–50, 2003.

[219] Y. Zuo, J. L. Lubischer, H. Kang, L. Tian, M. Mikesh, A. Marks, V. L. Scofield, S. Maika, C. Newman, P. Krieg, and W. J. Thompson. Fluorescent proteins expressed in mouse transgenic lines mark subsets of glia, neurons, macrophages, and dendritic cells for vital examination. *Journal of Neuroscience*, 24(49):10999–11009, 2004.

I am deeply greatful to

Prof. Bert Sakmann for his exceptionally generous support

Prof. Fritjof Helmchen for mentorship, the experimental freedoms granted, as well as his outstanding personal commitment and support

Dr. Jason Kerr, Dr. Pavel Osten, and PD Dr. Frank Kirchhoff for their great personal and scientific support

Dr. Patrick Theer, Dr. Jack Waters, and Werner Göbel for fruitful discussions

The Böhringer Ingelheim Fonds for funding

Furthermore, I would like to thank

Prof. Winfried Denk for his support at the initial stages of microscope miniaturization

Prof. Karlheinz Meier for supervising this thesis as a member of the Combined Faculties for the Natural Sciences and for Mathematics

Prof. Heinz Horner and Prof. Rainer Fink for joining the dissertation committee

Dr. Tansu Celikel, Dr. Patrick Krieger, Marlies Kaiser, and all other members of the Cell Physiology Department

Dr. Valery Grinevich, Tanjew Dittgen, and Pawel Licznerski

The Mechanical and Electronics Workshop, Tatjana Pospiech, and Klaus Bauer

Special thanks go to

My Parents, my Grandma, my Brother, Diana Dudziak, and my Friends

Appendix A

Supplementary Movies

The thesis includes supporting material, which is essential for its evaluation. In particular, it comprises 19 movie files showing dynamic data discussed quantitatively in the text. All movie files are included on a CD-ROM attached to the thesis. A short description of the dynamic data is given below.

A.1 Neurons

Supplementary Movie SN1. Three-dimensional distribution of FCK(1.3)GW-infected neurons in cortical layer 2/3 of rat neocortex (P28) in vivo. The images are maximum-intensity side projections from a stack of fluorescence images recorded 7 days after virus infection. Individual focal planes were recorded in 2.0 μm steps starting from 860 μm depth below the pial surface. (Scale bar, 40 μm.)
Folder: Neurons *File Name: NimmerjahnMovSN1.avi*

Supplementary Movie SN2. Two-photon time-lapse recording of dendritic spines in layer 1 of the intact mouse neocortex. Infected neurons are located in layer 2/3. Each image is a maximum-intensity projection of a stack of fluorescent images collected every 1.0 μm in axial direction. Image stacks were recorded every 60 s for 45 min. On this time course, no retraction or new formation of dendritic spines were observed. (Scale bar, 2.5 μm.)
Folder: Neurons *File Name: NimmerjahnMovSN2.avi*

Supplementary Movie SN3. Structural dynamics of axonal projections recorded in layer 1 of mouse neocortex by using in vivo two-photon microscopy. Infected neurons are located in layer 2/3. Each image is a maximum-intensity projection of a stack of fluorescent images collected with 1.5 μm axial spacing. Corresponding image stacks were recorded every 5 min for 350 min $\sim$300 μm away from the injection site. Some axonal fiber endings show directed outgrowth for several micrometers on time scale of several hours in a probing manner. (Scale bar, 5 μm.)
Folder: Neurons *File Name: NimmerjahnMovSN3.avi*

A.2 Astrocytes

Supplementary Movie SA1. Three-dimensional distribution of SR101 labeled cells in mouse neocortex in vivo. The images are maximum-intensity side-projections from a stack of fluorescence images recorded approximately 30 min after dye application. Individual focal planes were recorded in 3 μm steps starting from the pia surface down to 705 μm depth.

Folder: Astrocytes *File Name: NimmerjahnMovSA1.avi*

Supplementary Movie SA2. SR101 uptake in EGFP-expressing astrocytes in TgN(GFAP-EGFP) mice. The focus series is an overlay of the simultaneously recorded green and red fluorescence images of EGFP-expressing astrocytes and SR101 labeled cells, respectively. Images are 103 μm on side and were recorded approximately 310 μm below the pia with 1.0 μm axial spacing.

Folder: Astrocytes *File Name: NimmerjahnMovSA2.avi*

Supplementary Movie SA3. SR101 is not taken up by EGFP-expressing microglial cells in CX_3CR1-deficient mice. The focus series is an overlay of the simultaneously recorded green and red fluorescence images showing no overlap of microglial and SR101-labeled cells. Images are 103 μm on side and were recorded approximately 140 μm below the pia with 1.0 μm axial spacing.

Folder: Astrocytes *File Name: NimmerjahnMovSA3.avi*

Supplementary Movie SA4. Focus series demonstrating the close association between SR101 labeled cells (shown in green color) and the cortical microvasculature (shown in red color). Blood plasma was stained using a tail vein injection of FITC-labeled dextran. SR101 labeling was achieved using surface application of the dye. The endothelial sheet surrounding the blood vessels is visible as a dark gap (unstained area) between end feet and labeled vessel lumen. Images are 87 μm on side and were recorded starting from 110 μm below the pia in axial steps of 1.0 μm.

Folder: Astrocytes *File Name: NimmerjahnMovSA4.avi*

A.3 Microglia

Supplementary Movie SM1. Typical motility of resident microglial cells in the intact mouse brain. Each frame is a maximum-intensity projection from stacks of fluorescence images recorded every 45 s (150 - 100 μm below the pia; 2 μm axial spacing). (Image width, 150 μm; rate, 13 fps)

Folder: Microglia *File Name: NimmerjahnMovSM1.avi*

Supplementary Movie SM2. Typical microglial cell motility in the resting state imaged through the thinned skull (individual cell). Each image is an overlay of two maximum-intensity projection images, recorded at $t_0 = 0$ min and $t_i = (t_0+i)$ min. Projection images were created from stacks of fluorescence images acquired during time-lapse recording (1 min sampling interval; 45 - 75 μm below the pia; 1 μm steps). Green and red colors thus indicate new formation and deletion of microglial processes over time, respectively. (Image width, 51 μm; rate, 7 fps)

Folder: Microglia *File Name: NimmerjahnMovSM2.avi*

Supplementary Movie SM3. High-resolution time-lapse series showing that microglial cells continually and repeatedly sample the brain parenchyma with highly motile protrusions. Individual images are maximum-intensity projections through stacks of fluorescence images recorded every 15 s with 2 μm axial spacing through the thinned skull. (Image width, 22 μm; rate, 13 fps)

Folder: Microglia *File Name: NimmerjahnMovSM3.avi*

Supplementary Movie SM4. Time-lapse series showing spontaneous formation of an inclusion and its transport toward the soma in the normal brain. Images are maximum-intensity projections through stacks of fluorescence images recorded every 40 s (2 μm axial spacing; 150 - 110 μm below the pia; every second frame shown). (Image width, 50 μm; rate, 14 fps)

Folder: Microglia *File Name: NimmerjahnMovSM4.avi*

Supplementary Movie SM5. Microglial cell protrusions make close contact to neurons and other cortical elements in vivo. The time series is an overlay of the simultaneously recorded green and red fluorescence images of EGFP-expressing microglia and SR101 labeled astrocytes, respectively. Neurons and blood vessels appear as unstained dark areas. In addition, blood vessels are enwraped by SR101-labeled astrocytic end feet. Images are maximum-intensity projections through stacks of fluorescence images recorded 145 - 125 μm below the pia (2 μm axial spacing; 15 s sampling interval; every second frame shown). (Image width, 54 μm; rate, 13 fps)

Folder: Microglia *File Name: NimmerjahnMovSM5.avi*

Supplementary Movie SM6. Enhanced microglia volume surveillance in response to surface application of BCC (50 μM), an ionotropic GABA receptor blocker used to increase neuronal activity. In the time series, BCC application is indicated by a white square in the upper right corner. Each image is a maximum-intensity projection through stacks of fluorescence images (2 μm axial increment) recorded every 40 s in layer 2/3 of mouse neocortex in vivo (every second frame shown). (Image width, 160 μm; rate, 8 fps)

Folder: Microglia *File Name: NimmerjahnMovSM6.avi*

Supplementary Movie SM7. Microglial cell activation following targeted BBB disruption of a microvessel using a highly localized laser lesion. Simultaneously recorded green (left) and red (right) channel of EGFP-expressing microglia and SR101 labeled

astrocytes, respectively, are shown side by side. BBB disruption is evident in the red channel by local tissue expansion and detachment of astroglial end feet. Immediately after the microlesion (indicated by a white square) nearby microglial cells switch from an undirected surveillance behavior to targeted movement of their processes towards the injured site. Also note the formation and collapse of spherical shaped inclusion in the vicinity of the injured site. The time series was recorded 180 - 135 μm below the pial surface with a 40 s time interval between successive fluorescence image stacks. (One channel image width, 112 μm; rate, 14 fps)

Folder: Microglia *File Name: NimmerjahnMovSM7.avi*

Supplementary Movie SM8. Microglia activation following targeted BBB disruption of a microvessel using a highly localized laser-induced microlesion (indicated by a yellow square). Individual images are overlays of the simultaneously recorded green and red fluorescence channel showing EGFP-expressing microglia and Texas Red-dextran labeled blood plasma, respectively. BBB disruption is evident through release of stained blood plasma into the extracellular space, local tissue expansion and gradual staining of damaged BBB components by the released (red fluorescent) dye. Note, that microglial processes immediately invade the affected areas. Phagocytosis is indicated by increased protrusive activity within these areas and inclusion of damaged tissue components. Also note the shielding of nearby microvessel branches by microglial excrescences. The time series was recorded 140 - 80 μm below the pial surface with a 60 s time interval between successive fluorescence image stacks. (Image width, 87 μm; rate, 10 fps)

Folder: Microglia *File Name: NimmerjahnMovSM8.avi*

Supplementary Movie SM9. Comprehensive microglia activation following a highly localized laser lesion. Immediately after the microlesion (indicated by a white square) nearby microglial cells switch from an undirected surveillance behavior to targeted movement of their processes towards the injured site. The time series was recorded 130 - 90 μm below the pial surface with a 40 s time interval between successive fluorescence image stacks (every second frame shown). (Image width, 111 μm; rate, 8 fps)

Folder: Microglia *File Name: NimmerjahnMovSM9.avi*

Supplementary Movie SM10. Shielding of a microvessel segment by microglial processes following a laser-induced microlesion (indicated by a yellow square). The time series is an overlay of the simultaneously recorded green and red fluorescence images of EGFP-expressing microglia and SR101 labeled astrocytes, respectively. Note that only one microglial cell appears to participate in the response to the highly localized injury. Fluorescence image stacks were taken every 30 s between 150 and 110 μm below the pia (every second frame shown). (Image width, 93 μm; rate, 10 fps)

Folder: Microglia *File Name: NimmerjahnMovSM10.avi*

Supplementary Movie SM11. Time series showing the formation and collapse of spherical shaped inclusions in the vicinity of a laser-lesioned blood vessel arborization, indicating phagocytosis. Each image is a subvolume projection (2 focal planes; 2 μm apart)

of the recorded fluorescence image stacks at the level of microvessel cross section (30 s sampling interval; every fourth frame shown). (Image width, 50 μm; rate, 9 fps)

Folder: Microglia *File Name: NimmerjahnMovSM11.avi*

Supplementary Movie SM12. Microglia response to local LPS application. Individual images are overlays of the simultaneously recorded green and red fluorescence channel showing EGFP-expressing microglia and the LPS containing micropipette, respectively. For visualization, 100 μM Alexa Fluor 594 was added to the pipette solution. Two pressure applications are visible through a transient increase in red background fluorescence. In response to LPS application, microglia showed targeted outgrowth of their processes towards the source of inflammation. Note, that the micropipette becomes overgrown by microglia extensions, and that a dense meshwork of processes forms around its tip. Each image is a projection (45 focal planes; 2 μm apart) of the recorded fluorescence image stacks 140 - 50 μm below the pial surface (120 s sampling interval; micropipette tip located at 95 μm below the pial surface). (Image width, 188 μm; rate, 9 fps)

Folder: Microglia *File Name: NimmerjahnMovSM12.avi*

Appendix B

Acronyms

This chapter reviews acronyms used in this thesis:

AP	Action Potential
APD	Avalanche Photo Diode
BCC	Bicuculline
CaM	Calmodulin
EGFP	Enhanced Green Fluorescent Protein
FP	Fluorescent Protein
GFP	Green Fluorescent Protein
GM	Göppert-Mayer
GVD	Group Velocity Dispersion
LTP	Long-Term Potentiation
NA	Numerical Aperture
PMT	Photomultiplier Tube
PSF	Point Spread Function
S/N	Signal-to-Noise
SPM	Self-Phase Modulation
SR101	Sulforhodamine 101
TPTP	Two-Photon Targeted Patching
TTX	Tetrodotoxin
2PM	Two-Photon Microscopy *(more precisely, Two-Photon Laser-Scanning Fluorescence Microscopy)*